NTNU – Trondheim
Norwegian University of
Science and Technology

Thermal characterisation of anode materials for Li-ion batteries

Øystein Gullbrekken

Materials Technology
Submission date: July 2012
Supervisor: Fride Vullum, IMTE
Co-supervisor: Ann Mari Svensson, SINTEF
Edel Sheridan, SINTEF
Anita Fossdal, SINTEF

Norwegian University of Science and Technology
Department of Materials Science and Engineering

Declaration

I declare that the work described in this Master's thesis has been performed independently and in accordance with the rules and regulations for examinations at the Norwegian University of Science and Technology, NTNU.

Øystein Gullbrekken

Trondheim, July 9, 2012

Preface

The present work was conducted as part of a larger battery project collaboration entitled "Carbon materials for improved stability of anodes for Li-ion batteries" (CARBATT). Several partners are involved in this project, and particularly the Department of Materials Science and Engineering at NTNU and SINTEF Materials and Chemistry are responsible for the research activities. The main objectives of CARBATT are to increase the understanding of how correlations between surface structure, surface chemistry and morphology of carbon materials influence the performance of anodes for Li-ion batteries. The new understanding will then be utilised to improve the electrochemical and thermal stability of Li-ion batteries, exemplified by demonstration of a small-scale battery. CARBATT started in 2009 and will be running through 2012[1]. The current work is also an extension of a project work carried out in the autumn semester of 2011 by the author which resulted in a report titled "Thermal characterisation of graphite materials for Li-ion batteries".

Most of the experiments and analyses described in this thesis were conducted at the Department of Materials Science and Engineering at NTNU by the author. One of the electrode materials studied, Timcal SLP30, and one electrolyte were prepared by Research Scientist Edel Sheridan from SINTEF. The other four electrolytes investigated were prepared by PhD candidate Carl Erik Lie Foss.

First of all, I would like to thank my main supervisor Associate Professor Fride Vullum-Bruer at NTNU for rewarding discussions about the findings of this work. In addition, I want to thank Research Scientists and co-supervisors Anita Fossdal and Edel Sheridan from SINTEF for helping out with the thermal analysis, Senior Research Scientist and co-supervisor Ann Mari Svensson from SINTEF for helpful input concerning the interpretation of results, and PhD candidate Morten Onsrud for lab assistance and informative discussions. Finally, I want to thank PhD candidate and co-supervisor Carl Erik Lie Foss for being generally very helpful and always ready for a discussion.

[1] From the project description of CARBATT

Abstract

Coin cells with lithium and graphite electrodes were assembled using different combinations of graphite material and electrolyte. Specifically, three commercially available graphite materials and five electrolyte compositions were studied. The cells were discharge-charge cycled with varying parameters in order to determine the performance of the graphite materials and electrolytes. Particularly, a temperature chamber was employed to cycle some cells at temperatures between 0 and 40°C to find the significance of the electrolyte composition and graphite material on the cell performance at these temperatures. The cycled cells were disassembled and samples from the graphite electrode soaked with electrolyte were prepared for thermal analysis, specifically differential scanning calorimetry (DSC). The thermal stability of the graphite electrodes and the influence from the graphite and electrolyte properties and the cycling parameters were analysed. In order to facilitate the interpretation of the results from discharge-charge cycling at different temperatures, DSC analysis from -80 to +50°C was performed on the pure electrolytes.

Confirming previous studies, it was found that both the thermal stability and cycling performance were highly influenced by the properties of a solid electrolyte interphase (SEI), situated between the graphite surface and the electrolyte and formed during cycling. The three graphites were good substrates for stable SEI formation, exhibited by high thermal stability after being cycled at room temperature. After cycling with a temperature program, subjecting the cells to temperatures between 0 and 40°C, the thermal stability was generally reduced. This was attributed to increased SEI formation. The properties of both the electrolyte and graphite influenced the SEI and consequent thermal stability, though in different ways.

The cell capacity was considerably reduced upon cycling at lower temperatures, such as 10 and 0°C. The results indicate that the electrolyte properties, particularly the viscosity and resulting conductivity, played the most important role in determining the cell performance. Low viscosity electrolyte components should be utilised, maintaining the electrolyte conductivity even at reduced temperatures. The graphite properties did not influence the cell performance at the temperatures studied. Advice is given on which electrolyte components should be avoided to build Li-ion cells performing acceptably at temperatures from 0 to 40°C.

Sammendrag

Knappeceller med litium- og grafitt-elektroder ble satt sammen ved å bruke forskjellige kombinasjoner av grafittmaterial og elektrolytt. Tre kommersielle grafittmaterialer og fem elektrolytt-sammensetninger ble studert. Cellene ble utladet og oppladet gjentatte ganger (sykling) med forskjellige parametre for å bestemme ytelsen av grafittmaterialene og elektrolyttene. Et temperatur-kammer brukt til å sykle noen av cellene ved temperaturer mellom 0 og 40°C for å finne ut hvordan elektrolytt-sammensetningen og grafittmaterialet påvirket celleytelsen ved disse temperaturene. De ferdig-syklede cellene ble demontert og prøver fra grafitt-elektroden fuktet med elektrolytt ble preparert for termisk analyse, spesifikt differensiell scanningskalorimetri (DSC). Grafitt-elektrodenes termiske stabilitet og påvirkningen fra grafittens og elektrolyttens egenskaper og parametere brukt ved sykling ble analysert. I tillegg ble DSC-analyser fra -80 til +50°C utført på de rene elektrolyttene for å støtte tolkningen av resultatene fra syklingen av celler ved forskjellige temperaturer.

Det ble funnet at egenskapene til en fast elektrolytt-fasegrenseflate (SEI), lokalisert mellom grafittoverflaten og elektrolytten og dannet i løpet av sykling, hadde stor påvirkning på både den termiske stabiliteten og ytelsen ved sykling, hvilket bekreftet tidligere studier. De tre grafittene var gode substrater for stabil SEI-dannelse, som viste seg i form av høy termisk stabilitet etter at de var syklet i romtemperatur. Den termiske stabiliteten ble redusert etter sykling med temperatur-program, som utsatte cellene for temperaturer mellom 0 og 40°C. Årsaken for dette ble tilskrevet økt SEI-dannelse. Egenskapene til både elektrolytten og grafitten påvirket SEI-laget og den termiske stabiliteten, dog på forskjellige måter.

Cellekapasiteten ble betydelig redusert ved sykling ved lavere temperaturer som 10 og 0°C. Resultatene indikerer at elektrolytt-egenskapene, spesielt viskositeten og den resulterende ledningsevnen, påvirket celleytelsen mest. Elektrolytt-komponenter med lav viskositet burde benyttes for å opprettholde elektrolyttens ledningsevne selv ved reduserte temperaturer. Grafitt-egenskapene påvirket ikke celleytelsen ved temperaturene brukt i denne studien. Oppgaven presenterer råd om hvilke elektrolytt-komponenter som burde unngås for å bygge Li-ion celler med akseptabel ytelse ved temperaturer mellom 0 og 40°C.

List of abbreviations

DSC	Differential scanning calorimetry
SEI	Solid electrolyte interphase
ICL	Irreversible capacity loss
EC	Ethylene carbonate
PC	Propylene carbonate
DEC	Diethyl carbonate
DMC	Dimethyl carbonate
EMC	Ethylmethyl carbonate
VC	Vinylene carbonate
MCMB	Mesocarbon microbeads
FTIR	Fourier transform infrared spectroscopy
XPS	X-ray photoelectron spectroscopy
BET	Brunauer-Emmett-Teller (specific surface area measurement method)
ASA	Active surface area
PVDF	Poly(vinylidene fluoride)
GIC	Graphite intercalation compound
SEM	Scanning electron microscopy
NMP	1-methyl-2-pyrrolidinone
EA	Ethyl acetate
RT	Room temperature
DFT	Density functional theory
XRD	X-ray diffraction
EIS	Electrochemical impedance spectroscopy

Contents

1 Introduction

Li-ion batteries are currently the state of the art rechargeable battery system. They provide the highest gravimetric and volumetric energy densities, display superior cycleability during long time operation compared to other systems, and have proven highly flexible with respect to design, size, and thus application. Because of this, Li-ion batteries are the system of choice to provide power in almost all current portable electronic equipment [1].

Moreover, the battery system is recently facing new applications and its use is expected to increase globally. Because of its favourable properties mentioned above, Li-ion batteries are the most promising for use in both electric and hybrid electric vehicles [2], the markets of which are expected to grow substantially in the coming years [3]. As sustainability and environmentally damaging emissions from the present use of fossil fuels receive more attention, large research efforts are made to design and optimise devices for utilising alternative energy sources, such as solar and wind power. The industries related to exploiting solar energy are currently experiencing the greatest expansion of all energy industries, with up to 40% increase of global installed capacity per year [4]. However, due to natural variations they both deliver variable power output over time and as a result, a system for storing energy produced during periods of excess production will be required for times of energy deficit. The Li-ion battery is a very relevant candidate for small to medium sized and even large size energy storage systems [5].

Along with the expansion of these new applications, higher and novel requirements must be met by the batteries, which is the driving force behind much of the present research activity in the field. In an electric car, for example, the batteries should allow for high power rate output to accelerate the car, show minimal capacity loss after long time operation [6] and display excellent stability over a range of different environmental conditions, particularly both at low and high temperatures [7]. The latter points are a key challenge in order to establish electric cars as a viable alternative to conventional cars running on fossil fuels. Battery components, and in particular the electrolyte composition, are being redesigned and optimised with respect to the new requirements [8].

In spite of the beneficial qualities of Li-ion batteries and its future use looking secured, there are several vulnerabilities in current Li-ion batteries. Perhaps the most severe weakness is related to the thermal instability and safety of the batteries.

Such examples have been conveyed through media many times, especially in the early 2000's, in incidents ranging from cellular phones smoking to laptops catching fire or even exploding [9]. As late as in 2006, Sony Corporation recalled approximately 10 million Li-ion batteries because they could potentially overheat and catch fire [10]. In small Li-ion batteries for use in laptops and cellular phones, this safety problem is limited. In larger batteries, for example in electric vehicles or ferries, however, the consequences of such a battery failure could be devastating. Research is conducted globally to optimise the batteries and minimise the safety issues [9].

One of the most important features of Li-ion batteries, particularly so for the thermal stability, is the solid electrolyte interphase (SEI) [11]. It consists of decomposed electrolyte species and covers both electrodes in the battery, acting as a barrier between the electrolyte and electrodes. The thin layer has been subject to great interest for several decades as it determines many performance parameters of the battery. Nonetheless, since it is formed after the battery has been assembled and is difficult to analyse in situ, there is still uncertainty regarding its composition, structure and general properties. Exothermic reactions occurring in the SEI layer on elevated temperatures are believed to facilitate overheating that could result in the battery phenomenon "thermal runaway", causing the battery to smoke, catch fire, or explode [12].

Aim of this work

This work aims at investigating and comparing the thermal stability of some selected commercially available graphite materials for different applications, intended for use as intercalation anodes in Li-ion batteries. Additionally, the temperature-dependency of the performance of several graphite materials and electrolytes will be examined. The graphite materials will be electrochemically cycled with varying parameters, e.g. temperature, while subjected to different electrolytes, both conventional and optimised for low temperature. Thermal characterisation using specific analysis methods will then be conducted in order to find the significance of the various parameters on the thermal stability. Attempts will be made to unravel the processes and mechanisms causing the observed behaviour, both related to cycling and thermal stability, including reasons for any differing performance of the materials.

2 Theory

2.1 Electrochemical principles

Principally, the functionality of Li-ion batteries is no different to any other rechargeable battery system. Upon discharge, the battery delivers electric energy. This energy is originally stored as chemical energy in the active materials of the battery and is converted through an electrochemical reduction-oxidation (redox) reaction. The reaction is enabled by electrons spontaneously flowing from the negative to the positive electrode via an external circuit. Upon charging, the reverse reaction takes place as the electrons travel the opposite direction due to externally applied electric energy. Electric energy is then supplied and converted to chemical energy that is stored in the active materials of the battery. All these processes occur in the basic electrochemical unit of the battery, the cell [13]. A schematic illustration of the operation of a Li-ion cell is provided in Figure 1. Batteries are comprised of one or several cells connected in series and in parallel in order to obtain the desired voltage and capacity, respectively.

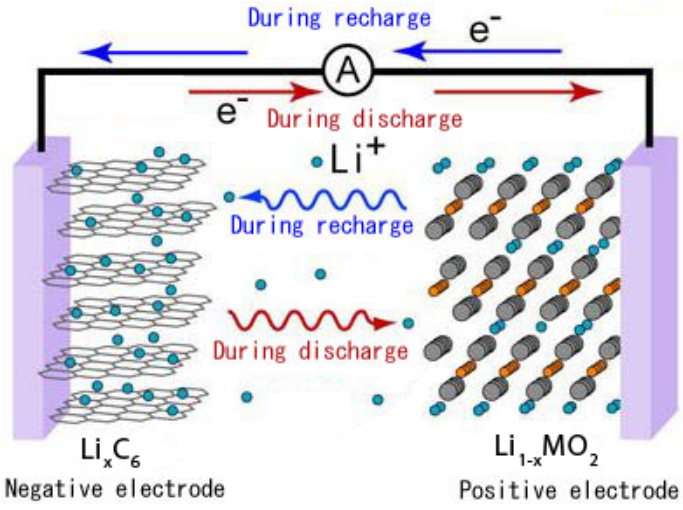

Figure 1: Operating principle of Li-ion cell. Modified from [14].

The electrochemical cell consists of two electrodes, the anode and cathode, wherein the chemical energy is stored, and the electrolyte, separating the electrodes. By definition, the cathode is the location of the reduction reaction and the anode is the location of the oxidation reaction. The oxidation reaction releases electrons that are subsequently consumed by the reduction reaction. Consequently, the external electron flow is always from the anode to the cathode during operation. Accordingly, the electrodes act as anode or cathode depending on whether the cell is being

charged or discharged. Upon discharge, the electron flow is from the negative electrode acting as anode to the positive electrode acting as cathode. Concurrently, the negative and positive ions, anions and cations, which are dissolved in the electrolyte, migrate to the oppositely charged electrodes to maintain the charge balance of the cell. Upon charging of the cell, the negative electrode functions as cathode while the positive electrode functions as anode due to an externally applied voltage exceeding the internal electrochemical potential difference. As a result, the direction of the electron flow and the migration directions of the anions and cations are reversed. The functionality of an electrode during discharge defines whether it is classified as an anode or a cathode.

The electrolyte enables the internal charge transfer of the cell by means of ion conduction, while acting as an electronic barrier separating the electrodes [15]. A porous separator, often made of a polymeric material and capable of conducting ions, prevents the electrodes from physically coming into contact and thus the electronic short-circuiting of the cell [13].

2.2 The electrode reactions and intercalation process

Upon discharging and charging (electrochemical cycling) of a Li-ion cell, Li^+ ions shuttle back and forth between the positive and negative electrodes. The processes of Li^+ ions entering and leaving the electrodes are called intercalation and de-intercalation, respectively. These involve the reversible insertion and removal of the ions from the host. Often, the host material experiences a volume change during these processes. The structure of the material, however, is not significantly altered. The actual mechanism of intercalation depends on the crystal structure of the host material and the properties of the ions. Figure 2 is a schematic illustration of the mechanism of intercalation of Li^+ ions into a common anode material, graphite. In order to enter the graphite, the Li^+ ions must approach the structure from the edge plane, i.e. between the graphene planes.

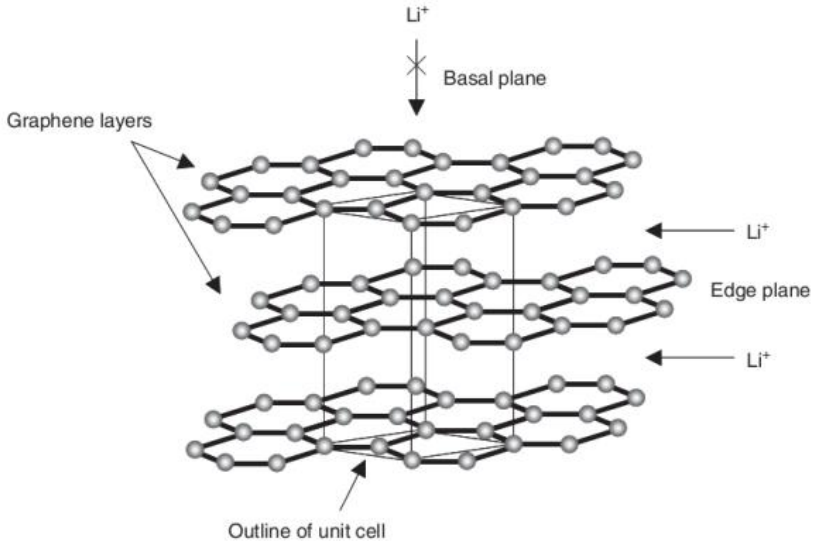

Figure 2: Insertion mechanism of Li^+ into graphite. The ions must enter via the edge plane and are then bonded between the graphene layers by means of van-der-Waals interactions. Modified from [16].

The cell is charged as Li^+ ions enter the graphite and diffuses into the structure. The intercalation occurs sequentially and several phases, termed stages, with gradually higher amounts of Li^+ are obtained before the graphite is fully charged. In voltage-charge curves, the stages appear as distinct voltage plateaus as exemplified in Figure 3, where the three main stages can be seen [13]. Typically, the intercalation stages of Li^+ occur between 0.2 and 0.05 V vs. Li/Li^+ on discharging, and at slightly higher voltages on charging. The main reason for the sequential intercalation is thermodynamic effects due to expansion of graphene planes [17]. The expansion energy increases with the number of neighbouring graphene layers on both sides of the relevant gap for intercalation. Consequently, intercalation usually begins near the basal planes (in the gap adjacent to the end basal plane) of the graphite particles where the expansion energy is lowest. As the graphite electrode is charged, the intercalation progresses toward internal layer gaps.

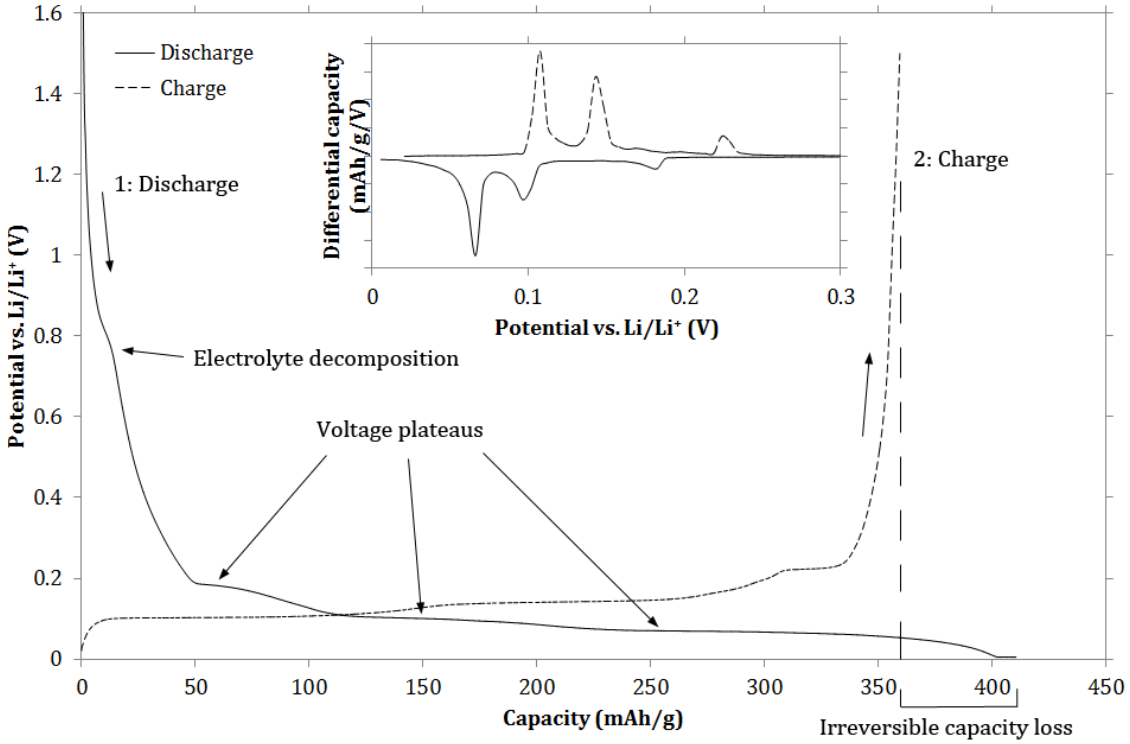

Figure 3: Voltage-charge curve of the initial discharge-charge cycle of a Li/graphite half cell. Lithium metal will deposit at 0 V. The different stages in the initial cycle are specified, along with the irreversible capacity loss (ICL). The insert shows the differential capacity vs. voltage, displaying the three main intercalation stages upon discharging and charging. Note that the plateaus appear at higher voltages on charging than discharging.

The theoretical maximum capacity of Li^+ ions in the graphite structure corresponds to LiC_6, i.e. one Li^+ per six carbon atoms. The in-plane structure of fully intercalated graphite is displayed in Figure 4. In terms of electric energy, the theoretical capacity of graphite in Li-ion cells is 372 mAh/g [13]. The calculation of the specific capacity of graphite is provided in appendix A.1.

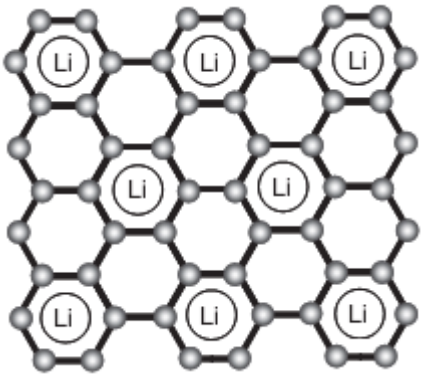

Figure 4: In-plane structure of graphite fully intercalated with Li^+ ions, corresponding to LiC_6. Modified from [16].

The electrode reactions and total cell reaction for a standard $LiMO_2$/graphite cell are as follows [13]:

Positive electrode:	$LiMO_2 \rightleftharpoons Li_{1-x}MO_2 + xLi^+ + xe^-$	(2.1)
Negative electrode:	$6C + xLi^+ + xe^- \rightleftharpoons Li_xC_6$	(2.2)
Cell reaction:	$LiMO_2 + 6C \rightleftharpoons Li_xC_6 + Li_{1-x}MO_2$	(2.3)

Depending on the level of intercalation of Li^+ ions in the graphite structure, x goes from 0 to 1 in the negative electrode reaction. The maximum level of reversible de-intercalation of lithium in common cathode materials, e.g. lithium metal oxides, however, is limited by structural restrictions and corresponds to less than $x = 1$ [18]. For the reactions in equations (2.1)-(2.3) the arrows to the right represent charging, while those to the left represent discharging of the cell.

2.3 Common materials in Li-ion batteries

Even if the shapes, sizes and applications of Li-ion batteries vary considerably, the internal design and materials used in commercially available batteries are quite similar. In all Li-ion batteries, both electrodes are made up of lithium insertion materials, i.e. materials capable of repeatedly hosting and evacuating Li^+ ions [13]. As these materials undergo large compositional changes, it is a requirement that their crystal structure remains stable over a wide range of compositions. An overview of relevant anode and cathode materials presently used or considered for next-generation Li-ion batteries is provided in Figure 5. Their capacities and potentials against Li metal are also represented.

The cathode is the lithium source in the battery, and is commonly based on a lithium transition metal oxide; $LiMO_2$. Traditionally, $LiCoO_2$ has been the most utilised active cathode material. Recently, due to the new and tougher requirements and a wish to reduce cost and improve stability, the look for alternative cathode materials has intensified. Current high-performance cathode materials have lower capacity than the anode materials, and are thus capacity-limiting in the battery. Promising candidates for next-generation cathode materials are $Li(Ni,Mn,Co)O_2$ materials of different stoichiometric compositions, spinel type materials such as $LiMn_2O_4$, and transition metal phosphates ($LiMPO_4$) with olivine crystal structure. However, the development of cathode materials is a challenge. The stabilisation of the crystal structure during de-lithiation and improvement of the microstructure and morphology in order to increase conductivity and optimise the electrode-electrolyte

interface are main tasks in order to engineer better cathodes [19]. Regardless, cathode materials have not been the focus of this work. In the following, introductions will be given to already commonly featured and promising next-generation electrolytes and active anode materials for Li-ion batteries.

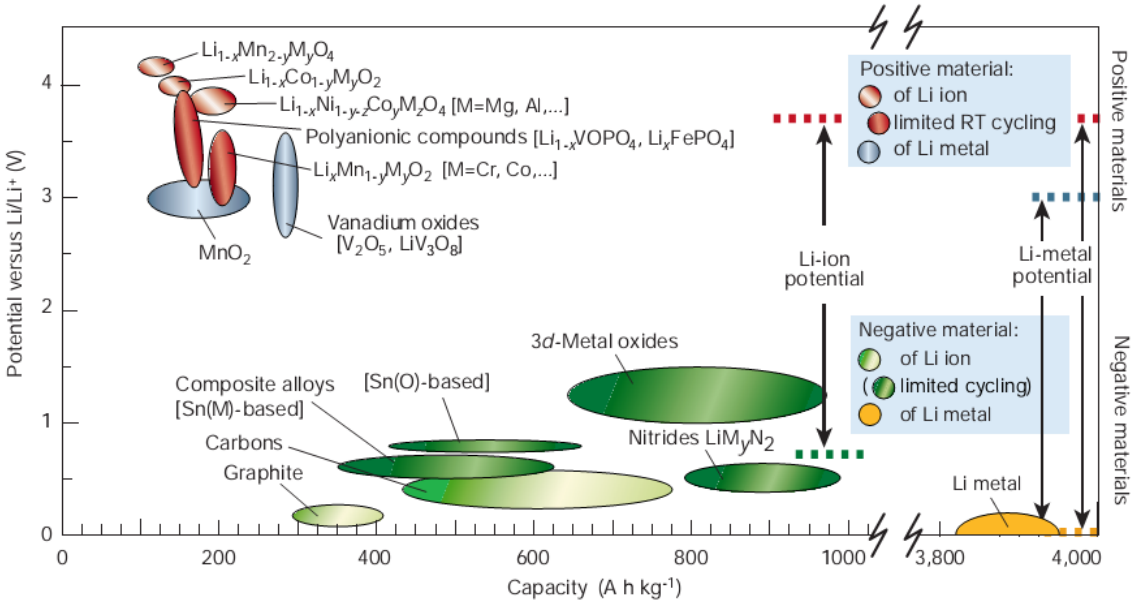

Figure 5: Voltage vs. capacity for most of the currently used or researched anode and cathode materials for Li-ion batteries [1].

2.3.1 Electrolyte

2.3.1.1 Electrolyte principles

Numerous electrolyte compositions have been developed for Li-ion batteries. The compositions are made up of solvents, salts and sometimes additives and all these are usually tailored to meet specific demands. Yet, there is a set of requirements that should be met by any electrolyte composition. Over all, the main function of the electrolyte is to prevent direct electron exchange between the electrodes and thus facilitate the orderly and steady flow of electrons via an external circuit. Simultaneously, the electrolyte must be an ionic conductor (ideally highly conductive) to maintain the internal charge transfer. In addition to these essential requirements, the electrolyte should also satisfy several more to ensure that the resulting battery functions as desired. Perhaps most important, the electrolyte should exhibit a wide electrochemical stability window, preferably over the entire voltage range of the battery. This means that the electrolyte should remain inert during operation. In practice, this can be achieved either by the electrolyte components being thermodynamically stable under the operating conditions, or by effective passivation of the electrode surfaces, preventing sustained decomposition

of electrolyte components. For most Li-ion battery electrolytes, the requirement is obtained by the latter. Other important requirements include wide liquid range, meaning low melting point and high boiling temperature, high safety and low toxicity [15].

Most electrolyte compositions are based on a single lithium salt dissolved in a mixture of two or three solvents. Maintaining ion conductivity is the key reason for mixing several solvents. The ionic conductivity of an electrolyte can be expressed as

$$\sigma = \sum_i n_i \mu_i Z_i e \tag{2.4}$$

where n_i is the number of moles of ion i, μ_i is its mobility, Z_i is the valence number, and e is the electronic charge. For an electrolyte to display high values for all these parameters, it must have contradicting properties. The ability of a solvent to dissolve and coordinate salt ions can be measured by the dielectric constant. In order to coordinate large numbers of ions, the solvent must have high dielectric constant, which is usually associated with high viscosity. Additionally, the dissociation energy of the salt should be low, a result of uniform charge distribution. In contrast, the mobility of ions is improved in a low viscosity solvent where the solvated ions occupy a small volume. These apparently contradicting requirements can be met by mixing one co-solvent displaying high dielectric constant with a low viscosity co-solvent. The former co-solvent would be responsible for dissolving the salt and coordinating Li^+, and the latter for providing a conducting medium of low resistance for the solvated Li^+ ions [15]. Figure 6 shows how Li^+ can be coordinated in an electrolyte solution.

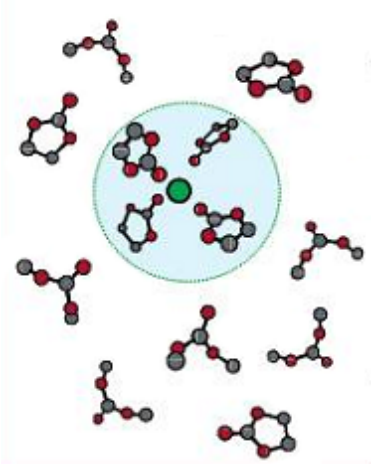

Figure 6: Illustration of Li^+ (green particle) coordinated by four ethylene carbonate molecules in an electrolyte composed of ethylene carbonate and dimethyl carbonate. Modified from [20].

The most important electrolyte requirements are summed up beneath:

- High ionic conductivity
- Electrochemically stable in the operating voltage range of the battery
- High wettability
- Low viscosity (related to high ionic conductivity)
- Ability to dissolve the salt even at high concentrations (high dielectric constant)
- Stable over a wide temperature range
- Low toxicity
- Low cost

In addition the electrolyte should be inert during operation, meaning it would have to be either

- Thermodynamically stable

or

- Reduce to form a protective passivating film on the surface of the electrode, involving an irreversible capacity loss (which is the case for most Li-ion battery systems)

2.3.1.2 Solvents

Because of their oxidative stability and ability to form stable passivating products upon reduction, almost all co-solvents in current Li-ion batteries are esters. Especially the diesters of carbonic acid (carbonates) have found widespread use. Linear and cyclic carbonates possess low viscosity and high dielectric constant, respectively, and many electrolyte formulations are consequently based on a binary

mixture of these. Common cyclic carbonates include ethylene carbonate (EC) and propylene carbonate (PC); particularly the former is a key co-solvent present in almost all electrolytes. Although having a very similar molecular structure to EC, PC is notorious for failing to form a protective film on graphite, and breaking up the graphite structure in a process termed exfoliation. The process of exfoliation is shown in Figure 7. Diethyl carbonate (DEC), dimethyl carbonate (DMC) and ethylmethyl carbonate (EMC) are examples of common linear carbonates [15]. Structural formulas of these important co-solvents are provided in Figure 8. Recently, electrolyte compositions containing three or more solvents have been increasingly studied due to their preferable properties, amongst them inherently higher conductivity [21]. Such electrolytes, particularly utilised for improving low temperature performance, will be further discussed in chapter 2.6.2.

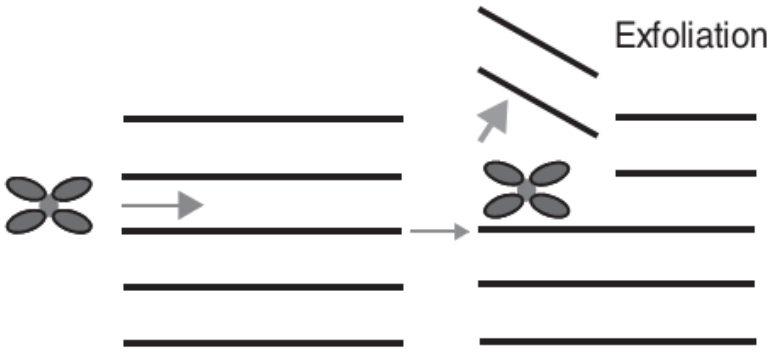

Figure 7: Schematic illustration of a Li^+ ion solvated by four PC molecules that are co-intercalated between graphene planes together with the Li^+ and subsequently exfoliate the structure. Modified from [16].

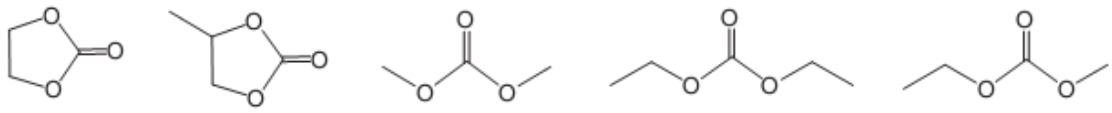

Figure 8: Structural formulas of important co-solvents. From left to right: EC, PC (cyclic carbonates), DMC, DEC, EMC (linear carbonates). Modified from [15].

2.3.1.3 Solutes

Even though several lithium salts have been extensively investigated as electrolyte solutes, lithium hexafluorophosphate ($LiPF_6$) is almost universally used in Li-ion cells. It fulfils both of the important solute requirements; being readily soluble in a non-aqueous solvent and having an anion stable against oxidation. In fact, $LiPF_6$ tends to decompose to form a passive film on positive electrode surfaces.

Nonetheless, as $LiPF_6$ is moisture sensitive and reactive at elevated temperatures, alternative lithium salts are sought for [15]. Lithium bis(oxalato)borate (LiBOB) and lithium difluoro(oxalato)borate (LiDFOB), both containing boron anions, have recently been investigated to improve the high temperature performance of Li-ion batteries [22]. These salts have shown significant improvements on selected properties, however, their overall performance cannot yet compare to $LiPF_6$ [15].

2.3.1.4 Additives

The amount of an electrolyte additive is usually less than 5% by weight or volume. Nevertheless, its presence may significantly improve the performance of Li-ion batteries. Largely speaking, the main objectives of additives include improving the stability of the passivating film (also termed solid electrolyte interphase or SEI [11]) on the electrode surfaces; protecting the cathode material from overcharge and dissolution; stabilising the $LiPF_6$ salt; and enhancing the safety by protecting against overcharge and lowering the flammability of the solvents.

Additives for improving the passivation films are classified according to how they function and most of these are reduction-type, also called sacrificial additives. This means that they have higher reductive potential than the other electrolyte solvents and consequently cover and deactivate the catalytic sites on the electrode surfaces before the other solvents decompose. In this manner, the passivating films can be engineered to a certain degree by determining which decomposition products make up its composition. It has been found that the use of such reductive-type additives, for example vinylene carbonate (VC), has improved the film stability and reduced gas evolution during the initial cycle [22]. Additives and co-solvents designed to improve the low temperature performance will be discussed in chapter 2.6.2.

2.3.2 Active anode materials

2.3.2.1 Lithium metal

The main reason for the Li-ion rechargeable battery system being the widest applied today is the advantageous properties of lithium as an anode material, which led to the initial research. It is the ultimate anode material, owing to three features; the largest theoretical specific capacity of any metal (see Figure 5), the most electropositive metal vs. standard hydrogen electrode, and the lightest metal. These features generate the highest possible gravimetric density and highest cell voltage against any cathode material observed for any element. However, the uneven re-deposition of lithium metal due to non-uniform current distribution, forming

dendrites, resulted in hazard related to short-circuiting which has been a major obstacle for the development of this cell chemistry [15].

2.3.2.2 Carbonaceous materials

In addition to graphite, also other carbonaceous materials have been researched as potential anode materials. These carbonaceous materials, which include synthesised graphite but not naturally occurring graphite, are prepared from two types of starting materials. These are more or less amorphous, and can be distinguished by whether they are graphitisable (soft carbons) or non-graphitisable (hard carbons). As seen in Figure 9, the crystallites are relatively oriented in soft carbons and generally they are stacked in the same direction, whereas they are randomly oriented in hard carbons. Heat treatment thus leads to graphitisation of soft carbons, but not of hard carbons. Notably, both types of materials must first be heat treated in order to be functional host materials for lithium ions.

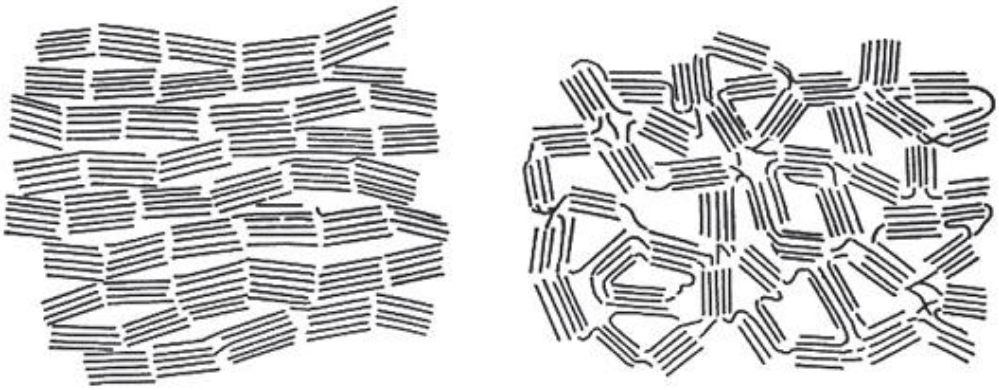

Figure 9: Schematic models of the structures of soft carbon, to the left, and hard carbon, to the right, taken from [16].

The heat treatment temperature determines the resulting structure and capacity of the carbonaceous materials. Soft carbons heat treated above 2400°C become highly graphitised and are converted to graphite, while heat treatment at lower temperatures yield other structures with other properties which are also called soft carbons. As the degree of crystallinity and the crystal structure itself are different for the various resulting materials, the mechanisms of lithium insertion vary accordingly. The carbons heat treated at temperatures below 2400°C usually have larger initial capacity than graphite, as lithium is accommodated by other means than intercalation. Figure 10 shows the specific capacity of soft and hard carbons as a function of their heat treatment temperatures. The exact mechanisms of Li^+ accommodation are still debated. It has been suggested that lithium insertion into

soft carbons heat treated at temperatures below 1000°C, exhibiting the highest capacities, occur by lithium doping in nano-sized cavities, formation of ionic complexes, and chemical reactions between hydrogen-bonded defects in the carbon structure and lithium ions. In hard carbons, adhesion of lithium ions on both sides of single graphene sheets has been proposed as the main mechanism of lithium insertion [16].

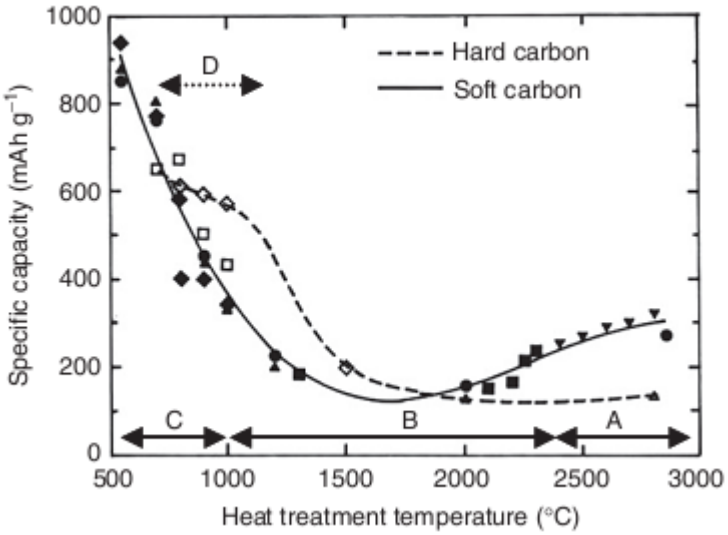

Figure 10: Specific capacity of the different types of soft and hard carbons as a function of their heat treatment temperatures. Region A corresponds to graphite, region B and C to soft carbons heat treated at lower temperatures (called soft carbons) having different structures, and region D is a particular high-capacity type of hard carbon. Closed and open symbols show data for soft and hard carbons, respectively [16].

However, even if both of these carbonaceous materials were used in early commercial Li-ion batteries [23], they have short-comings compared to graphite. Soft carbons have low density, large irreversible capacity in the first cycle and poor cycleability and are mostly discarded as anode materials in the last decade. Hard carbons, suffering from several of the same disadvantages are still promising candidates as negative electrode materials in high capacity batteries. Nonetheless, their low and large potential plateau, increasing the risk of lithium metal deposition, is a problem that must be overcome [16].

2.3.2.3 Graphite

As graphite comprised of micro-scale particles is the most utilised active anode material in current Li-ion batteries, and the anode materials studied in this work are

exclusively graphites, the main focus will be on this anode material. The mechanism of lithium insertion into the graphite structure has already been explained.

Commercial graphite types for Li-ion batteries are natural graphite, highly oriented pyrolytic graphite and modified graphite materials. Natural graphites have not been widely adopted because of the inherent defects found in these, e.g. pores and inhomogeneous surface structure, increasing the irreversible capacity loss. Highly oriented pyrolytic graphites are, due to their structurally high degree of order, mostly used for research purposes. Consequently, most of the graphites used commercially today are of the last type; synthetically modified graphite materials [24].

Much of the development of graphites has revolved around manipulating particle morphology. Common morphologies include fibres, flakes, potatoes and what is termed mesocarbon microbeads (MCMB), which was the leading morphology for a long time. In general, the size of the crystallites is around 50 nm; while the particle size usually varies from a few μm up to 25 μm for different graphites. MCMB is prepared by graphitisation of a specific soft carbon type. It is comprised of spherical particles, leading to minimum surface area. The particularly low irreversible capacity loss observed when using MCMB graphites is one of its most advantageous features [24]. Particles appearing as flakes are also quite commonly used, especially in natural graphites. Flaky particles might be more densely packed than spherical particles, and could thus theoretically contain larger amounts of lithium ions per volume. However, the surface of such particles is usually not as uniform as for spherical particles. It may contain cracks and crevices which are unfavourable, especially regarding the properties of the SEI layer formed on the graphite surface, which will be further discussed in chapter 2.4.2. Graphite flakes are furthermore difficult to distribute thinly and evenly onto the current collector substrate. Also, the flat area of the particles directed towards the Li^+ ion flow tends to be dominated by basal planes, complicating facile Li^+ intercalation [25]. Recently, exemplified by the graphite materials studied in this work, potato-shaped particles have become the morphology of choice in most cases. This morphology can be obtained by coating flaky particles. Potato-shaped particles combine the favourable properties of both spherical and flaky particles. They have uniform and smooth surface as MCMB, but can still be densely packed similarly to flaky particles.

With the recent market increase of electric- and hybrid electric vehicles, graphite materials especially designed for these applications are being engineered.

Particularly hybrid electric vehicles, containing a relatively small Li-ion battery that must be able to provide large amounts of power in short time periods, require high rate capability electrode materials. Consequently, the kinetics of the electrochemical reaction becomes important. Regarding the anode reaction, the process of Li^+ intercalation and diffusion into the graphite structure is usually rate-determining when high rates are employed. A straightforward method for improving the kinetics related to these processes is to decrease the particle size in order to reduce the diffusion distance of Li^+ ions inside the material. Accordingly, graphite materials for power cells usually consist of smaller particles than all-round high performance graphites [26].

Unfortunately, the literature on the field of graphite engineering is quite limited. Several industrial companies, such as Timcal and Phillips 66's CPreme, deliver Li-ion battery grade graphites and much of the science and practical knowledge behind the development and manufacturing of their products are industry secrets and protected by patents.

2.3.2.4 Nanostructured materials

Due to the unusual material properties occurring when the material dimensions are confined to the nanometre scale, nanostructured materials have recently gained large interest worldwide. Also in the field of energy storage, and active storage materials for Li-ion batteries, such materials have been increasingly studied. Electrodes made of nanomaterials have several advantages compared to conventional electrode materials. For example, higher charge and discharge rates can be achieved as the electrolyte/electrode contact area is increased; shorter path lengths also facilitate faster kinetics; and cycle life can be improved by engineering structures optimised for Li^+ accommodation. On the other hand, the higher surface area of nanomaterials could lead to more undesirable reactions at the electrode/electrolyte interface, increasing the SEI formation and thus irreversible capacity loss, and ultimately reducing the cycle life. The poor packing density of nanomaterial electrodes, limiting the volumetric energy density, is another challenge regarding their development. Nanocomposite approaches have been attempted to utilise the extraordinary high capacity of for example lithium-silicon alloy ($Li_{4.4}Si$, corresponding to 4200 mAh/g), a material which otherwise breaks down after a few cycles due to enormous volume changes. Nanostructured forms of carbon, such as carbon nanotubes have also been explored as intercalation materials for Li-ion cells. Further, the discovery of conversion reactions, producing nanocomposite materials from the electrochemical reduction of oxides such as CoO and CuO against lithium

metal electrode, is highly interesting as it enables the reconsideration of non-intercalating and therefore previously discarded electrode materials [27]. Nevertheless, much work is still required to commercialise these innovative technologies and they will probably not be available for some years to come.

2.4 Solid electrolyte interphase

The notion of a solid electrolyte interphase has been briefly described previously; however, here it will be thoroughly examined. All Li-ion cells feature a solid electrolyte interphase (SEI) on the electrode surfaces exposed to the electrolyte, primarily formed during the initial cycle [12]. As this work has focussed on graphite materials, the SEI formation on the graphite electrode surface will be discussed. The SEI is a result of the thermodynamic instability of electrolyte components at low and high electrochemical potentials vs. Li/Li^+ [13], causing them to irreversibly reduce and decompose on the electrode surfaces. The decomposition products develop an inhomogeneous layer between the electrolyte and the electrode with thickness ranging from a few nanometres up to tens of nanometres. The SEI is a passivating film preventing further electrolyte reduction and the presence of a stable and effective SEI is therefore crucial for high battery performance [12]. Particularly, the SEI prevents solvent molecule co-intercalation (of for example PC) into the graphite structure and their subsequent decomposition which leads to graphite exfoliation [28]. Nonetheless, SEI formation involves an irreversible capacity loss as Li^+ ions are incorporated and immobilised in the resulting layer, clearly observed in voltage-charge curves, for example Figure 3. Additionally, the properties of the SEI significantly influence cycleability and rate capability along with thermal stability and safety. Since the SEI substantially affects the resulting thermal properties of Li-ion cells, the relevant influences determining the properties of the SEI layer will be presented in the following [12]. The SEI is located between the electrolyte and the electrode material and hence it is rational that the properties of these will be most influential.

2.4.1 Influence of the electrolyte composition on the SEI

The composition of the SEI is dependent on several factors, yet first and foremost the electrolyte composition. Numerous SEI components are known to occur only for specific electrolyte solvents. Still, there is no consensus regarding the specific SEI compositions and the exact influence of the electrolyte. The SEI composition is highly sensitive to many factors, and due to the different working conditions in the labs studying Li-ion battery systems, the proposed compositions have varied accordingly.

Nevertheless, some general features and major SEI components present for specific electrolyte compositions have been identified [12].

Generally, the layer is believed to be of a very complex nature, consisting of several inorganic and organic species distributed in an inhomogeneous fashion [12]. Several models have been proposed of its structure. Most of these agree that the inorganic components are primarily situated near the graphite in a dense and thin layer. The organic and polymeric components are located on top of this layer, i.e. close to the electrolyte, in a more porous manner [29]. The inorganic species are a result of salt degradation while the organic species stem from the reduction of electrolyte solvents. Common SEI components are lithium fluoride (LiF), lithium oxide (Li_2O), lithium carbonate (Li_2CO_3), lithium alkyl carbonates ($ROCO_2Li$) and lithium alkoxides (ROLi). One of the proposed SEI structures, comprising micro-phases of different compositions, is shown in Figure 11. Another suggested structure is a more layered arrangement of the inorganic and organic components as described above, in which crystals of LiF are present [12].

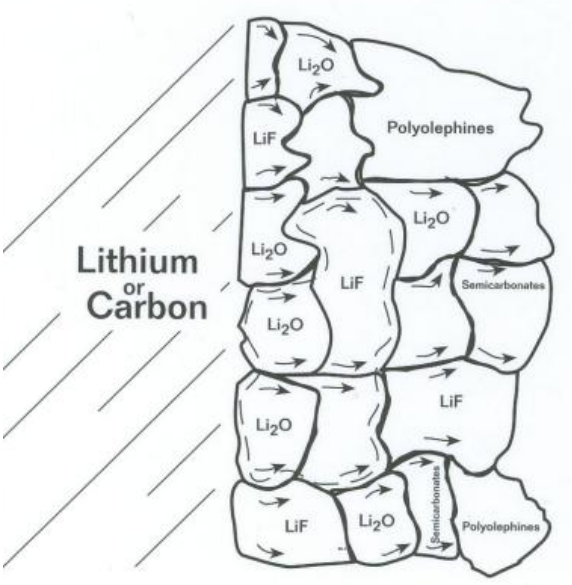

Figure 11: Proposed structure of SEI layer consisting of micro-phases [30].

The reduction products and resulting SEI compositions from common electrolyte solutions have been investigated in the literature. The SEI composition resulting from cycling a graphite electrode with 1:1 EC:DEC electrolyte solution and 1M $LiPF_6$ was analysed by means of Fourier transform infrared spectroscopy (FTIR) by Aurbach et al. [31] in 1995. They found that the SEI mainly consisted of $(CH_2OCO_2Li)_2$, the major EC reduction product, $ROCO_2Li$ and also traces of Li_2CO_3.

However, in recent studies, it has been suggested that Li_2CO_3 is merely a reaction product of semicarbonates with water or CO_2, and thus not an inherent SEI component [12]. For example in 2008, Kang et al. [32] did not identify Li_2CO_3 as part of the SEI. On the other hand, ROLi, lithium alkyl phosphate and lithium fluorophosphates, the two latter probably resulting from $LiPF_6$ decomposition, were detected by FTIR and X-ray photoelectron spectroscopy (XPS). They used electrolyte containing EC and EMC, $LiPF_6$ as salt and graphite electrodes manufactured without polymer binder to simplify the compound characterisation. Andersson and Edström [33] also detected LiF, a $LiPF_6$ reduction product, present as crystallites in the SEI layer in Li/graphite half cells containing EC-DMC based electrolyte.

The effect of VC as an additive was investigated by Aurbach et al. in 2002 [34]. They found that the addition of VC in the electrolyte reduced irreversible capacity loss, inhibited salt reduction and improved the cycling behaviour. These effects were attributed to the reduction products of VC, being polymeric species, that contributed to a more flexible and protective SEI layer. Because of this, VC is a common additive present in many electrolyte compositions and, together with EC, the most utilised electrolyte component with the main purpose of creating an effective SEI layer.

2.4.2 Influence of the graphite on the SEI

The graphite, being the surface on which the SEI is formed, has substantial effect on several of its parameters. For example, Winter et al. [17] in 1998 showed that irreversible capacity loss caused by SEI formation was approximately linearly proportional to the specific surface area of the graphite material, as measured by the Brunauer-Emmett-Teller (BET) method. Applying the knowledge that SEI is formed on any electrode surface exposed to electrolyte, this finding is quite logical. However, they also indicated that the particle size and morphology could have an effect on the observed capacity loss. The decomposition reactions occurring on the edge plane of the graphite particles apparently contributed much more to the capacity loss than those occurring on the basal plane. Accordingly, crystallographic properties such as the ratio of basal to edge plane area would have substantial effect on the SEI and finally on the Li-ion cell. This finding has later been verified by other studies, for example by Zheng et al. [35] in 1999, where the significance of the crystallographic structure and particle morphology on the irreversible capacity loss was emphasised. A systematic study by Placke et al. [36] from 2012 further investigated the importance of the ratio of basal plane to “non-basal plane” surface area on the irreversible capacity loss. They found that the irreversible capacity loss increased nearly linearly with increasing ratio of “non-basal plane” surface area, and logically

decreased similarly with increasing ratio of basal plane area. In conclusion, the prevalent graphite surface type (edge or basal) might have just as much significance as the specific surface area on the extent of SEI formation and irreversible capacity loss.

The relation between specific surface area, SEI formation and subsequent irreversible capacity loss has implications on the type of graphite chosen for specific applications. Naturally, the specific surface area of the graphite increases by decreasing particle size, due to relatively fewer atoms being located in the bulk of the particles. Accordingly, the amount of SEI, and thus the irreversible capacity loss, increases similarly. Generally, graphites engineered for power cells, comprised of smaller particles, are expected to exhibit lower capacity due to higher irreversible capacity loss than for high-capacity graphites. This trade-off situation is a representative example of the many factors that have to be balanced in the manufacture of Li-ion cells for specific applications.

The spatial distribution of SEI components and morphology on a highly ordered graphite electrode were examined by Peled et al. [37] in 2004. The composition of the SEI was highly dependent on whether it had been formed on the basal or edge plane surface of graphite particles. The SEI formed on the edge planes contained nearly only LiF and nearly no Li_2CO_3. The basal plane SEI, on the other hand, consisted mainly of polymeric material, some carbonates and almost no LiF. It was concluded that the organic components preferred to adsorb on the basal plane, while the inorganic components (typically salt reduction products) preferred to adsorb on the edge plane. A more recent study from 2010 by Yan et al. [38], based on thermodynamic principles, supports this finding. Additionally, the SEI formed on edge planes was reasoned to be thicker than that formed on basal planes.

The presence of active reduction sites, i.e. nano-scale defects such as vacancies and dislocations, on the surface of graphites particles influences the SEI formation. Novák et al. [28] emphasised the importance of such sites on the SEI formation occurring during the initial lithium intercalation. The cumulated surface area of different types of defects present at the carbon surface was related to the concept of active surface area (ASA), an intrinsic feature of the carbon. The specific ASAs of Timcal SLX30 graphite samples subjected to different atmospheres and temperatures were determined by means of O_2 chemisorption, as surface oxide complexes were formed at the active sites area. The structural ordering of the graphite surface was reasoned to be inversely related to the ASA, meaning a lower ASA correlated with less surface

defects and thus higher structural ordering. The study showed that higher ASA values resulted in less exfoliation of the graphite. Higher ASA of the graphite surface brought about higher reactivity of the surface towards electrolyte components, which ultimately led to improved surface passivation by SEI formation. In contrast, graphite with low ASA showed low reactivity towards the electrolyte and this slowed down the kinetics of the surface passivation. Consequently, the passivation process would not be completed before the onset of electrochemical exfoliation. The exfoliation process would break up the graphite structure and expose fresh graphite to the electrolyte. The following film formation process (similar to SEI formation) consumed charge and increased the irreversible capacity loss. In the worst case, such exfoliation could render the Li-ion cell useless.

Larger scale surface defects, such as cracks and particle edges, also affect the SEI morphology and stability. Such sites often act as catalytically active sites for solvent reduction due to high current density, and on a larger scale, these defects may lead to less uniform and possibly less stable SEI layer [12]. A former study by the author supports this, as two graphite materials composed of flaky particles with many large-scale surface defects were less thermally stable, probably partly due to their SEI layer, than a graphite material comprising potato-shaped particles with smoother surface [39].

2.4.3 Dynamics and sensitivity of the SEI

It has been shown that both the structure and chemical composition of the SEI layer are not static, but rather changes during cycling and with time. Using XPS, Bryngelsson et al. [29] found that the SEI layer was significantly thinner for de-lithiated graphite electrodes than for lithiated graphite electrodes after three cycles. Furthermore, they discovered that the presence of Li_2CO_3 and semi-carbonates was more pronounced in the SEI layer on de-lithiated graphite than on lithiated graphite after 50 cycles. Andersson et al. [33] investigated how storage of cycled graphite electrodes at elevated temperatures influenced the SEI composition and morphology. After storage, the SEI was more porous, possibly due to partial melting or dissolution of soluble species, and/or decomposition of metastable semicarbonates to form stable Li_2CO_3. In a recent study, Smith et al. [40] used a high precision battery charger to carefully examine the coulombic efficiency and capacity development of Li/graphite coin cells cycled at low rates. By directly correlating the capacity reduction to SEI growth, it was discovered that the SEI grew as a function of the square root of time, $t^{1/2}$. In other words, time, not cycle count, dominated the loss of Li^+ in Li-ion cells cycled at low rates. Above all, this study settles that the SEI is not

completely formed in the first charge-discharge cycle, but will continue to grow, probably during the entire lifetime of the battery.

The majority of the SEI components are highly sensitive to contamination, air and humidity. Furthermore, trace moisture present in for example electrolyte components could cause the decomposition or hydrolysis of $LiPF_6$ to produce hydrogen fluoride, PF_5 and POF_3. These components could then render the electrolyte unstable, particularly at high temperatures [41].

2.5 Thermal instabilities of Li-ion batteries

As briefly mentioned in the introduction, current commercial Li-ion batteries are inherently thermally unstable. However, this issue arises first when the battery is exposed to elevated temperatures. Well-functioning small batteries operating at normal loading at room temperature will be completely stable, but a faulty battery or abusive behaviour can lead to short-circuiting or overcharging that will cause the battery temperature to rise and make the thermal instabilities relevant. Large batteries for electric vehicles also require cooling systems as the operation of these will generate heat by itself [42]. Furthermore, cells in battery packs consisting of many cells connected in series and in parallel may be overcharged without abuse. This can be explained by minor differences within the cell parameters. The cells can thus develop different states of charge at the same voltage after a period of operation, which could lead to some cells being overcharged [43]. A significant temperature increase can cause exothermic reactions to start inside the cells. These could increase the cell temperature even further, initiating other exothermic reactions. In the worst case scenario, uncontrolled temperature rise occurs, termed "thermal runaway". Thermal runaway describes a situation inside the battery where the heat output from the reactions exceeds the heat dissipation from the battery [9]. The reactions and their relations to the graphite material, electrolyte and SEI will be discussed in the following.

2.5.1 Exothermic reactions occurring in Li-ion cells

The exothermic reactions occurring inside Li-ion batteries have been studied by means of different thermal analysis techniques, e.g. differential scanning calorimetry (DSC), which will be explained in detail in chapter 2.7. The possible exothermic reactions in a Li-ion battery have been summarised by Tobishima [9]. In order of relevance, they are:

1. Chemical reduction of the electrolyte at the surface of the negative electrode, i.e. SEI formation
2. Thermal decomposition of the electrolyte
3. Chemical oxidation of the electrolyte at the surface of the positive electrode, i.e. SEI formation
4. Thermal decomposition of the negative electrode
5. Thermal decomposition of the positive electrode

In addition, when the polymer separator melts, occurring at about 125°C for a standard polyethylene separator, a large heat evolution might be generated by internal short-circuiting. Furthermore, several studies [12, 30, 32, 33, 35, 39] have proposed that exothermic reactions occur inside the SEI layer at elevated temperatures, leading to its transformation. Lastly, it should be noted that each of the above points could comprise several reactions. The chemical reduction of the electrolyte, for instance, is likely to occur in several stages as each electrolyte component is reduced separately.

Verma et al. [12] claimed that the two most important exothermic reactions occurring on raised battery temperature were the transformation of the SEI layer and the subsequent reaction of the active electrode material with the SEI or directly with the electrolyte. The thermal stability of Li-ion batteries could thus be largely attributed to the stability of the SEI layer [44].

2.5.2 Thermal studies on graphites in specific cell combinations

Through the last two decades, many studies have investigated the thermal stability of graphite anodes with electrolyte in Li-ion cells and the specific reactions involved, and some representative results will now be presented.

In 2002, Yamaki et al. [44] conducted a DSC study on the thermal stability of fully lithiated graphite that had been electrochemically cycled two times in a half cell with electrolyte composed of 1M $LiPF_6$ dissolved in EC and DMC. A minor peak in the DSC curve signifying an exothermic reaction occurred at 140°C and was attributed to a reaction between the electrolyte and lithiated graphite causing SEI formation. The authors reasoned that the swelling of poly(vinylidene fluoride) (PVDF) binder material in the electrode at this temperature exposed lithiated graphite to electrolyte and initiated the reaction. The presence of PVDF binder thus prevented complete SEI formation and passivation of the entire graphite surface at a lower temperature. A modest heat generation from 130°C continued after the small peak until the

temperature was 280°C. This was ascribed to the continued reaction of lithiated graphite with the electrolyte, forming new SEI. At 280°C, the SEI finally broke down and directly exposed the lithiated graphite to the electrolyte which produced a sharp exothermic peak in the DSC curve.

In a more recent work from 2011, Haik et al. [45] reported the thermal behaviour of three commercial graphite materials in electrolyte solutions containing EC, EMC, DMC and $LiPF_6$. On the whole, three thermal features were observed in the cycled and fully lithiated graphites:

1. From 80 to 120°C: mild heat generation from the transformation of the SEI.
2. From 120 to 180°C: slight exothermic response caused by reactions between the lithiated graphite and the electrolyte solution continuously forming new SEI.
3. Above 200°C: a significant thermal response containing two exothermic reactions separated by an endothermic process. The first exothermic reaction was ascribed to the decomposition of the electrolyte. The authors suggested that the endothermic response was a result of co-intercalation of EC molecules into the graphite structure. The subsequent formation and decomposition of lithiated graphite-EC intercalation compounds could exfoliate the graphite structure and produce an endothermic response. This process promoted the final exothermic peak, caused by further thermal decomposition of the electrolyte and the PVDF binder.

The heat evolution occurring from 80 to 120°C was supported by an extensive reaction mechanism proposal. Exothermic reactions between intercalated Li^+ and several SEI species, producing metastable compounds such as lithium carbonate, were particularly important and could initiate further thermal reactions. DSC data supported that the presence of intercalated Li^+ was a requirement for such reactions, as the SEI on completely de-lithiated graphites did not participate in thermal processes between 80 and 120°C. Li^+ was gradually consumed in these reactions which brought about a reduced degree of intercalation in the graphite structure. The other proposed reactions in the reaction scheme, including the decomposition of $LiPF_6$, finally produced two stable species, LiF and LiO_2, neither of which formed an effective protective layer on the graphite surface. Consequently, weak exothermic reactions involving the reduction of solvent molecules on the lithiated graphite surface continued until 180°C.

The presence of an endothermic reaction contributes interesting information about the processes in the graphite electrode at elevated temperatures. The graphite exfoliation causing the endothermic peak is, as previously mentioned, probably caused by co-intercalation of solvent molecules, especially EC, in between the graphene planes of the graphite structure. In fact, the authors proposed that the presence of EC in the electrolyte was important, possibly a requirement, for the exfoliation process. The formation of the ternary graphite intercalation compound (GIC) $Li(EC)_yC_x$ is thus thermodynamically favoured at potentials higher than the intercalation of Li^+ into the graphite. The decomposition products from such compounds include gases such as CO_2 and C_2H_4. It is this gas evolution, increasing the pressure between the graphene layers, which ultimately causes the graphite structure to exfoliate. The significance of particle morphology and crystallographic structure was emphasised by the authors. Particularly, the ratio of basal to edge planes was deemed to be important for the magnitude of the exfoliation process. A higher fraction of basal sites on the particle surface might hinder gas diffusion from the interior of the graphite structure which could bring about enhanced pressure increase and greater degree of exfoliation. In the study, it was observed that a flaky particle graphite type with higher basal plane area experienced more significant morphological changes and consumed more heat due to the exfoliation than a graphite material with rounder particle shape. However, the increased exfoliation subsequently exposing fresh graphite directly to the electrolyte could also result in a larger exothermic reaction afterwards. Nonetheless, the researchers pointed out that the endothermic process caused significant self-cooling of the Li-ion cells, which could affect the triggering and evolution of thermal runaway under similar conditions. The endothermic DSC response, along with the other thermal responses described above, is shown in Figure 12.

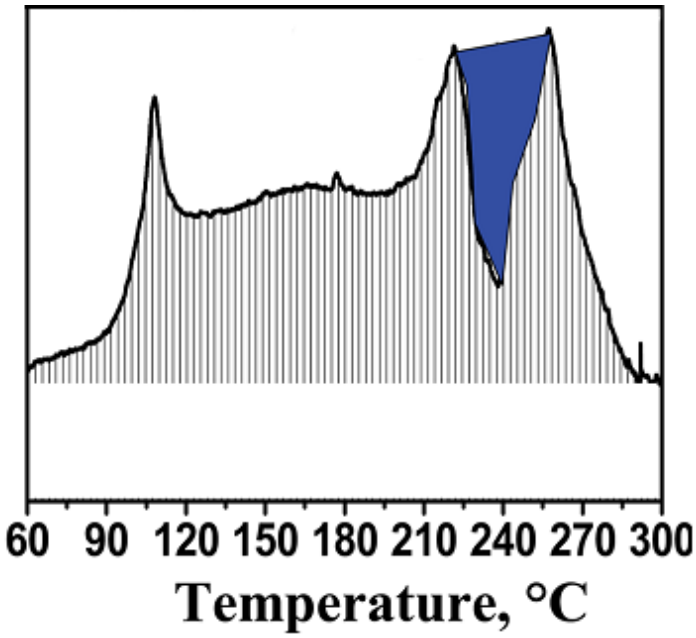

Figure 12: Typical DSC curve from the study by Haik et al. [45] showing the three thermal features described above, the endothermic process indicated with blue. The maximum exothermic response height corresponds to about 0.5 W/g.

On the basis of a thorough quantitative DSC study on several graphite materials and binders, Roth et al. [46] found that the binder type and level had small influence on the thermal stability of the anodes. Instead, the reaction enthalpies increased with increasing surface area of the graphite materials and especially with increasing state of charge. Notably, an exothermic peak occurring at 280°C was not present in the graphite electrodes when the cell was only charged 50%. Presumably, this could be explained by of the consumption of Li^+ in previous reactions, also suggested in the study by Haik et al. [45] and discussed above.

A former study by the author of the current work reported and compared the thermal stability of three graphite materials, using 1:1 EC:DEC and 1:1 EC:DEC + 1 wt% VC with 1M $LiPF_6$ as electrolytes [39]. Similar thermal features as those discussed in Haik et al.'s [45] article were found, except for a major exothermic response caused by leakage from the sample pans. Two Elkem materials were found to be less thermally stable than Timcal SLP30. This could largely be attributed to the specific surface area and particle morphology of the graphites. The graphites with higher specific surface area generated more heat, since these were covered with more SEI. Furthermore, the findings supported that potato-shaped particles were likely better substrates than flaky particles for the formation of stable SEI, due to the inherent cracks and sharp edges of the latter. Finally, the addition of VC to the

electrolyte improved the surface chemistry of the SEI layer, and significantly reduced the heat generation from the SEI transformation.

More DSC studies on the thermal stability of graphite electrodes are presented as supportive material in appendix B.1.

2.5.3 Summary of thermal studies on graphite materials

From the above studies and those described in appendix B.1, it is evident that there are substantial variations within the analyses conducted on the thermal stability of graphite materials for Li-ion batteries. As previously mentioned, the properties of Li-ion battery components, among them also the thermal stability, are highly dependent on several parameters. Particularly this is true for the SEI layer, which additionally is not possible to influence directly during battery manufacture. Slight variations in laboratory conditions can lead to significantly different thermoanalytical results, especially with respect to the onset temperatures of the reactions and their magnitudes [46-49].

Nonetheless, certain trends seem to be common among most of the studies. At relatively low temperatures, around 100°C until around 200°C, the composition of the SEI layer is transformed from metastable compounds to more stable compounds. In the DSC analyses, this transformation is observed as a mild exothermic response. Notably, there are indications that the presence of Li^+ inside the graphite structure is a requirement for this transformation. Unlike the initial SEI layer, the transformed layer does not provide complete passivation of the lithiated graphite surface. Consequently, the electrolyte continuously reacts with the lithiated graphite through the SEI layer in the same temperature interval, adding to the observed exothermic response. Above 200°C, the electrolyte starts to decompose and contributes to a significant exothermic response. However, it can also result in an endothermic exfoliation of the graphite structure caused by co-intercalation and subsequent decomposition of electrolyte molecules inside the lithiated graphite structure. Combined with the breakdown of the SEI layer, this exfoliation leads to direct exposure of fresh lithiated graphite surface to the electrolyte, observed as the final large exothermic peak present in most studies. Further decomposition of the electrolyte species and the PVDF binder is also believed to contribute to the final peak.

To summarise, the most important parameters relevant for the thermal stability of graphite materials considered in the literature are:

- Graphite material properties; specific surface area, morphology and crystallographic structure
- Electrolyte composition
- Degree of Li^+ intercalated in the graphite structure
- Properties and stability of SEI layer, which again depends heavily on all the above points

Finally, it is crucial to note that most of the parameters influencing the thermal stability of anode materials cannot be treated independently, as their interactions are equally, and sometimes more significant. Analysis of the thermal behaviour of anode materials requires a similar approach, since most of the underlying processes result from several effects and their relations.

2.6 Low temperature operation of Li-ion batteries

The global use of Li-ion batteries, involving a range of different applications, is predicted to increase in the coming years due to rapidly emerging applications, such as the powering of electric and hybrid electric vehicles. This development increases the requirements to the batteries. As Li-ion batteries can be used in arctic as well as tropic regions on the planet, particularly the temperature range over which the batteries are useable becomes crucial. For example, in Norway, where electric vehicles are quickly becoming popular city vehicles, the temperature can easily vary between -20°C in winter and 25°C during summer. Furthermore, for military or space applications, the temperature requirements are even more extreme. In fact, research groups have in recent studies claimed that Li-ion batteries should function acceptably over a wide temperature range from -40 to +60°C in order to meet these new requirements [7, 50]. The main challenge in this work has been to improve the low temperature performance of Li-ion batteries, especially with respect to the kinetics of the electrochemical processes. Particularly the performances of the electrolyte and surface films have suffered at low temperature operation, and the research effort has been directed accordingly. In the following, the key issues regarding low temperature operation of Li-ion batteries will be presented, followed by examples of the work conducted on electrolyte and graphite electrode optimisation.

2.6.1 Kinetic limitations at low temperature

Until recently, the performance of Li-ion batteries has been considered poor at low temperatures, i.e. temperatures below -20°C and approaching -40°C. Actually, the

temperature range for optimal operation is only from ca. 20 to 40°C [51]. The key reason for this has been kinetic limitations of various transport processes occurring inside the cells. Mainly, these limitations have been related to poor electrolyte conductivity, slow Li^+ transport through the SEI layer covering the electrodes and poor Li^+ diffusion through the surface layers and bulk of the electrodes [7]. Particularly, Li^+ desolvation, migration through the surface films as well as the interfacial charge transfers between solution, surface films and graphite material all affect the overall Li^+ insertion/de-insertion kinetics [50]. These processes are schematically illustrated in Figure 13. Of these parameters, the electrolyte properties are presumably the most dominant, as sufficient conductivity is necessary for good low temperature performance. Unfortunately, the electrolyte conductivity is also often the property that suffers most at low temperature. As described in chapter 2.3.1.1 and specifically in equation (2.4), ion mobility is an essential parameter to obtain high electrolyte conductivity. The mobility of ions in an electrolyte solution is logically dependent on the viscosity of the solution; molecules and ions will move slower in a viscous solution. Accordingly, maintaining low viscosity and thus high ionic mobility of the electrolyte even at low temperatures has been the key interest in order to improve the low temperature performance of Li-ion batteries [7].

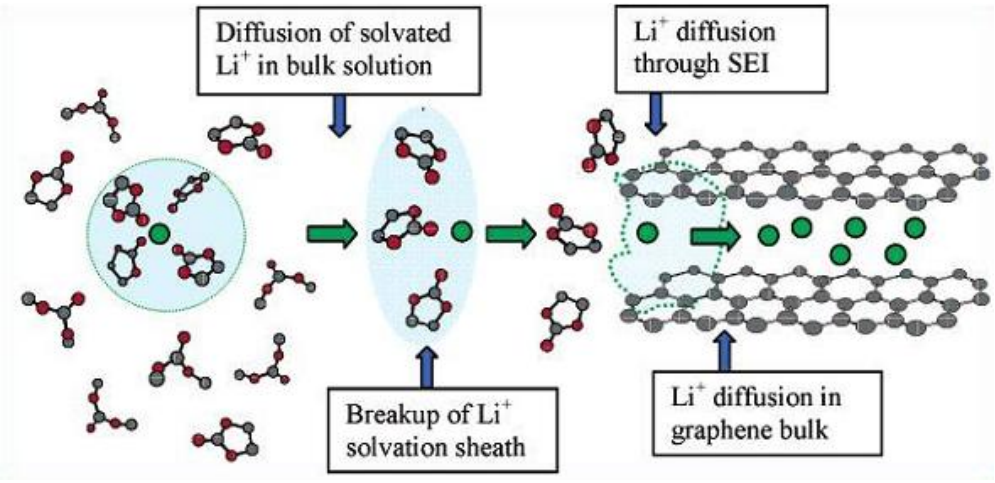

Figure 13: Schematic illustration of the journey of a Li^+ ion (green particle) from the electrolyte solution into the graphene bulk, emphasising the main energetic barriers [20].

2.6.2 Electrolytes for improved low temperature performance

The standard electrolyte formulations often employed both in research and in commercial batteries have commonly been binary mixtures composed of a cyclic and a linear alkyl carbonate. As pointed out by Yaakov et al. in 2010 [50], particularly EC-DMC electrolyte mixtures have exhibited a good balance of beneficial properties,

including high oxidative stability, effective passivation of graphite electrodes and consequently a very good cycle life at room temperature. However, these electrolytes cannot operate below -20°C, mainly due to the solidification of the EC component (melting point at 36°C) in the binary solvents system and the increasing order of the electrolyte at low temperatures, increasing the viscosity. In fact, the required presence of EC as a superior SEI forming agent and Li^+ coordinator is also the most significant electrolyte problem with respect to low temperature performance. Consequently, either reducing or replacing the EC component would be necessary to improve the low temperature performance. In addition, adding more co-solvents to create ternary or even quaternary mixtures has been known to improve the conductivity, also at low temperatures, because of a disordering effect of the electrolyte [21]. The effects of partially replacing EC with PC have been widely studied, because of the improved low temperature properties of the latter. Particularly, the transport properties of the SEI layer were found to improve at lower temperatures by incorporating PC instead of EC [52]. However, its use should be limited as PC is known to exfoliate the graphite structure [15]. Two recently published articles have examined the main paths towards enhanced low temperature performance, i.e. reduction of the EC-content and addition of alternative electrolyte components.

The research group of Smart [53], which has studied electrolytes for low temperature operation for more than 15 years, conducted a systematic examination of the effect of various ester co-solvents in 2010 [7]. Their structural formulas are provided in Figure 15. Three-electrode cells with MCMB carbon anodes, $LiNi_{0.8}Co_{0.2}O_2$ cathodes, and lithium reference electrodes were tested with several novel electrolytes. These electrolytes were based on a recipe 20:60:20 (wt.) with EC, EMC and an ester co-solvent, respectively, and $LiPF_6$ as solute. The authors found that fixing both the EC- and ester co-solvent contents at 20% produced battery systems with wide operating temperature range. The main purposes of EC and the ester co-solvent were, respectively, to form effective SEI layer and improve viscosity and thus conductivity at low temperature. The performance of the novel electrolytes were compared to all-carbonate based baseline electrolytes at temperatures down to -60°C. All the Li-ion cells performed reasonably similar at -40°C when discharged at moderate rate (~C/16). However, when using a discharge current corresponding to complete discharging in four hours (C/4), the ester co-solvent electrolytes performed dramatically better than the baseline electrolytes. The baseline electrolyte solution delivered 5% of room temperature capacity, while the best ester co-solvent electrolytes provided over 60%, as can be seen in Figure 14. Hence, the ester co-

solvents significantly improved the rate capability at low temperature. Upon discharge at even lower temperatures, -50 and -60°C, the same trend was observed, as the ester co-solvent electrolytes outperformed the baseline electrolytes.

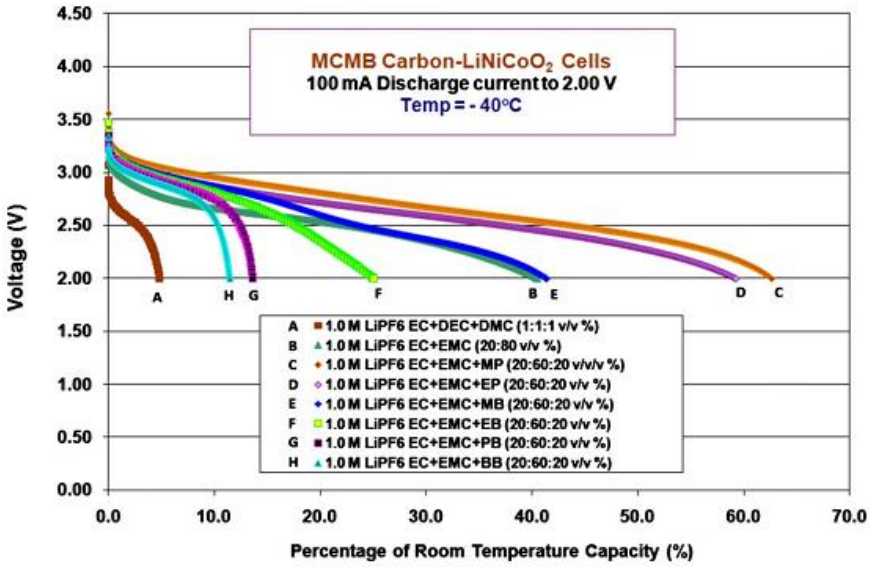

Figure 14: Discharge capacity of cells with the different electrolyte compositions at -40°C using a rate of C/4, showing the considerable increase when employing the novel electrolytes [7].

Various electrochemical measurements, including electrochemical impedance spectroscopy, were employed to attempt to reveal the explanation for the superior performance exhibited by the ester co-solvent electrolytes. Improved mass-transfer characteristics due to higher ionic conductivity and faster Li^+ intercalation/de-intercalation at the interfaces due to favourable film formation at the electrode surfaces were suggested to be the most important reasons. High capacity (7 Ah) aerospace quality Li-ion cells were fabricated using baseline electrolytes and the three most promising ester co-solvent electrolytes in order to compare their performances in a specified application. Once again, the novel electrolytes proved superior. As an example, the cell containing the methyl propionate-based electrolyte delivered 72.3% of room temperature capacity (5.78 Ah) at -50°C using C/5 discharge rate, a six-fold improvement over the baseline electrolyte.

Problems related to using ester co-solvents are the stability at elevated temperatures and stability against oxidation. Smart et al. [7] anticipated the higher molecular weight esters, due to their higher boiling points and general high temperature stability, to perform better at high temperatures than low molecular weight esters. However, they had not yet conducted research to verify this. Also, the use of esters is

known to worsen the oxidative stability of electrolyte solutions relative to common binary mixtures, such as EC-DMC [50].

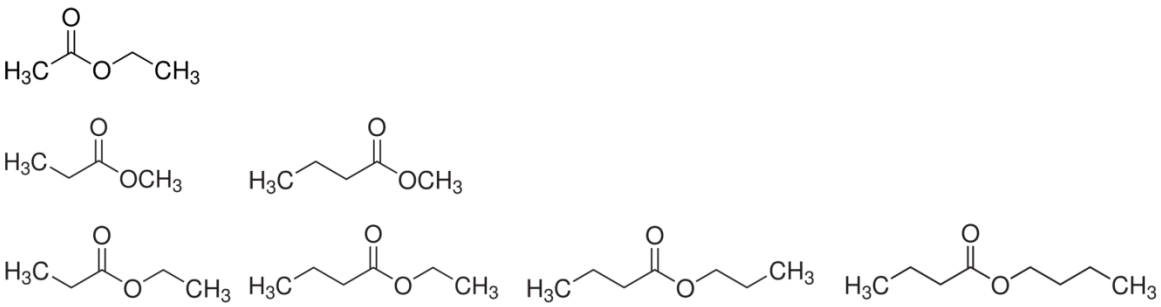

Figure 15: The ester co-solvents examined by Smart et al [7]. Top part: Ethyl acetate. Middle part from left to right: methyl propionate, ethyl propionate.
Bottom part from left to right: methyl butyrate, ethyl butyrate, propyl butyrate, butyl butyrate. Structural formulas are taken from Sigma-Aldrich's website [54].

In a similar study by Yaakov et al. [50], the performance of ten different electrolyte solutions and three different graphite materials were studied over a wide temperature range, from -40 to 60°C. EC-DMC was chosen as the basic system, into which several other co-solvents were added in different amounts as well as a range of different solutes. Coin cells with disk-shaped graphite electrodes, metallic lithium disk counter electrodes and porous polypropylene separator soaked with the selected electrolyte solutions were assembled for cycling between 30 and -40°C in steps of 10°C. Additionally, the specific conductivity of the electrolytes was measured for temperatures between 60 and -40°C. The authors claimed that any electrolyte should show conductivity not less than 1 mS/cm even at low temperatures, a requirement which all the selected compositions fulfilled at -40°C. They also found that the presence of electrolyte additives, such as VC and LiBOB, at low concentrations did not deteriorate the conductivity and general low temperature performance. Consequently, these additives could be utilised for improving the passivation of graphite electrodes both at low and high temperatures.

The initial irreversible capacity losses when using the various electrolyte solutions were comparable to the losses when using the basic electrolyte. The authors therefore argued that the addition of a third or even fourth alkyl carbonate or ester component to the basic system did not alter the surface reactions on the graphite, which was dominated by the reduction of EC. This finding verifies that electrolytes optimised for low temperature use also have acceptable room temperature properties. The electrolyte composition, however, strongly influenced the

temperature dependency of the capacity. This variation could be related to the passivation quality of the graphite electrodes, and the consequent transport properties of the passivating surface films.

On a more fundamental level, Ding et al. [55-57] conducted very thorough and systematic DSC studies on binary, ternary and even quaternary mixtures of the most common carbonates in electrolytes to develop phase diagrams. These studies are highly useful, as they readily show the melting points of the mixtures and at which temperatures components are expected to solidify, thus providing the temperature range of operation for a given electrolyte composition. Even though the studies were performed mostly on salt-free solutions, Ding also showed that, in general, increasing the salt concentration in an electrolyte reduced the phase transition temperatures. Figure 16 shows a typical phase diagram resulting from DSC analysis of different compositions in the EMC-EC binary system, including the effect of adding different concentrations of salt to one specific composition.

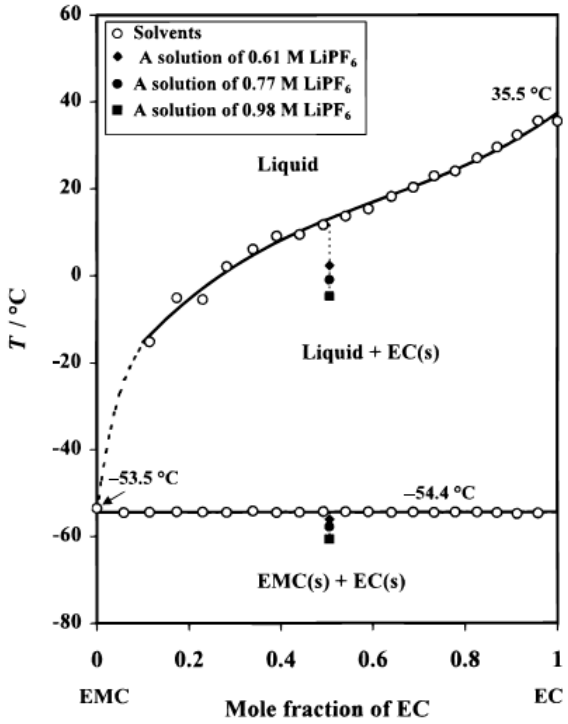

Figure 16: Liquid-solid phase diagram of EMC-EC. Open dots represent measured data and the lines are obtained by data fitting. The dotted line is an estimated extension of the liquidus curve. The closed dots are data points for different concentrations of $LiPF_6$, clearly showing how the phase transition temperatures are reduced for increasing salt concentration [56].

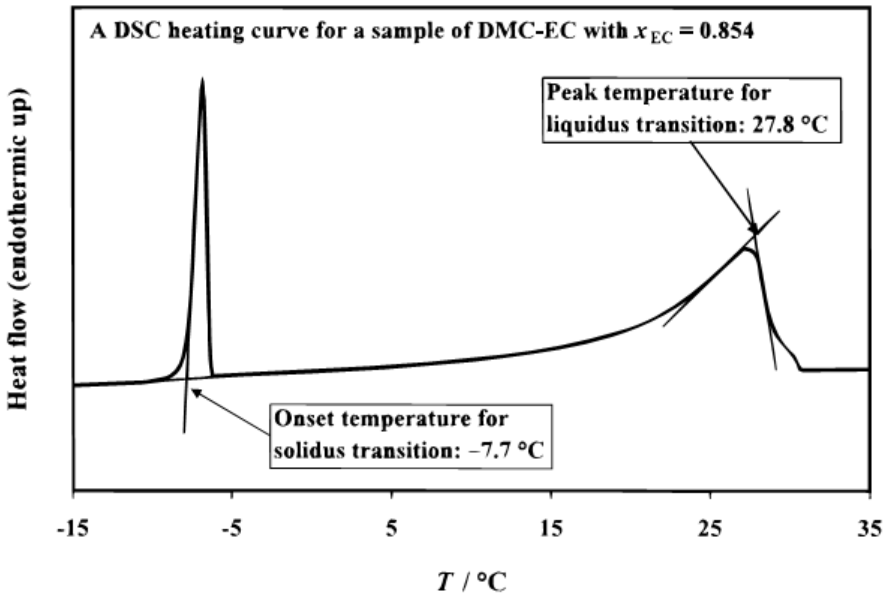

Figure 17: Example of DSC curve from heating solvent mixture of EC-DMC [56].

Figure 17 is an example of a DSC curve from heating a sample of EC-DMC solvent mixture, showing the usual phase transition peaks, and how to determine their temperatures. Notably, all the binary phase diagrams produced by Ding et al. [56, 57] are based on such curves. Upon heating, the solidus transition occurs when the mixture changes from being completely solid to a mixture of solid and liquid, and in the liquidus transition the mixture becomes completely liquid. For a given composition, the solidus and liquidus transition peaks in a DSC heating curve thus correspond to two dots in a phase diagram such as Figure 16.

2.6.3 Graphites for improved low temperature performance

The study by Yaakov et al. [50] also described the low temperature performance of three different graphite materials. Some general graphite characteristics of significance for low temperature performance were identified.

In the study, the graphite with the highest specific surface area provided the highest capacity at low temperature, as well as the highest irreversible capacity loss. It was reasoned that increasing the surface area of the graphite compensated for the slower Li^+ intercalation kinetics at low temperature. Accordingly, increasing the surface area, for example by reducing the graphite particle size, might be a viable path towards improving the low temperature performance of graphite materials. As previously mentioned, such graphites also exhibit high discharge rate capability and are relevant for electrodes in power cells. However, it must be noted that this advantage is at the expense of higher irreversible capacity loss.

From Figure 18 it can be seen that the capacity of the graphite material decayed rapidly as the temperature decreased below 0°C. At -10°C, about 50% of the room temperature capacity was available, while less than 10% could be utilised at -40°C.

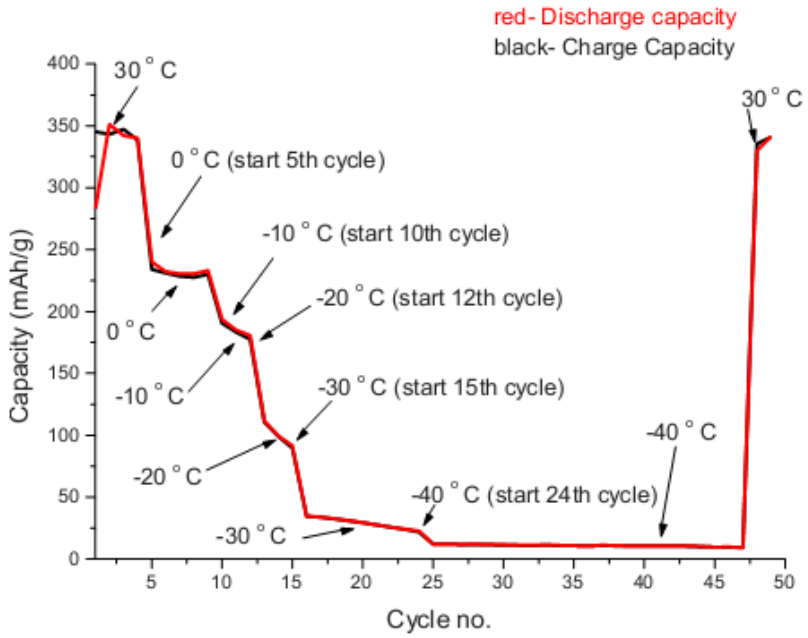

Figure 18: Typical variation of capacity vs. cycle number during the temperature cycling for SLP30 graphite electrodes in an EC:DMC:EMC electrolyte solution with 1M LiTFSI and 1% VC. A current density of C/20 was used for all cycles [50].

Figure 18 shows that the studied graphite electrodes had very low capacity at temperatures below -20°C. According to the authors, Li-ion batteries comprising graphite electrodes and the most relevant electrolyte solutions were not practical for operation at very low temperatures.

2.6.4 Summary of low temperature studies

As supported by the above studies, the main issue regarding low temperature operation of Li-ion batteries is related to the kinetics of the journey of the Li^+ ions through the cell. Largely speaking, the journey can be described by the following processes:

- Diffusion of solvated Li^+ through the electrolyte
- Removal of desolvation sheath surrounding Li^+
- Migration of desolvated Li^+ through the surface films
- Diffusion of Li^+ through the electrode surface and intercalation in the bulk of the electrodes

Logically, all these processes are slower at low temperatures than at room temperature. Consequently, the work to mitigate this problem has revolved around both electrode and electrolyte optimisation. However, studies have shown [7, 21] that the electrolyte component suffers most at lower temperatures, and the main focus of the work has been directed accordingly. Specifically, increasing the electrolyte conductivity at low temperatures has been viewed as an effective way of improving the low temperature operation. To summarise, the methods for improving the electrolyte conductivity have been:

- Reduction of EC component which might precipitate at low temperatures
- Use of additional solvents to create ternary or quaternary electrolyte compositions, as these are less ordered and thus have inherently higher conductivity
- Use of ester co-solvents due to their low viscosity and therefore high conductivity, particularly at low temperatures

Regarding graphite materials, it has been found that simply reducing the particle size of the material is a route towards improving their low temperature performance, even though other parameters, such as capacity, could suffer from it. As it is difficult to enhance the kinetics of Li^+ diffusion in the graphite structure on its own, shortening the diffusion distance inside the material is an obvious choice. However, the method is also significant, as emphasised in the study by Yaakov et al. [50], since the Li^+ kinetics inside the graphite is drastically reduced at temperatures below -20°C.

The difference between the low temperature capacity achieved in Yaakov et al.'s [50] cells and Smart et al.'s [7] batteries is considerable and noteworthy, and probably a result of several factors. Firstly, Yaakov et al. have assembled Li/graphite half cells, while Smart et al. have manufactured three-electrode glass cells (full cells) from spiral rolls of anode and cathode material, using Li as reference electrode. The latter cell type is likely to behave differently than coin-shaped half cells, and could perform better at low temperatures, perhaps because of the different cycling procedure in full cells. In addition, the experience accumulated by Smart's research group over more than 15 years has probably increased the understanding of important factors to build high performing Li-ion cells for low temperature operation.

To the best of our knowledge, there has not been conducted any characterisation of the thermal stability of graphite materials cycled with special electrolytes at lower temperatures. The present work aims at gathering this type of data in order to

determine the thermal stability of some novel electrolytes and the influence of cycling at different temperatures on the thermal stability of the graphite.

2.7 Differential scanning calorimetry

2.7.1 Main principles of DSC

As exemplified in a number of studies referenced in this report [32, 39, 44-49, 58], differential scanning calorimetry (DSC) is the thermoanalytical technique of choice when studying Li-ion battery components. The thermal characterisation in this work was also conducted using DSC. DSC can offer a highly sensitive and rapid thermal analysis of many types of materials. A differential scanning calorimeter specifically measures "the change of the difference in the heat flow rate to a sample and to a reference sample while they are subjected to a controlled temperature program" [59]. A standard DSC achieves this by using thermocouples to measure the temperature difference between the samples, which is proportional to the difference in heat flow rates. The program that changes the temperature with time is set up before the analysis and enables measurable temperature and heat flow differences. Two modes of operation can be utilised in such a program. Isothermal mode maintains a constant heat flow and temperature in the sample, i.e. the change of heat flow is zero, while scanning mode changes the sample temperature linearly with time. Power compensated DSC instruments were employed in this work. As opposed to a standard DSC, two micro-furnaces are utilised in such an instrument to individually heat sample and reference, enabling both to be kept at the same temperature. The measured heat in the sample is compensated with electrical heating power. The compensation energy supplied by the instrument is equal to the heat consumed or generated in the thermal reaction, directly providing the relevant data [59].

2.7.2 Analysing DSC curves

Usually, a DSC analysis output is represented as a curve showing the heat flow rate versus temperature or time, exemplified in Figure 19. Thus, if no thermal processes occur in the sample, the curve will ideally be completely flat. However, because of thermal asymmetry between the sample and reference, this is rarely the case, and the resulting baseline is dependent on sample properties, instrument properties and temperature. So, if no thermal processes of any kind occur in the sample, the heat flow rate curve will only consist of the mentioned baseline. When thermal reactions or transitions happen in the sample, either consuming or producing heat, a peak will appear in the curve. The peak area with respect to the baseline and the gradient of

the curve at any point determine the overall heat generation from the process and the instantaneous rate, respectively. Furthermore, the temperature at which the process initiated can easily be determined. All these parameters are interesting with regards to thermal processes in Li-ion batteries.

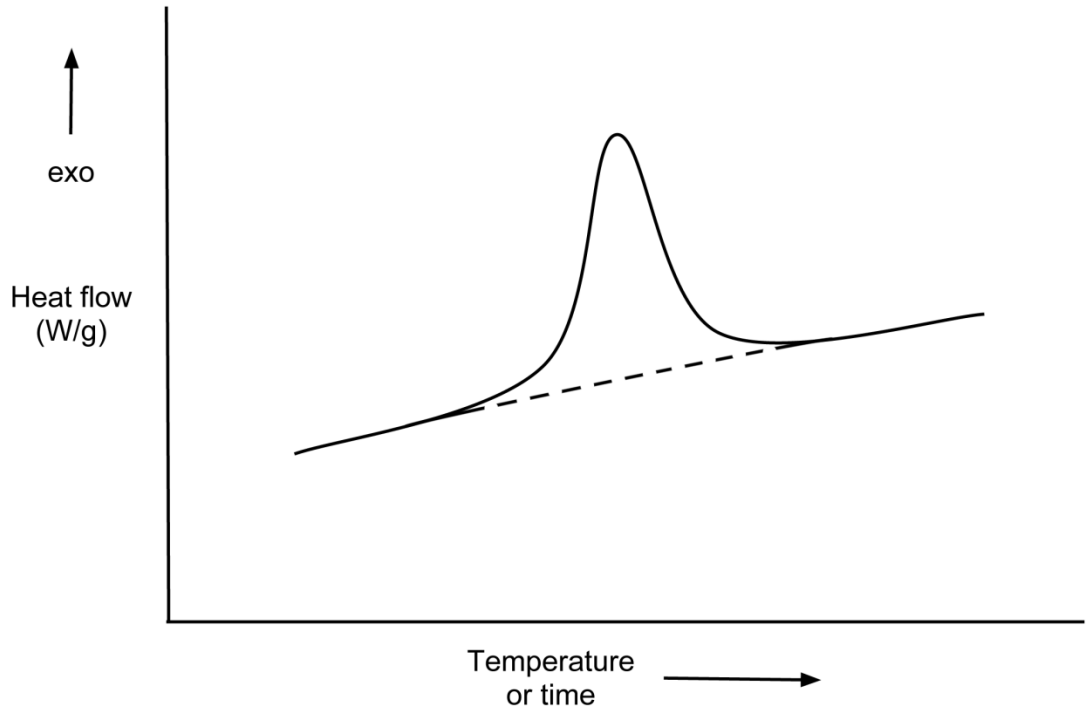

Figure 19: DSC curve featuring an approximately linear baseline (marked with a dashed line) with a positive slope and an exothermic peak.

3 Experimental

The main experimental work conducted for this report can be separated into four parts which will be briefly presented in the following. Firstly, the different graphite materials were tape casted onto copper foils acting as current collectors. This work was partially carried out by others that have been acknowledged. Secondly, cells were assembled utilising the cast material to prepare electrodes. Thirdly, the cells were electrochemically cycled, some at specific temperatures inside a temperature chamber. After cycling, the cells were disassembled and samples for thermal analysis were prepared. Each sample consisted of a part of the cycled graphite electrode and fresh electrolyte, to simulate the conditions inside a functional Li-ion cell. Finally, the thermal analyses were conducted. In addition, the thermal behaviour of pure electrolytes was studied at high temperatures to facilitate the interpretation of the analysis results. The phase transitions of pure electrolytes at lower temperatures were also studied by thermal analysis in order to enhance the understanding of the low temperature cell performance.

SEM analysis and nitrogen adsorption measurements of the graphite materials were conducted to facilitate the interpretation of the cycling and thermal analysis results.

In the following sections more detailed description of the work will be presented. However, in order to facilitate the understanding of the descriptions, first the specifications of the manufactured cells will be provided.

3.1 Cell specifications

In this work, stainless steel (SUS316L alloy) coin cells of 20.25 mm diameter and 1.6 mm height from Hohsen Corp. were used for assembly of Li/graphite half cells. The internal design of the cells is provided in Figure 20. From bottom to top, the coin cell contains the graphite electrode (cathode), a polymer separator, and the lithium counter electrode (anode). The battery case and cap surrounds these components and hermetically seals the cell with a plastic gasket. In order to fill the free space inside the coin cell, a metal spacer is placed on top of the lithium electrode. The assembly process of these cells will be further explained in chapter 3.2.3.

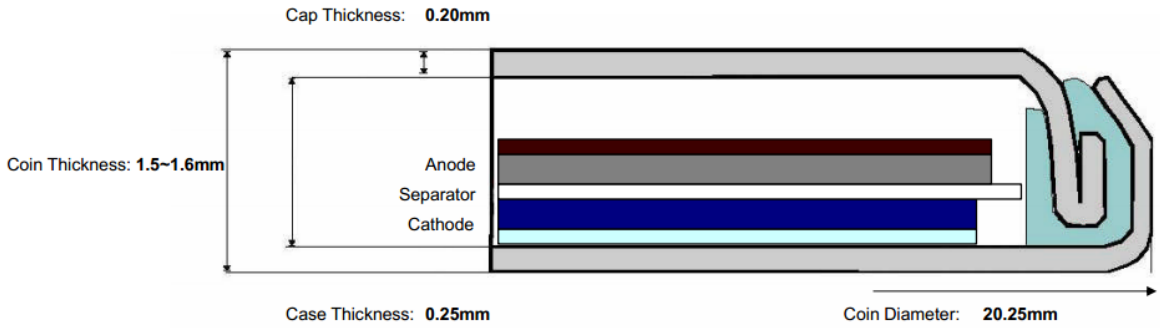

Figure 20: Partial cross section of a crimped Hohsen 2016 coin cell with cell dimensions [60].

In commercial Li-ion cells composed of graphite and lithium metal oxide electrodes, the former acts as anode and the latter as cathode during discharge. However, in the cells manufactured for this work, the situation is reversed. The electrode materials utilised here, graphite and lithium, are both candidates for negative electrode (anode) materials, because of their low electrochemical potential vs. Li/Li^+. Graphite has a positive potential with respect to pure lithium metal and will therefore function as the cathode in the resulting cells. Principally, upon discharge of the batteries, the Li^+ ions will travel towards and intercalate into the graphite electrode. Similarly, upon charging the Li^+ ions will move from the graphite electrode to the lithium electrode. The intercalation mechanism and general performance of graphite electrodes are not dependent on whether graphite acts as anode or cathode, and the results from this work can therefore be applied in standard Li-ion cells. Technically, the coin cells manufactured and analysed here are Li/graphite half cells, and will thus be called cells rather than batteries.

3.2 Cell manufacture

3.2.1 Tape casting of graphite electrode sheet

The graphite electrodes cycled and later analysed were initially prepared as sheets by spreading homogenous slurry on a copper foil. The electrode slurries were prepared by mixing 1-methyl-2-pyrrolidinone (NMP), carbon black, PVDF binder, and Timcal or CPreme graphite powders in certain weight ratios. An overview of technical properties of the analysed graphite materials is given in Table 1, while technical data on the materials used to fabricate graphite electrode sheets can be found in Table 2. The CPreme electrodes contained carbon black, PVDF and graphite in weight ratios of 3:7:90 while weight ratios of 2.5:5.0:92.5 were used to prepare Timcal electrodes. The components for preparing CPreme electrodes were mixed in a mixer mill Retsch MM 2000 into a homogenous slurry which was tape cast onto

copper foil current collectors. The Timcal electrode components were mixed by ball milling. In both cases, the wet film was initially dried on the tape caster for 2 hours at 60°C before placed in a Binder VD 23 vacuum oven overnight at a temperature of 120°C and pressure of 10^{-5} bar. The electrode sheets were finally heated to 80°C for 2 hours in an antechamber while transferred into an argon-filled MBraun glove box. Tape casting theory has been described in detail by Mistler and Twiname [61], while the specific procedures used here are described in appendix C.1. It is assumed that the different slurry preparation methods for Timcal and CPreme electrode sheets have not influenced the performance of the materials and the results presented in chapter 4.

Table 1: Technical properties of graphite materials [62, 63]

Graphite material	BET surface area (m^2/g)	$d_{50\%}$ (µm)	$d_{90\%}$ (µm)	Capacity (mAh/g)
Timcal SLP30	7.5	16	32	>360
CPreme G8	<2.3	6-9	12-18	325
CPreme P5	3-4	4-6	9-13	285-295

$d_{50\%}$ and $d_{90\%}$ are particle size distribution parameters. 50% of the particles are smaller than $d_{50\%}$, and 90% of the particles are smaller than $d_{90\%}$. The discrepancy between these parameters thus relates of the width of the particle size distribution and the uniformity of the particle size. The capacity of the different graphites is as specified by the manufacturers. Notably, CPreme P5 has relatively low capacity compared to the other graphites. CPreme P5 is designed for use in power cells and exhibits the smallest particle size of the three graphite materials. This leads to increased rate capability and possibly improved low temperature performance, but probably at the sacrifice of specific capacity.

Table 2: Technical data of materials for graphite electrode manufacture [54, 64, 65]

Material	Name	Purity (%)	Manufacturer
Timcal graphites	SLP30	-	Timcal
CPreme graphites	P5, G8	-	CPreme
Carbon black	Super P Li	-	Timcal
PVDF binder	Kynar 761	100	Arkema
Copper foil	BF-Plainstainproof	>99.8	Circuit Foil
NMP	1-methyl-2-pyrrolidinone	99.5	Sigma-Aldrich

3.2.2 Electrolyte preparation

Five different electrolyte compositions were prepared and analysed in this work. The electrolyte preparation was done by others that have been acknowledged. The five compositions are shown in Table 3. The electrolytes were prepared by mixing the organic solvents and the lithium salt under argon atmosphere. The exact procedure for preparing electrolyte solution is described in appendix C.2.

Table 3: Electrolyte compositions

Electrolyte number	Electrolyte composition
E1	1:1 EC:DEC + 1 wt% VC + 1M $LiPF_6$
E2	1:1:3 EC:PC:EMC + 1M $LiPF_6$
E3	2:2:3:3 EC:PC:EMC:DMC + 1M $LiPF_6$
E4	1:2:2 EC:EMC:DMC + 1M $LiPF_6$
E5	1:1:3 EC:EA:EMC + 1M $LiPF_6$

Note that the ratios are weight-based. EA is abbreviation for ethyl acetate. Below is a table showing the manufacturer, the purity and the melting points of the various components used to prepare electrolytes.

Table 4: Technical information of electrolyte components [54, 57, 66]

Electrolyte component	Purity (%)	Water content (ppm)	Melting point (°C)	Manufacturer
EC	99	≤50	36	Sigma-Aldrich
DEC	≥99	≤50	-74	Sigma-Aldrich
VC	97	-	19-22	Sigma-Aldrich
PC	99.7	≤20	-49	Sigma-Aldrich
EMC	≥99	≤20	-53	Merck
DMC	≥99	≤50	5	Sigma-Aldrich
EA	99.8	≤50	-84	Sigma-Aldrich
$LiPF_6$	≥99.99	-	200	Sigma-Aldrich

3.2.3 Cell assembly

The cells were assembled in an argon-filled MBraun glove box with water and oxygen contents below 1 ppm. Graphite electrodes of diameter 16 mm were cut from the electrode sheets, weighed, and placed in the bottom case of 2016 Hohsen coin cells. A 16 mm ion-conductive polymer film (Celgard 2320) of 20 µm thickness was placed between the graphite electrode and the 14 mm diameter counter electrode cut from 0.75 mm thick lithium foil (Alfa Aesar, 99.9%). 30-45 µl electrolyte was applied to

sufficiently soak the graphite electrode and the separator, i.e. applied to both sides of the separator. A 16 mm diameter stainless steel (SUS316L alloy) spacer of 0.3 mm thickness was placed on top of the lithium electrode and finally the battery cap. The cells were hermetically sealed in an automatic crimping machine provided by Hohsen Corp. A photograph of the cell components is provided in Figure 21.

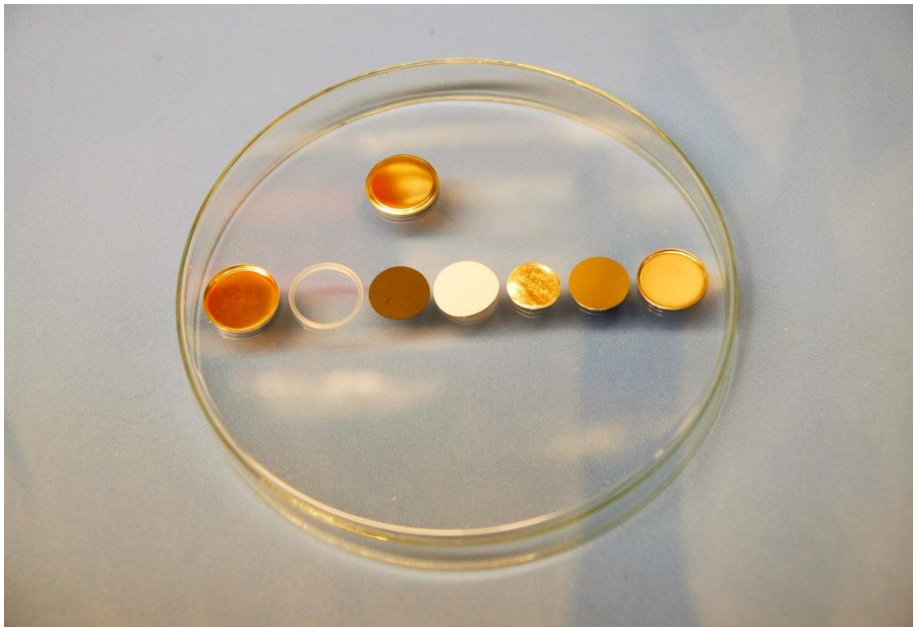

Figure 21: Cell components in the order of assembly. From left to right: Battery case, plastic gasket, graphite electrode, polymer separator, lithium electrode, metal spacer, and battery cap. An assembled coin cell can be seen above.

Matrix of cell combinations

The specific combinations of cells manufactured, cycled and thermally characterised in this work, in addition to the cycling method used, are given in Table 5. The figures inside the boxes indicate the electrolytes, according to Table 3, that were used to assemble cell combinations for the different cycling methods. The cell combinations were selected in order to compare the performance of the different graphite materials and the different electrolytes, both when cycled at room temperature and when cycled at lower and higher temperatures. Notably, cells containing CPreme P5 were also cycled using the temperature program in order to compare the low temperature performance of CPreme P5 and Timcal SLP30. Based on the results from cycling at different temperatures of Timcal SLP30, the electrolytes E2 and E4 were chosen for temperature cycling with CPreme P5.

Table 5: Cell combinations matrix

	Method of cycling	
Graphite material	Room temperature	Temperature program
Timcal SLP30	E1	E1, E2, E3, E4, E5
CPreme G8	E1	-
CPreme P5	E1	E2, E4

3.3 Electrochemical cycling

A computer controlled multichannel battery tester Maccor Model 4200 with a temperature chamber was used for electrochemical cycling. Varying discharge and charge rates (C-rates) were employed for the cycling programs. A current density of 1C is defined as the current required to completely charge or discharge an ideal cell with theoretical capacity (372 mAh/g) in one hour. Accordingly, C/2 corresponds to a current density that would discharge a completely charged cell in two hours, i.e. 186 mA/g. In this work, the first cycle was run at a slower C-rate to ensure optimal SEI formation conditions. Then, for the following cycles, a higher C-rate was employed to examine the rate capability of the cells.

Room temperature (RT) cycling program:

1. Initial galvanostatic discharge at 10 mA/g (C/37) until 5 mV.
2. Potential held at 5 mV until current dropped to 5 mA/g.
3. Galvanostatic charge at 10 mA/g until 1.5 V.
4. Ten cycles between 1.5 V and 5 mV at a rate of C/4.
5. Final discharge to obtain fully lithiated graphite at a rate of C/37 until 5 mV.

Cycling procedure with temperature program:

1. Initial galvanostatic discharge at 10 mA/g (C/37) until 5 mV at 20°C.
2. Potential held at 5 mV until current dropped to 5 mA/g at 20°C.
3. Galvanostatic charge at 10 mA/g until 1.5 V at 20°C.
4. Two cycles between 1.5 V and 5 mV using a rate of C/8 at 20°C.
5. Two cycles between 1.5 V and 5 mV using a rate of C/8 for each of the following temperatures, in order: 20°C, 10°C, 20°C, 0°C, 20°C, 40°C, 20°C. Upon temperature change in the chamber, the cell temperature was stabilised for at least two hours before the cycling commenced. The last step left the graphite completely de-lithiated (0% state of charge).

The cells were stored for varying periods between end of cycling and thermal analysis. They were discharged at a rate of C/37 until 5 mV right before thermal analysis in order to ensure that the graphite was fully lithiated.

3.4 Thermal characterisation

Two types of DSC analyses were conducted as part of the thermal characterisation in this work; low temperature analysis of pure electrolytes and high temperature analysis of graphite electrodes soaked with electrolyte, and of pure electrolytes. The low temperature DSC analysis would provide data on melting points and phase transitions in the electrolytes. Thus, the data could be useful to explain the performance of cells cycled at low temperatures. The high temperature analysis was performed in order to reveal the thermal stability of the various cell combinations and the effect of different cycling programs, enabling direct comparison of the influence of the various parameters.

3.4.1 DSC sample preparation

All samples for DSC analysis were prepared inside an argon-filled glove box to prevent the SEI layer and the electrolyte from chemically decomposing. For the high temperature analysis, the cycled cells were disassembled and samples of diameter 5 mm and typical weight of about 1-2 mg, including the Cu foil, were punched out from the fully lithiated graphite electrodes. These were weighed and placed inside high pressure stainless steel capsules with effective volume of 30 µl. 3 µl (about 3.5 mg by weight) fresh electrolyte, similar to the one used in the cell, was also added to the capsules and then they were hermetically sealed with a sealing tool. In order to determine the homogeneity of the electrode and the reproducibility of the analyses, two samples were cut and analysed from each electrode. At least two cells of each combination were disassembled to prepare samples, i.e. at least four samples of each cell combination were thermally analysed. The electrolyte samples for high temperature analysis were prepared by adding 3 µl solution to a high pressure sample capsule and hermetically sealing it. Two electrolyte samples were prepared of each electrolyte to ensure the reproducibility of the results.

Samples for the low temperature DSC analysis were prepared by adding 5 µl (about 6 mg by weight) electrolyte to aluminium sample pans which were hermetically sealed. At least two electrolyte samples were prepared of each electrolyte to ensure the reproducibility of the results. The sealing tool for the aluminium sample pans along with an enclosed pan is shown in Figure 22.

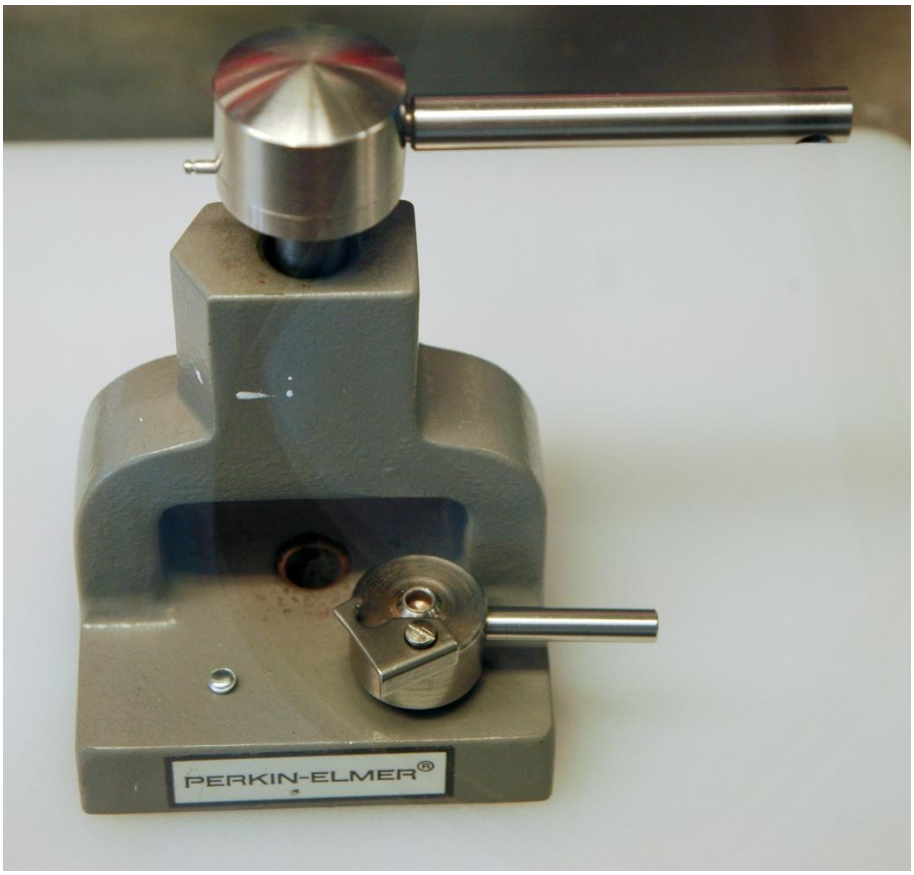

Figure 22: Sealing tool for the aluminium sample pans for the low temperature DSC analysis. A sealed pan is placed on the tool platform to the left of the pan holder.

The high pressure sample capsules were specified to withstand an internal pressure of 150 atmospheres. A photograph of the punching tool used to cut samples from the graphite electrodes, the sealing tool for high pressure sample capsules, and such a capsule is provided in Figure 23.

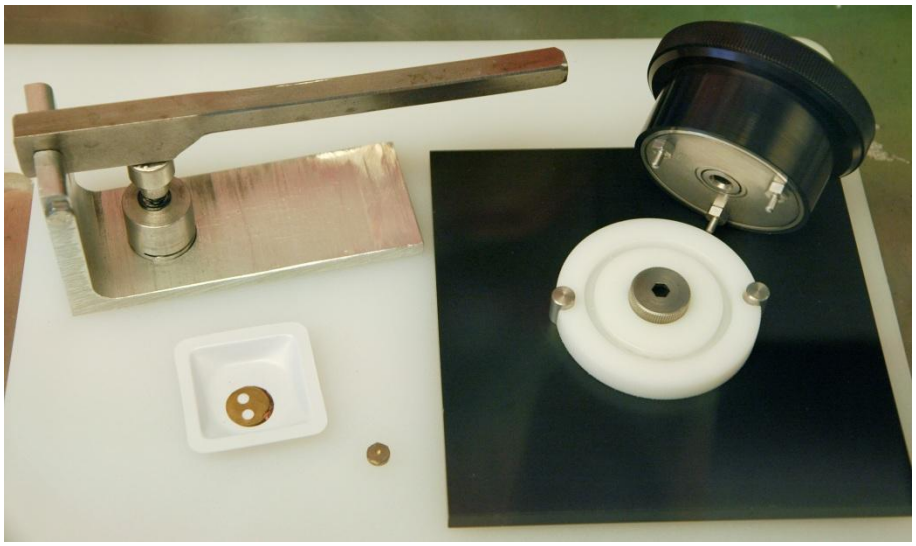

Figure 23: The tool for punching samples from graphite electrodes is to the left, above an electrode with two samples taken from it. Note that lithiated graphite is gold-coloured. The high pressure sample capsule sealing tool is to the right and a sealed capsule is placed in the middle.

3.4.2 DSC analysis

Two differential scanning calorimeters were utilised to conduct the thermal analyses. A TA Instruments DSC Q100 was used for the low temperature analyses while a PerkinElmer DSC 7 was used for the high temperature analyses. The DSC analyses were conducted using an empty sample capsule or pan as reference. The DSC capsules and pans were weighed before and after the analyses to ensure that no leakage developed during the experiments. The high temperature analyses were carried out over a temperature range from 30 to 300°C with a constant heating rate of 2.5°C/min. The low temperature analyses were carried out by first cooling the sample to -85°C, keeping it at that temperature for 20 minutes, and then heating it to 50°C with a constant rate of 5°C/min. This process was repeated once to investigate the reproducibility of the transitions. Both of the DSC instruments had attached cooling systems and the sample chambers were continuously flushed with nitrogen gas. The high temperature DSC curves presented in chapter 4.3.2 were obtained by subtracting a background scan (with empty sample capsules) from the sample analysis curve. Two photographs showing the sample chambers in the respective DSC instruments utilised in this work are displayed in Figure 24 and Figure 25.

Figure 24: Close-up of sample chamber in the TA Instruments DSC Q100 used for low temperature thermal analysis. The reference pan (top) and sample pan were placed on two separate platforms.

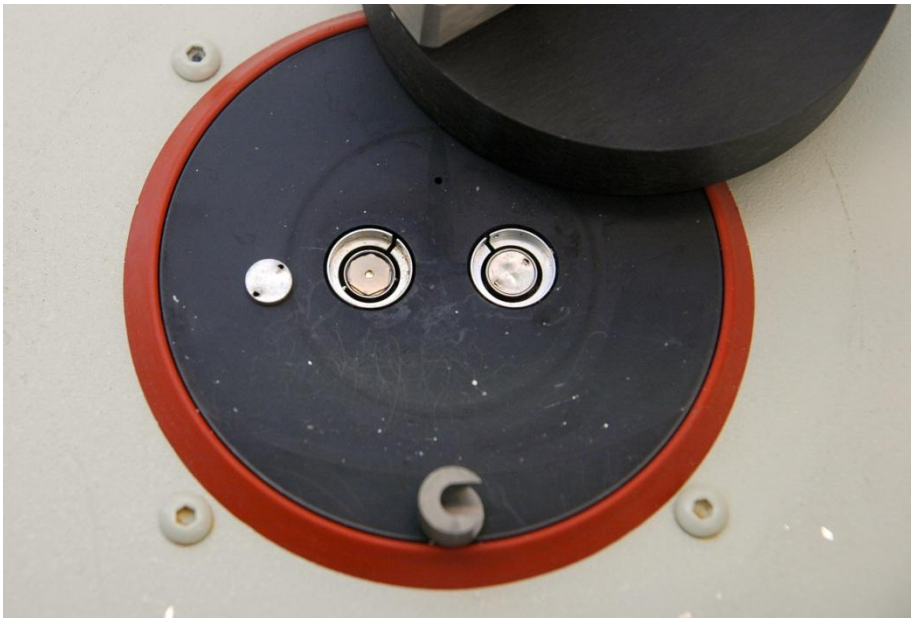

Figure 25: Close-up of sample chamber in the PerkinElmer DSC 7 used for high temperature thermal analysis, exhibiting the crucibles of the sample (left) and the reference (right).

3.5 Surface structure characterisation

Scanning electron micrographs were obtained from uncycled graphite electrodes. The electrodes were mounted on aluminium stubs and transferred into the SEM sample chamber. The characterisation was conducted in order to discover any differences in the morphology and particle size of the studied graphite materials. The

micrographs presented in this report were taken using secondary electron emission, an acceleration voltage of 10 kV and a working distance of about 11 mm on a Hitachi SU-6600 field emission scanning electron microscope.

3.6 Nitrogen adsorption measurements

Nitrogen adsorption measurements were performed to calculate the BET specific surface area; to estimate the relative and absolute extents of the basal plane, edge plane and defect surface areas; and to estimate the pore size distribution of the graphite powders. The BET values have already been presented in Table 1, but cannot be directly compared as the values come from different sources. Conducting these measurements on the same instrument using similar parameters enables direct comparison.

Before measurement, the powder samples were degassed overnight at 200°C until a static vacuum of less than 0.1 mbar was established. The measurements were conducted at liquid nitrogen temperature (-195.8°C) using a TriStar II 3020 (surface area and porosity analyser) apparatus by Micromeritics Instrument Corporation. The standard instrument software (version 1.03) and DFT Plus software was employed to calculate the adsorptive potential distributions from the adsorption isotherms. In other words, the software utilised density functional theory (DFT) on the data supplied by the BET measurements to calculate the extents of the various surface types and pore size distribution. The model for this calculation was developed by Ross and Olivier [67, 68] and employs the fact that nitrogen adsorbs with different energies to different surface types. Thus, by evaluating the contribution to the surface area at different adsorption energies/potentials, the relative ratio of the various surface types can be obtained. A schematic model displaying nitrogen adsorption on basal plane surfaces, edge plane surfaces and defect surfaces is provided in Figure 26.

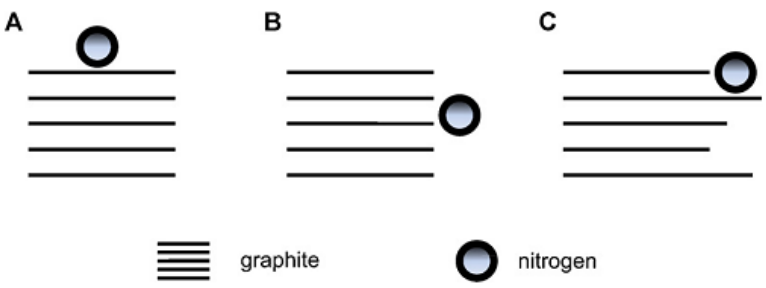

Figure 26: Illustration of nitrogen adsorption on basal plane surfaces (A), edge plane surfaces (B) and defect surfaces (C) [36].

4 Results

In this chapter, results from the surface structure characterisation, surface area measurements, thermal characterisation, and electrochemical cycling will be presented in order. First, micrographs of casted graphite materials and nitrogen adsorption measurements of graphite powders will be provided. DSC curves will be presented in the thermal analysis subchapter. In the final section about electrochemical cycling, voltage-charge curves and plots showing the discharge and charge capacities versus cycle number will be supplied to illustrate the electrochemical performance of the cells.

4.1 Surface structure of graphite materials

A)

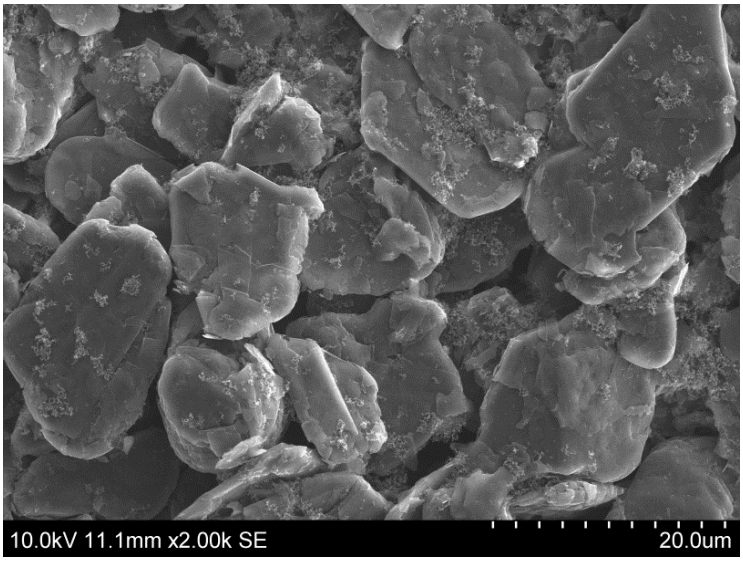

B)

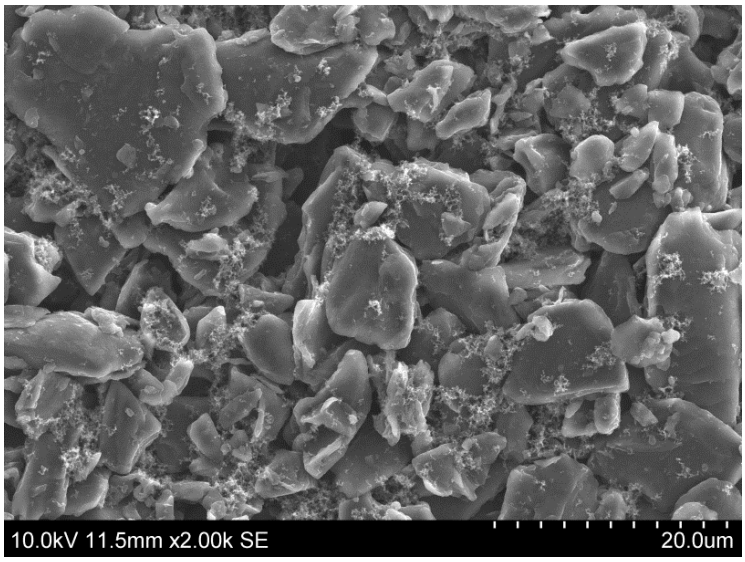

C)

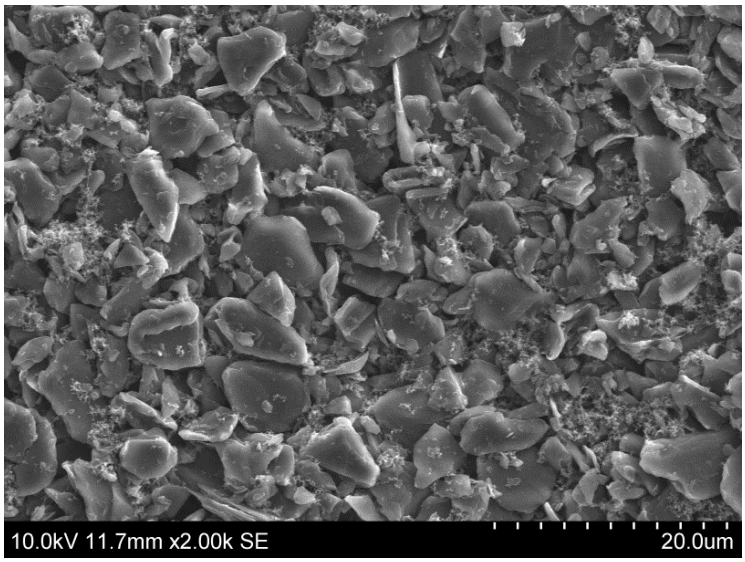

Figure 27: Micrographs of uncycled graphite electrodes. From top to bottom the micrographs show the surface structure of Timcal SLP30 (A), CPreme G8 (B) and CPreme P5 (C).

Most notably, the above micrographs clearly exhibit the different nominal particle sizes in the graphite materials. The nominal particle size is about 15 μm, 8 μm and 5 μm in Timcal SLP30, CPreme G8 and P5, respectively. All graphites are composed of particles with potato-shaped morphology. Furthermore, the particles are generally easily distinguishable because of the well-defined morphology. The particle surface is relatively smooth in all three graphites. The tiny particles sprinkled over the surface of and in between the larger graphite particles is carbon black, added to the casting mixture to increase the electrode conductivity.

4.2 Nitrogen adsorption measurements

This section will present the results from the nitrogen adsorption measurements. BET and DFT specific surface areas, the relative and absolute extents of the different surface types, and pore size data of the three studied graphites are provided in Table 6. Figure 28 shows the incremental surface area as a function of adsorptive potentials for the graphite materials.

Table 6: Graphite surface properties

Surface properties	Timcal SLP30	CPreme G8	CPreme P5
BET surface area (m^2/g)	6.16 ± 0.03	1.79 ± 0.03	3.48 ± 0.04
DFT surface area (m^2/g)	6.46	1.88	3.69
Edge plane surface area (m^2/g)	2.23	0.35	0.83
Basal plane surface area (m^2/g)	2.86	1.53	2.85
Defect surface area (m^2/g)	1.37	0	0
Ratio of basal:edge:defect areas (%)	44:34:21	81:19:0	77:23:0
Ratio of basal:non-basal areas (%)	44:56	81:19	71:29
Total area in pores (m^2/g)	2.41	0.6	1.2
% of surface area in pores (%)	37	33	33

All the properties presented below the row of "DFT surface area" are calculated based on the DFT surface area values.

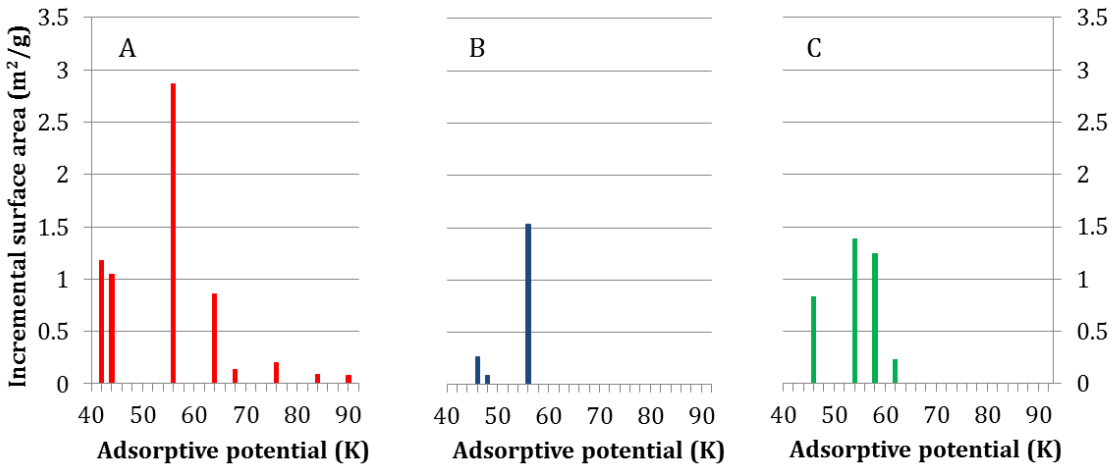

Figure 28: Incremental surface area vs. adsorptive potential plots of Timcal SLP30 (A), CPreme G8 (B), and CPreme P5 (C).

The absolute and relative extents of the basal plane, edge plane and defect surface areas presented in Table 6 were estimated based on the nitrogen adsorption

measurements. The strength with which nitrogen is adsorbed to a surface, termed the adsorptive potential with unit Kelvin, varies for different types of surfaces. This is the case also for graphite surfaces. Generally, the magnitude of the adsorptive potential increases with the local density of the adsorbent atoms [36]. According to literature [68, 69], the adsorptive potential distribution centred between 50 and 60 K represents the basal plane surfaces. The edge plane has a lower areal density of carbons, and will therefore adsorb nitrogen with lower adsorptive potential, i.e. <40 K. Defect surfaces, such as dislocations and surface steps result in increased surface roughness which also brings about enhanced interactions between the adsorbent and adsorbate atoms. According to Placke et al. [36], the adsorptive potential distribution above 62 K represents the defect surfaces. The absolute and relative extents of the different surface areas supplied in Table 6 were calculated by integration under the relevant increments in Figure 28.

The BET specific surface areas provided in Table 6 correlate quite well with the specified values from the manufacturers presented in Table 1. Timcal SLP30 has the highest specific surface area, while the values for both CPreme G8 and P5 are consistent with the specified values. Notably, the surface structure of the Timcal graphite is quite different than the CPreme materials. The surface of SLP30 is mostly made up of "non-basal plane" surface types, i.e. edge planes and defects, while basal planes is the prevalent surface type on both G8 and P5. Particularly, there are no measurable defects neither in P5 nor G8, while more than 20% of the surface in SLP30 is made up of defects.

Figure 29 displays the cumulative distribution of the surface area in different pore sizes for the three graphite materials. In the CPreme graphites, about 1/3 of the surface area is found in pores. The relative pore area is even higher for SLP30, 37%, corresponding to 2.41 m^2/g. The shapes of the distribution curves are similar and the curves clearly show for all three graphites that most of the pore area is inside pores with a smaller diameter than 16 nm. By taking both the total pore area values in Table 6 and Figure 29 into account, we can deduct that the CPreme materials nearly only contain pores smaller than 16 nm. The cumulative curves for these graphites also appear to be approaching the horizontal at 16 nm. For SLP30, on the other hand, the situation is different as the curve has reached 1.8 m^2/g at 16 nm pore width, while the total pore area is 2.41 m^2/g. Consequently, also larger pores must be present in SLP30. Importantly, no pores are smaller than 2 nm in any of the graphite materials, which is the critical size to allow access of $Li(EC)_{2/3}^+$ electrolyte complexes [70], thus activating the surface with respect to Li^+ intercalation.

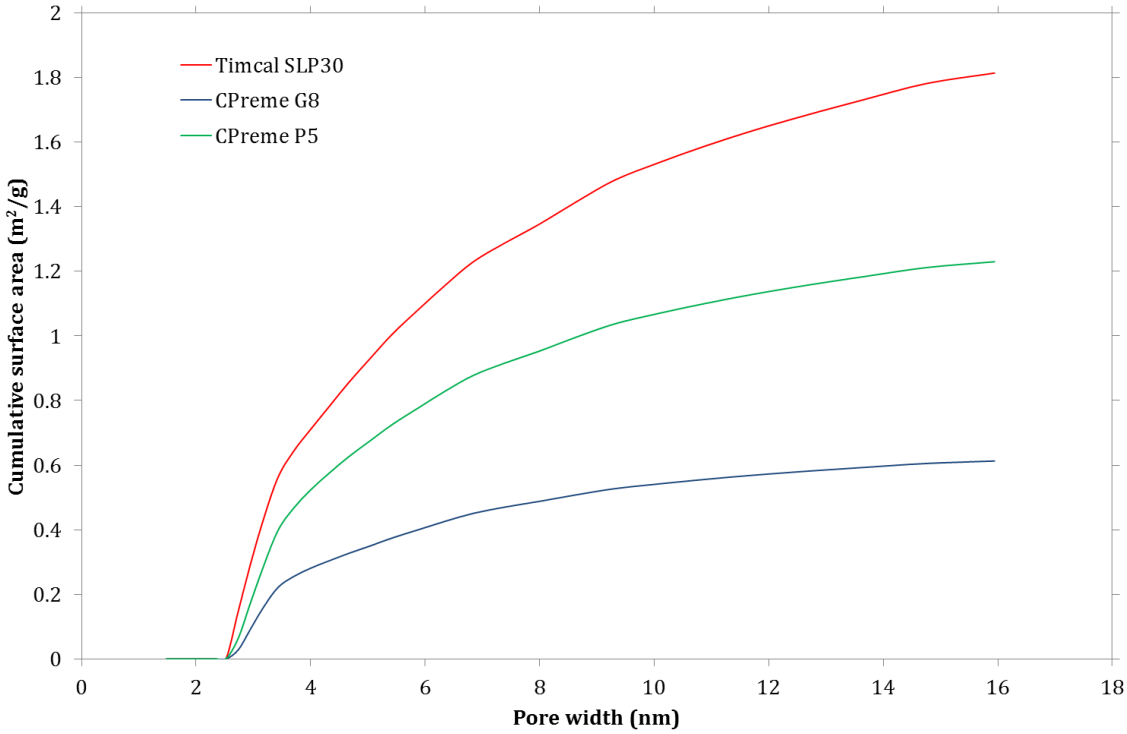

Figure 29: Cumulative surface area as a function of pore width for Timcal SLP30, CPreme G8 and P5.

4.3 Thermal analysis

This section comprises all the thermal analysis data obtained in this work, both at low temperatures of pure electrolytes, and at high temperatures of various combinations of cycled graphite materials and electrolytes. The data will be presented in similar order.

4.3.1 Low temperature DSC analysis

Figure 30 is an overview of the DSC curves obtained from low temperature analysis of the pure electrolytes. The electrolyte samples were heated twice from -80 to 50°C, but only one heating curve is shown for each electrolyte since both curves usually overlapped perfectly. In other words, the phase transitions observed in these curves were reproducible upon cooling and re-heating the sample. Note that endothermic reactions and processes are displayed as upward responses in the figure below.

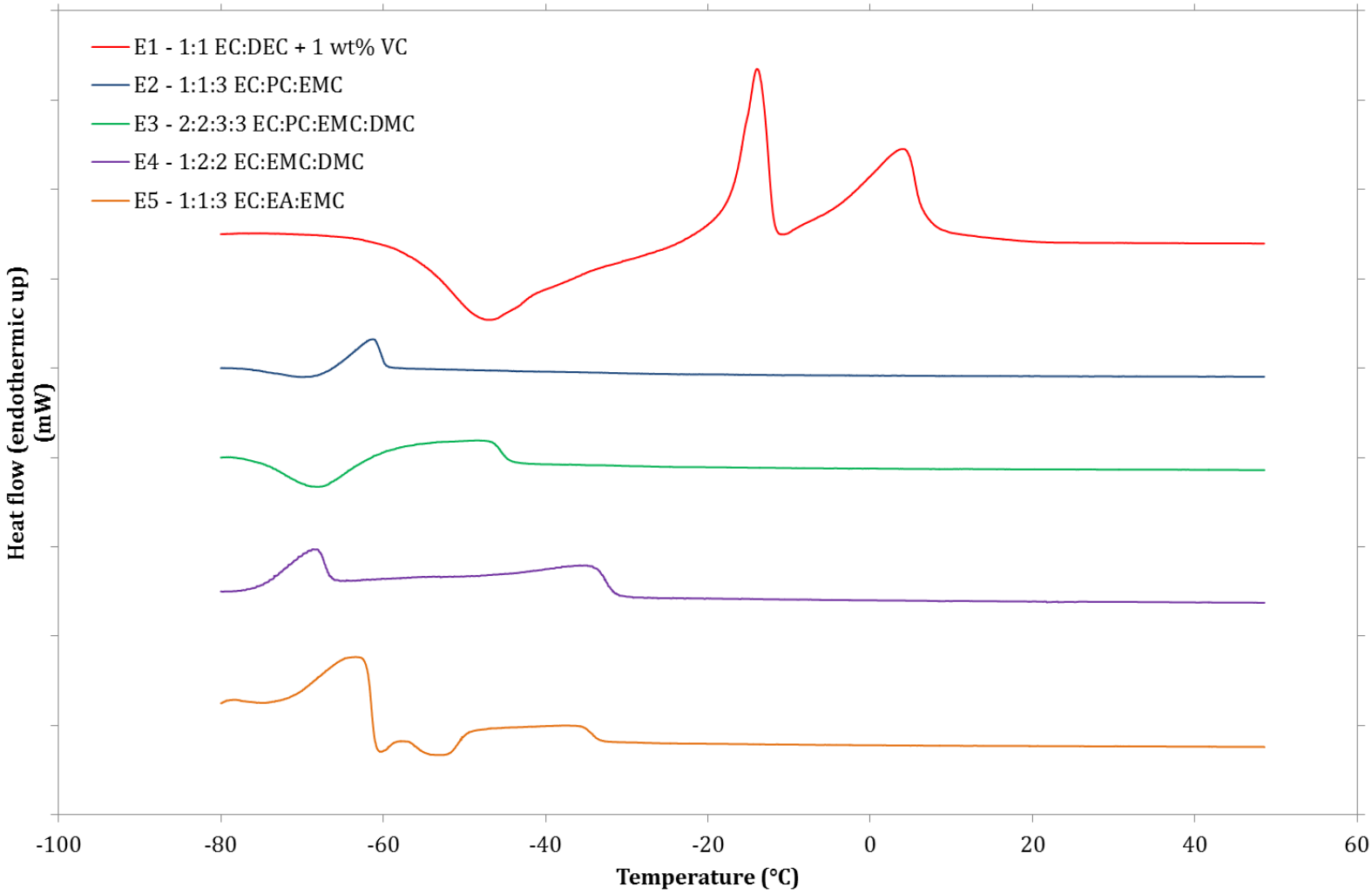

Figure 30: DSC heating curves showing the low temperature behaviour of the pure electrolytes.

In all the above curves, the endothermic peak/response observed at the highest temperature corresponds to the liquidus transition of the electrolyte solution. This is the temperature at which solidification of a component first takes place upon cooling, i.e. above this temperature the electrolyte is completely liquid. EC is common in all the electrolyte compositions and has the highest melting point of all the components, 36°C. Therefore, it is safe to assume that EC is the last component to melt upon heating of any of the electrolytes, thus causing the liquidus transition. Conservative estimates of the liquidus transition temperatures have been made based on the curves and are summarised in Table 7. The temperature can be translated to the liquid range of the electrolyte. Below the liquidus transition temperature, the electrolyte conductivity and performance is expected to worsen dramatically. Thus, the liquidus transition temperature effectively translates to the lowest operating temperature of the electrolyte.

Table 7: Liquidus transition temperature of the electrolytes

Electrolyte composition	Liquidus transition temperature (°C)
E1 - 1:1 EC:DEC + 1 wt% VC + 1M $LiPF_6$	5
E2 - 1:1:3 EC:PC:EMC + 1M $LiPF_6$	-60
E3 - 2:2:3:3 EC:PC:EMC:DMC + 1M $LiPF_6$	-45
E4 - 1:2:2 EC:EMC:DMC + 1M $LiPF_6$	-30
E5 - 1:1:3 EC:EA:EMC + 1M $LiPF_6$	-35

In addition to the liquidus transition peak, there are also other endothermic peaks present in the DSC curves. These are also caused by phase transitions from solid to liquid, i.e. melting of components. The E1, E4, and E5 electrolytes exhibit two or three endothermic peaks upon heating, while the E2 and E3 electrolytes display only one peak. If the electrolyte composition is close to the eutectic composition, the melting peaks will appear over a narrow temperature range. The lone peak in the E2 and E3 electrolyte curves could be composed of such overlapping peaks.

Even though only the heating curves are provided in Figure 30, the DSC responses on cooling of the electrolyte samples were also acquired. However, only the E4 electrolyte showed any thermal response on cooling, which is why these data are not presented. A considerable exothermic peak in the E4 cooling curve between -52°C and -62°C probably stemmed from the complete freezing of the electrolyte. This indicates that the E4 electrolyte was in fact the only electrolyte which completely froze before -85°C.

Some of the heating curves, e.g. of the E1 and E3 electrolytes, feature a broad exothermic response at a very low temperature, between -70 and -40°C. The possible reasons for this peak, as well as a thorough discussion of the other peaks and features present will be presented in chapter 5.2.1.

4.3.2 High temperature DSC analysis

This section will present the thermal results obtained from the high temperature DSC analyses. At least four parallel analyses were conducted of each sample combination. Representative DSC curves are presented. Figure 31 shows DSC curves of pure electrolytes, Figure 32 of room temperature cycled graphite samples with the E1 electrolyte, Figure 33 of temperature cycled Timcal SLP30 graphite samples with all five electrolytes, Figure 34 of temperature cycled CPreme P5 samples with electrolytes E2 and E4, and Figure 35 of temperature cycled SLP30 and P5 with electrolytes E2 and E4. The figures will create a basis for direct comparison of the various parameters. Finally, Figure 36 shows DSC curves exhibiting the thermal variation among two samples taken from the same graphite electrode to illustrate the degree of heterogeneity in the material and the reproducibility of the analyses. Exothermic reactions are displayed as upward responses in the following figures. The detected heat flow from the DSC analyses of graphite was normalised with the graphite weight (unit W/g).

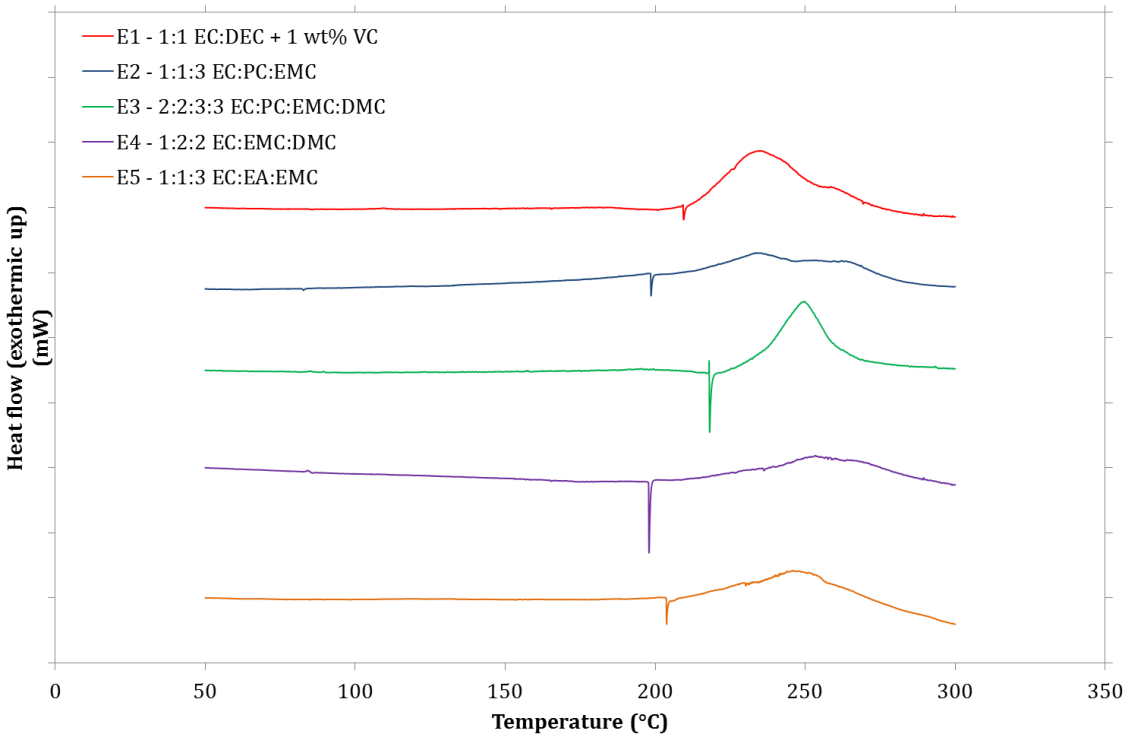

Figure 31: Comparison of the high temperature thermal behaviour of the five electrolytes.

The five electrolytes all have relatively similar thermal behaviour upon heating to 300°C. In general, there are no thermal reactions occurring below 200°C. Above that temperature, the electrolytes start decomposing, shown as an exothermic response which continues until the temperature is about 300°C. The magnitude of the response, however, varies substantially for the different electrolytes. Particularly electrolytes E1 and E3 appear to release more heat during the decomposition than the other electrolytes.

All curves feature a very sharp endothermic peak, apparently occurring right before the decomposition reaction. To the best of our knowledge, there is no reason why there should be such a sharp endothermic peak in the curves. This leads us to believe that it is merely an artefact caused by the instrument. These curves will be more thoroughly discussed in chapter 5.2.2.

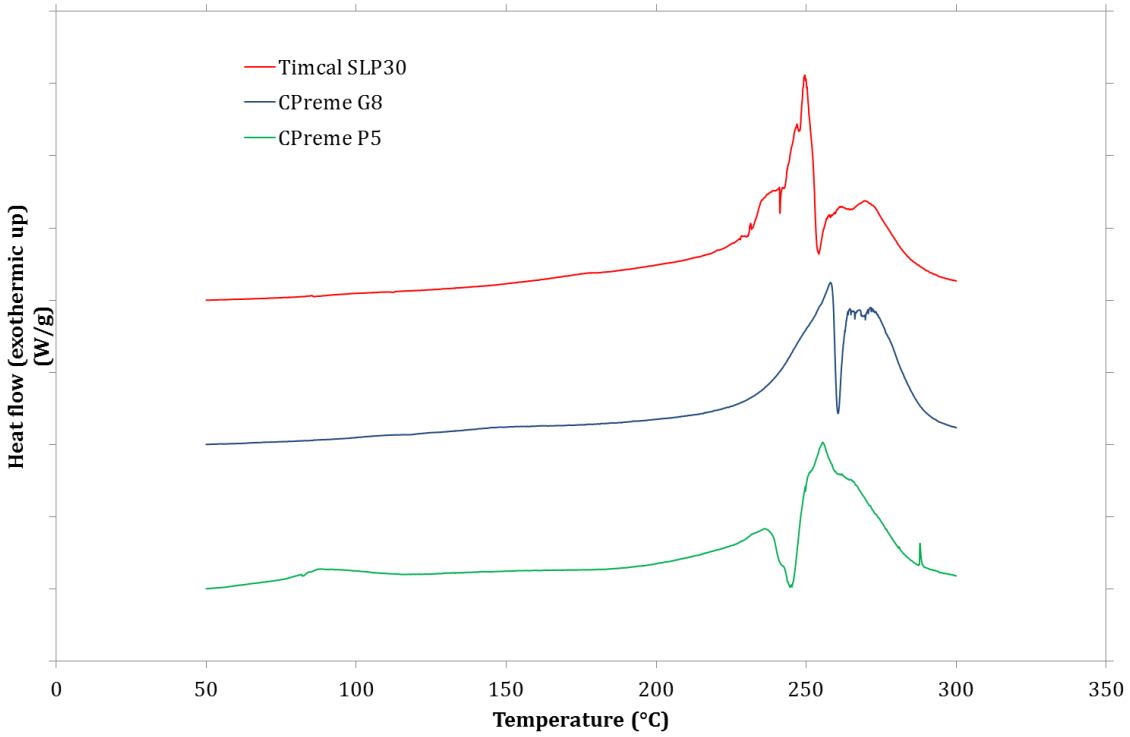

Figure 32: Comparison of the thermal behaviour of room temperature cycled graphite samples with electrolyte E1.

At first glance, the above DSC curves appear similar. Thermally speaking, there is not much happening between 50 and 200°C. According to the literature on the field, summarised in chapter 2.5.3, heat evolution due to SEI transformation and direct reaction between the lithiated graphite and electrolyte through the layer is expected to occur in this temperature interval. By careful inspection, a slight positive gradient

can be observed in the curves, indicating that there are in fact some thermal reactions occurring in the samples. Moreover, the CPreme P5 curve features a small exothermic peak at about 80°C, which might be due to transformation of the SEI layer.

From about 230°C, there is increased heat generation in the samples, which is caused by electrolyte decomposition (see Figure 31). The initial exothermic peak is succeeded by a well-known endothermic response caused by exfoliation of the graphite structure. As described in chapter 2.5.2, co-intercalation and subsequent decomposition of EC molecules in between the graphene planes is believed to increase the pressure and bring about the exfoliation. After the endothermic peak, there is yet another exothermic response. This response is probably a consequence of both the exfoliation, exposing fresh lithiated graphite that reacts with the electrolyte, and continued decomposition of electrolyte and PVDF.

Generally, there are no substantial differences between the above curves. Nevertheless, the onset temperature of some of the processes, for example the exfoliation, varies for the different graphite materials. These differences, and the general behaviour of the materials, will be further discussed in chapter 5.2.2.

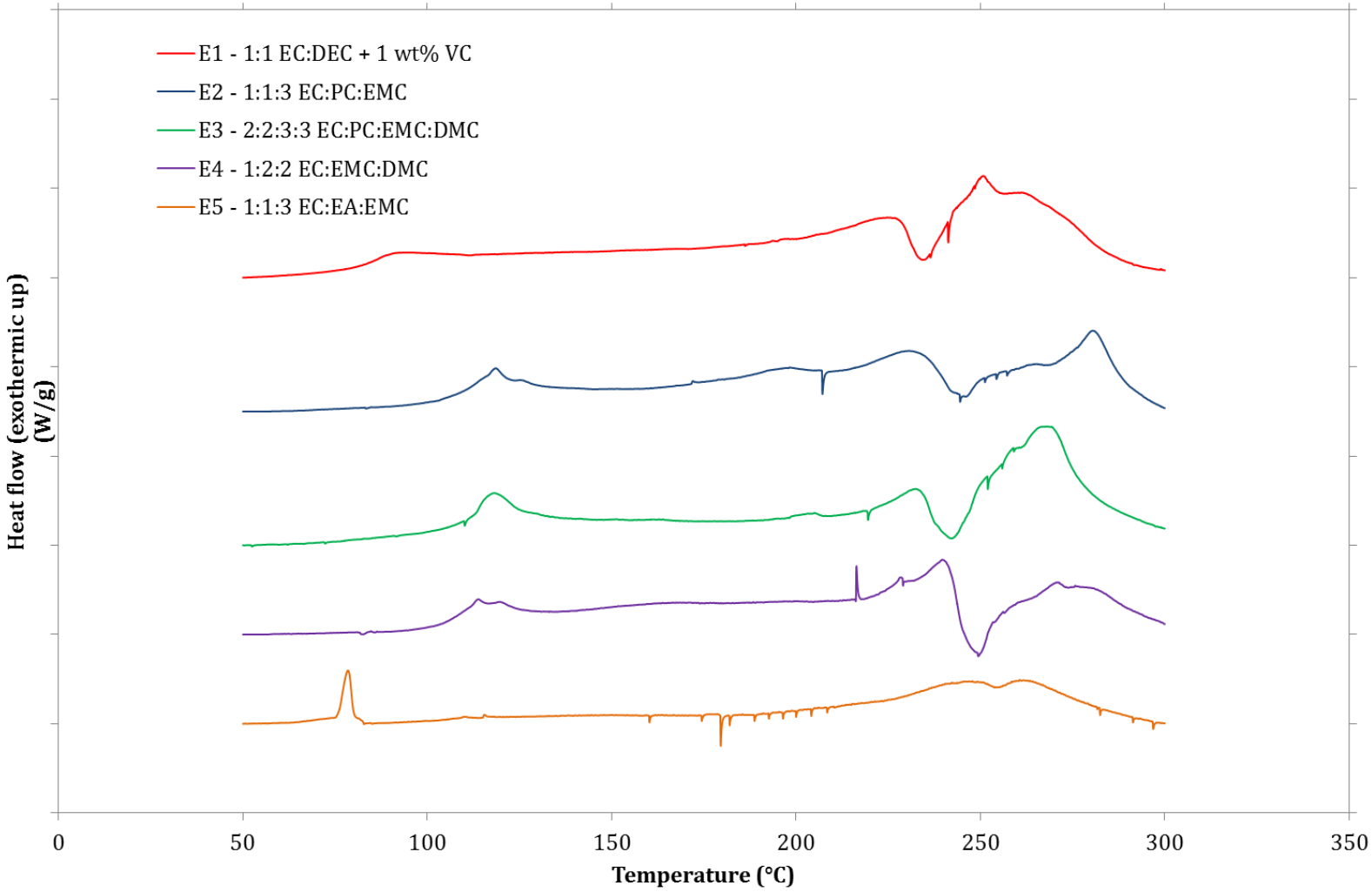

Figure 33: Comparison of the thermal behaviour of temperature cycled Timcal SLP30 electrode samples with the five electrolytes.

Most of the DSC curves in Figure 33 show the expected features from samples of cycled graphite and electrolyte. For the samples containing electrolyte E1-E4, the initial onset temperature varies between about 70 and 100°C, and is a result of SEI transformation. The magnitudes of the observed thermal responses are quite similar for the different electrolytes, but there are small variations.

The thermal behaviour of the sample containing E5 deviates in several ways from the other samples. Firstly, there is a sharp exothermic peak between 75 and 80°C, which does not resemble the typical heat response from SEI transformation which could occur in the same temperature interval. Furthermore, after this peak, there seems to be very little occurring in the sample, thermally speaking, until about 200°C. This deviating behaviour will be thoroughly discussed along with the rest of the DSC curves in chapter 5.2.2.

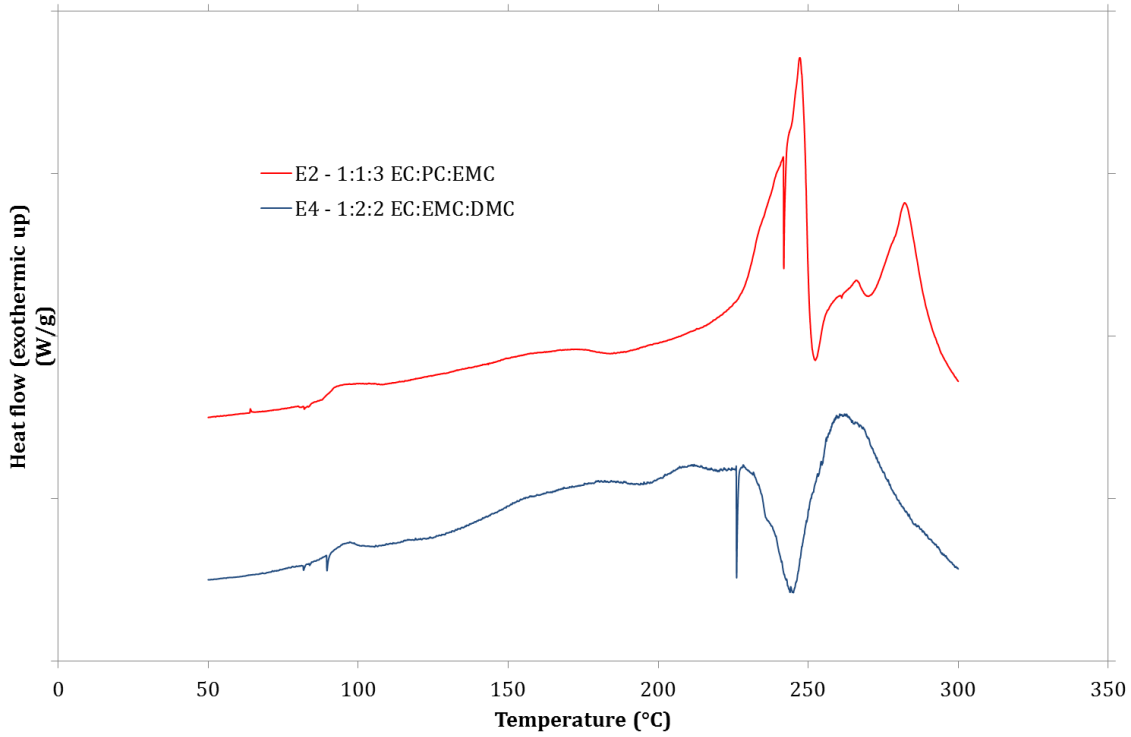

Figure 34: Comparison of the thermal behaviour of temperature cycled CPreme P5 electrode samples with electrolytes E2 and E4.

The same features as those observed for temperature cycled SLP30 are also present in the DSC curves of temperature cycled P5 with electrolytes E2 and E4. The onset temperature of SEI transformation is about 80°C for both samples. The heat generation between 100 and 200°C is significantly larger for the graphite cycled with electrolyte E4. In addition, the exfoliation process occurs at a lower temperature in

this sample. The heat evolution related to electrolyte decomposition, on the other hand, is larger for the sample with electrolyte E2. The thermal behaviour of these samples will be further inspected in chapter 5.2.2.

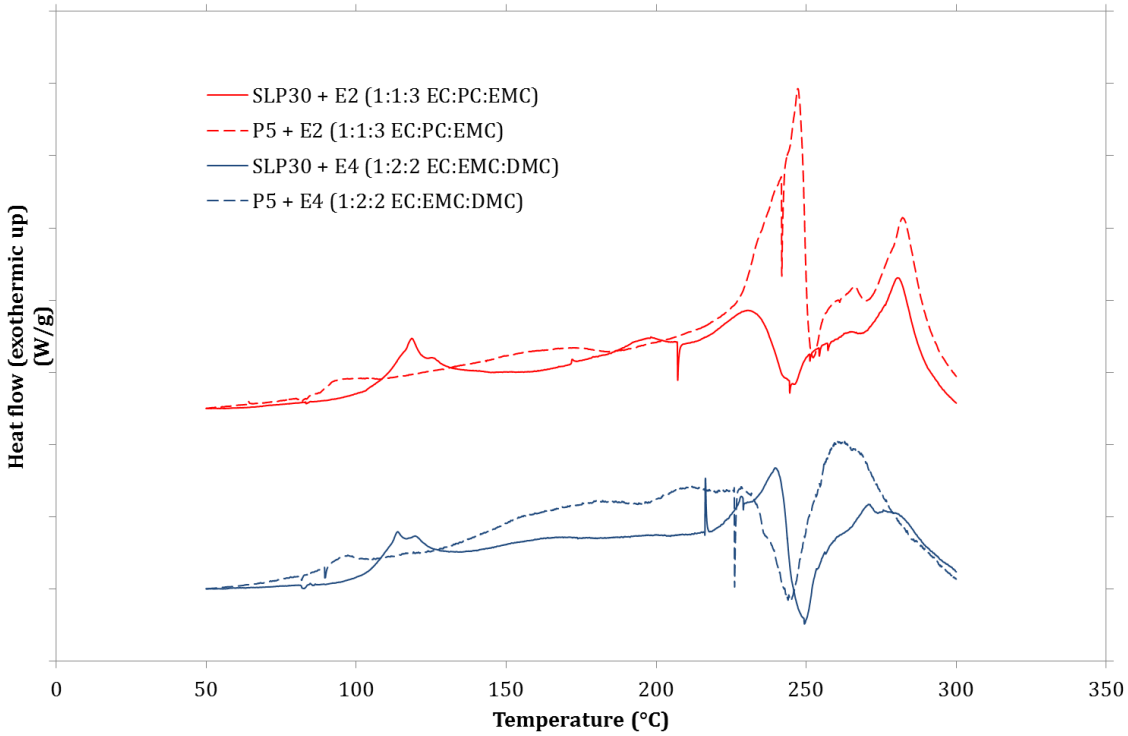

Figure 35: Comparison of the thermal behaviour of temperature cycled Timcal SLP30 and CPreme P5 electrode samples using electrolytes E2 and E4.

Figure 35 compares the thermal stability of Timcal SLP30 and CPreme P5 after cycling at different temperatures. Since CPreme P5 was temperature cycled only with electrolytes E2 and E4, the corresponding curves with Timcal SLP30 from Figure 33 are displayed. Interestingly, the onset temperature of SEI transformation seems to be lower for P5 than SLP30 regardless of electrolyte composition. In contrast, the corresponding peak height is higher for SLP30. As a consequence, the total heat evolution is fairly similar in both samples, at least when electrolyte E2 is used. Regarding the samples containing electrolyte E4, the heat production between 100 and 200°C is larger for P5 than SLP30. From the above figure, it is difficult to find any clear correlation between graphite type and onset temperature and magnitude of the exfoliation and electrolyte decomposition processes. The possible reasons for this and the general differences regarding thermal stability of temperature cycled SLP30 and P5 will be further examined in chapter 5.2.2.

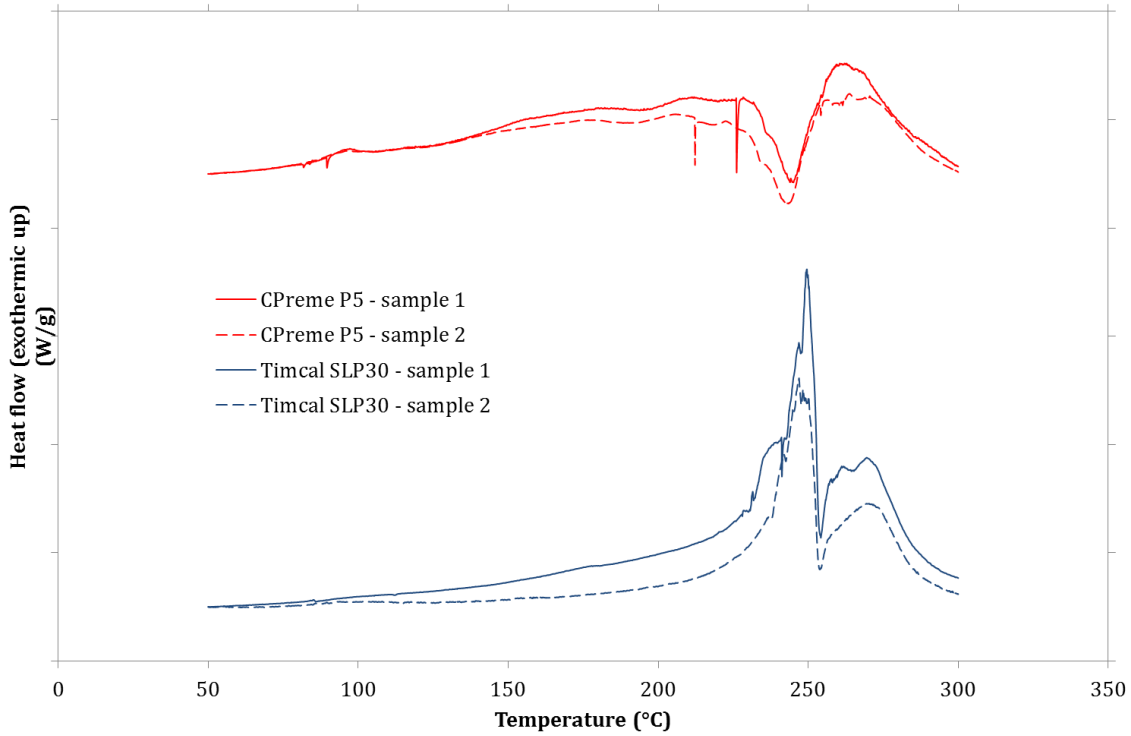

Figure 36: Examples of thermal variation among samples taken from the same graphite electrode. The CPreme P5 samples were temperature cycled with electrolyte E2 and the Timcal SLP30 samples were cycled at room temperature with electrolyte E1.

The above figure clearly shows that the cycled graphite electrodes are heterogeneous materials. The thermal variation can be quite significant, especially with respect to the electrolyte decomposition, the magnitude of which is very dependent on the amount of electrolyte in the sample. Obviously, the instrument uncertainty will also add to the total variation observed. At the same time, it is evident that the curves contain the same features at roughly the same temperatures. Consequently, the curves should allow for at least qualitative analyses of the thermal stability. Even though the variation is too large to permit quantitative comparison of the total heat output from different samples, the heat evolution from specific processes such as SEI transformation should be possible to compare quantitatively. Overall, the analyses have acceptable reproducibility.

4.4 Electrochemical cycling

This section comprises selected data from the electrochemical cycling of the different cell combinations, both those cycled at room temperature and those cycled with a temperature program. Not all the data will be presented, but enough to give a representative picture of the results and findings. The main purpose of the electrochemical cycling was to determine the properties and performance of the

various graphite materials and electrolytes at different temperatures. In addition, the SEI layer, which is the primary cause of the thermal instabilities in Li-ion batteries, is formed during cycling, enabling the subsequent thermal analysis.

Two or more parallels of each cell combination were assembled and cycled. The temperature cycled cells using Timcal SLP30 as graphite material were kindly assembled and prepared for cycling by PhD candidate Carl Erik Lie Foss.

4.4.1 Room temperature cycling

In the following figures, the large plot shows the correlation of voltage and capacity for all 11 cycles and the insert displays capacity versus cycle number. Figure 37-Figure 39 shows the cycling behaviour of Timcal SLP30, CPreme P5 and CPreme G8, respectively.

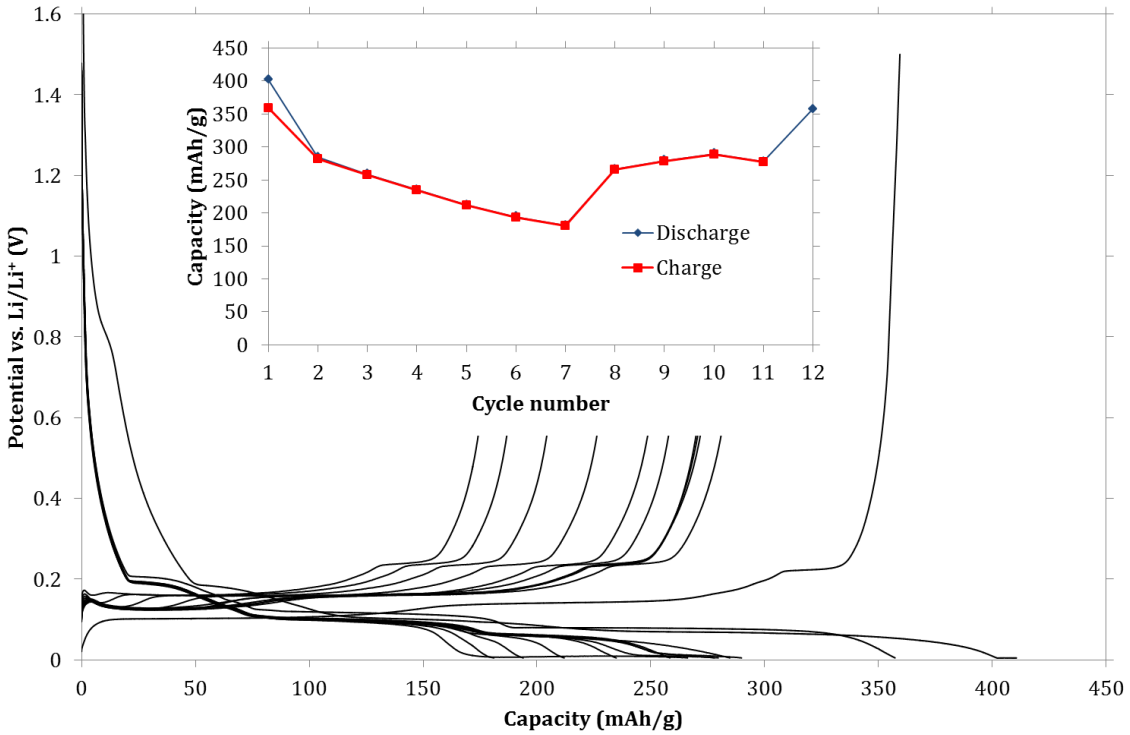

Figure 37: Cycling behaviour of cell composed of Timcal SLP30 as graphite material and the 1:1 EC:DEC + 1 wt% VC (E1) electrolyte. Note that the insert covers some of the voltage-charge curves above 0.6 V. The covered lines have similar trend as the uncovered line on the far right.

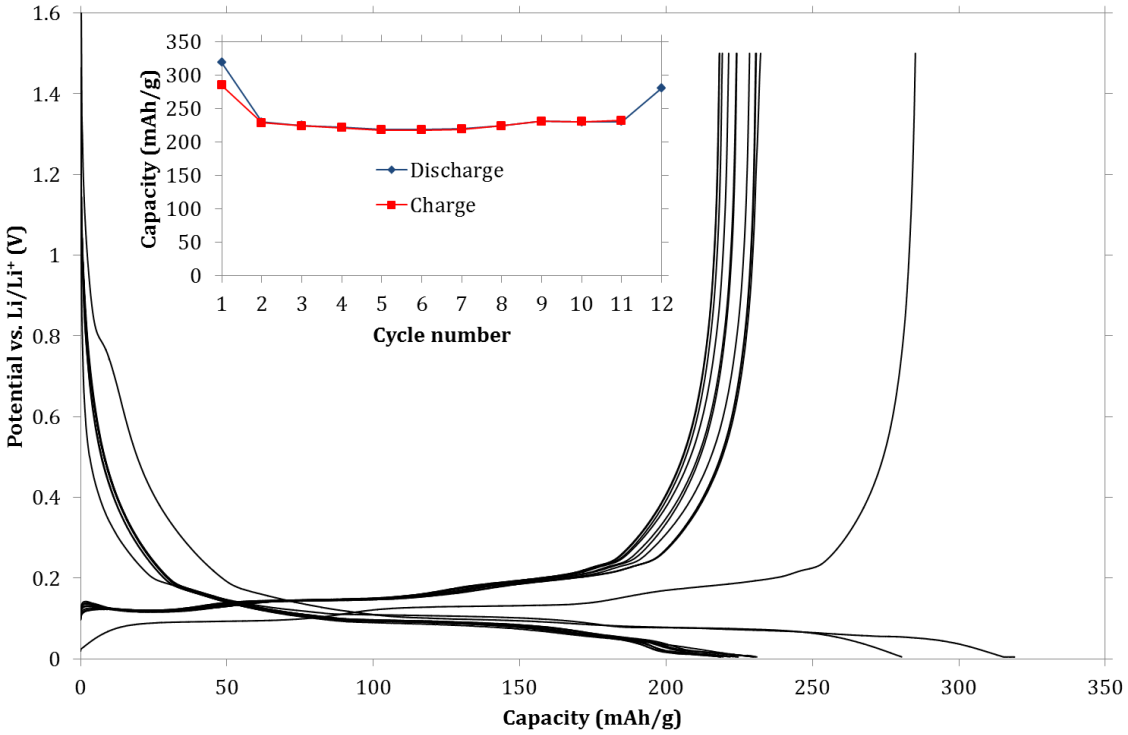

Figure 38: Cycling behaviour of cell composed of CPreme P5 as graphite material and the 1:1 EC:DEC + 1 wt% VC (E1) electrolyte.

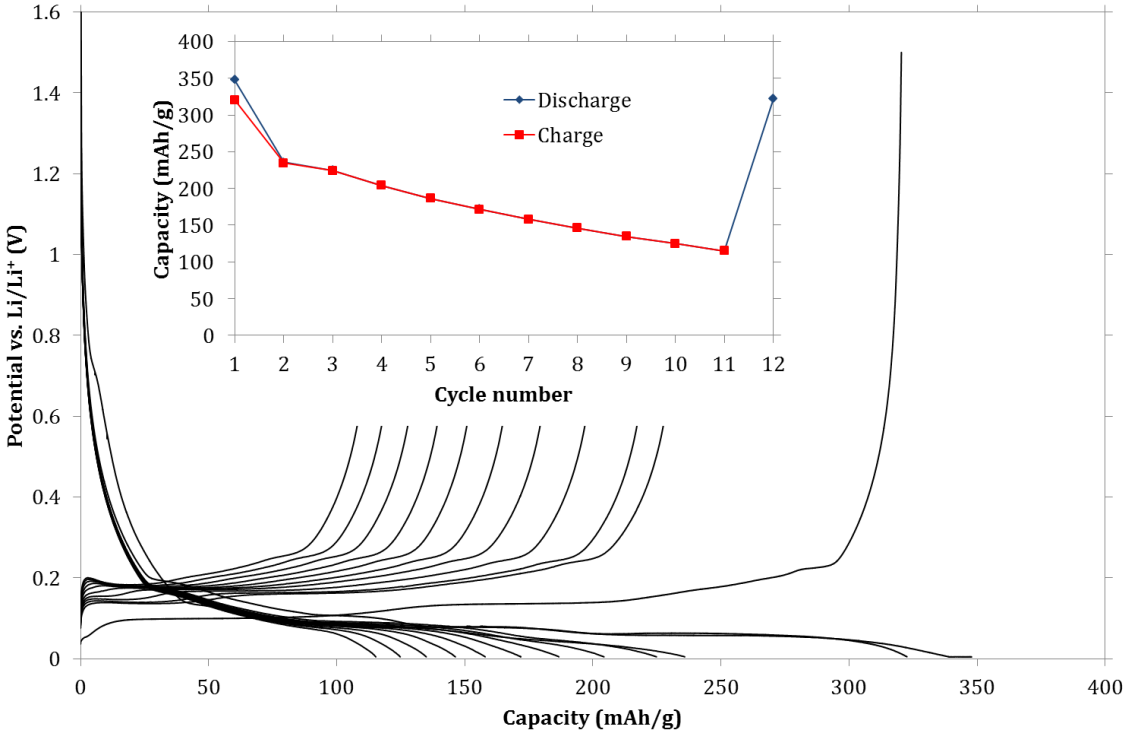

Figure 39: Cycling behaviour of cell composed of CPreme G8 as graphite material and the 1:1 EC:DEC + 1 wt% VC (E1) electrolyte. Again, note that the insert covers some of the voltage-charge curves above 0.6 V. The covered lines have similar trend as the uncovered line on the far right.

The irreversible capacity loss (ICL) during the initial cycle is a measure of the capacity lost due to SEI formation, which occurs mainly during the initial cycle. Thus, the ICL value for a Li/graphite half cell is often used to characterise the performance of the cell. High ICL values mean lower capacity and thus poorer cell performance. For the cells analysed in this work, the ICL is calculated as follows

$$\text{ICL} = \frac{Q_{discharge} - Q_{charge}}{Q_{discharge}} \times 100\% \qquad (4.1)$$

where $Q_{discharge}$ is the initial discharge capacity and Q_{charge} is the following charge capacity. Using equation (4.1), the average ICL values from cycling of Timcal SLP30, CPreme G8 and CPreme P5 cells were calculated and are summarised in Table 8 along with the respective average reversible capacities obtained in the cells. The standard deviation of the values is also provided. The discharge capacity at slow rate (C/37) in the 12th and final cycle was defined as the maximum reversible capacity attainable from a cell. The cell capacity is similar to the graphite electrode capacity as lithium metal has much higher capacity and acts as a Li^+ reservoir in these cells.

Table 8: Performance characteristics of RT cycled cells with E1 electrolyte

Graphite material	ICL (%)	Reversible capacity (mAh/g)
Timcal SLP30	12.9 ± 1.6	355 ± 5.9
CPreme G8	7.9 ± 0.1	316 ± 6.3
CPreme P5	11.0 ± 0.4	285 ± 4.5

Bearing in mind Table 1 with the graphite materials properties, it is apparent that the performance, at least at slow cycle rates, of the graphite materials manufactured in this work is not far behind the specified values. The reversible capacities of the cells are almost similar to the values provided by the manufacturers. Furthermore, it is clear that there is a positive relation between the specific surface areas provided in Table 6 and the ICL values of the graphites. Higher specific surface area brings about more extensive SEI formation, as SEI is formed on the entire graphite surface exposed to the electrolyte, and this ultimately results in larger irreversible capacity loss. The implications of the ratio of "non-basal" to basal plane surface area and other surface properties on the cell performance will be further discussed in chapter 5.3.1.

The cycling behaviour of Timcal SLP30 and CPreme G8, displayed in Figure 37 and Figure 39, respectively, is fairly similar. The capacity decreases slightly for each cycle

when the cells are cycled at a rate of C/4. However, for the final discharge at the very slow rate of C/37, the capacity is almost similar to the initial charge capacity. This means that the capacity degradation has not been irreversible, and thus probably not a result of extensive SEI formation. It is known that the SEI may use some time to stabilise, as its final structure is a result of a two stage process [22]. In the initial stage, a porous layer is created, mostly containing organic compounds, while the final stage results in a more compact layer with higher conductivity. With respect to Li^+ kinetics, the properties of the final SEI are thus improved compared to the half-finished layer. This could explain the remarkable cycling behaviour observed for Timcal SLP30 in Figure 37, where the cell capacity suddenly jumps almost 100 mAh/g between the 7^{th} and 8^{th} cycle. The capacity jump might also be explained by cell stabilisation, e.g. microstructural changes occurring in the graphite electrode during cycling, ultimately improving the Li^+ kinetics. Most of the Timcal SLP30 cells manufactured for this work had similar cycling behaviour as shown for CPreme G8 in Figure 39. Therefore, we cannot conclude that any of these graphites have higher cycling performance than the other.

The cycling behaviour of CPreme P5, shown in Figure 38, is different in several ways to the two other graphite materials. As expected, it delivers less capacity than SLP30 and G8. However, it retains a higher fraction of its reversible capacity when cycled at C/4. Furthermore, the capacity is not degraded for each cycle, but rather stays constant between 220-230 mAh/g for all 10 cycles at C/4. This improved cycling behaviour is probably not related to the high rate capability of P5 due to reduced particle size. Differences in the electrode thickness caused by minor variations in the casting process could have a much larger influence on the electrode rate capability in this case. This aspect, including all the other results from this subchapter, will be more carefully treated in chapter 5.3.1.

4.4.2 Cycling with temperature program

In this section, the cycling behaviour of the temperature cycled cells will be presented, according to the temperature cycling procedure described in chapter 3.3. Under each subchapter, the first figures are representative voltage-charge curves with inserts displaying capacity as a function of cycle number for the three first cycles at 20°C for each electrolyte composition. The next figure displays the capacity of the cells against temperature when cycled with the temperature program. Notably, two cycles were performed at each of the seven temperatures, in total 14 cycles, and thus there are 14 capacity points. Consequently, the figures also show the capacity as a function of time during the cycling program. As seen in Table 5, cells for cycling at

different temperatures were assembled using Timcal SLP30 as graphite material with five different electrolytes, and CPreme P5 with two different electrolytes. Four parallels were assembled and cycled of each combination. The error bars in the capacity versus temperature plots indicate the standard deviation of the capacity for the four cells.

4.4.2.1 Temperature cycling of Timcal SLP30 cells

Figure 40-Figure 44 show the cycling behaviour of the three initial cycles for cells composed of Timcal SLP30 and the five electrolytes. Figure 45 displays the capacity of the same cells when cycled at different temperatures.

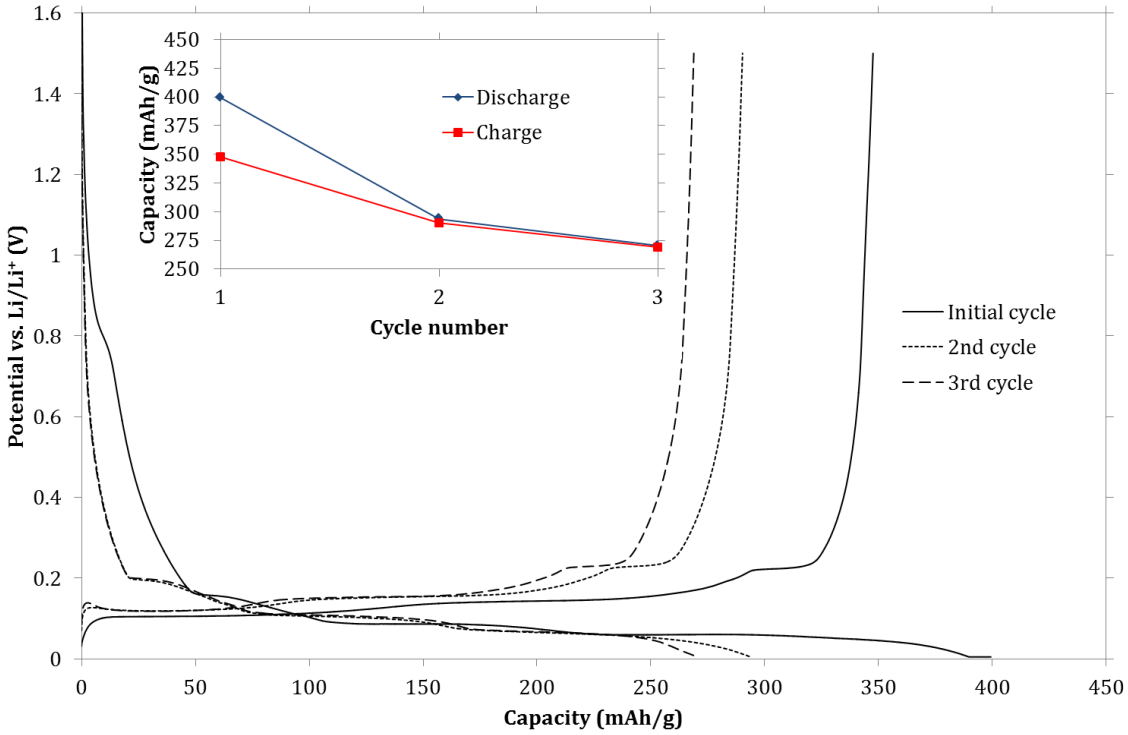

Figure 40: Cycling behaviour for the three first cycles at 20°C of one of the four cells composed of Timcal SLP30 and the 1:1 EC:DEC + 1 wt% VC (E1) electrolyte.

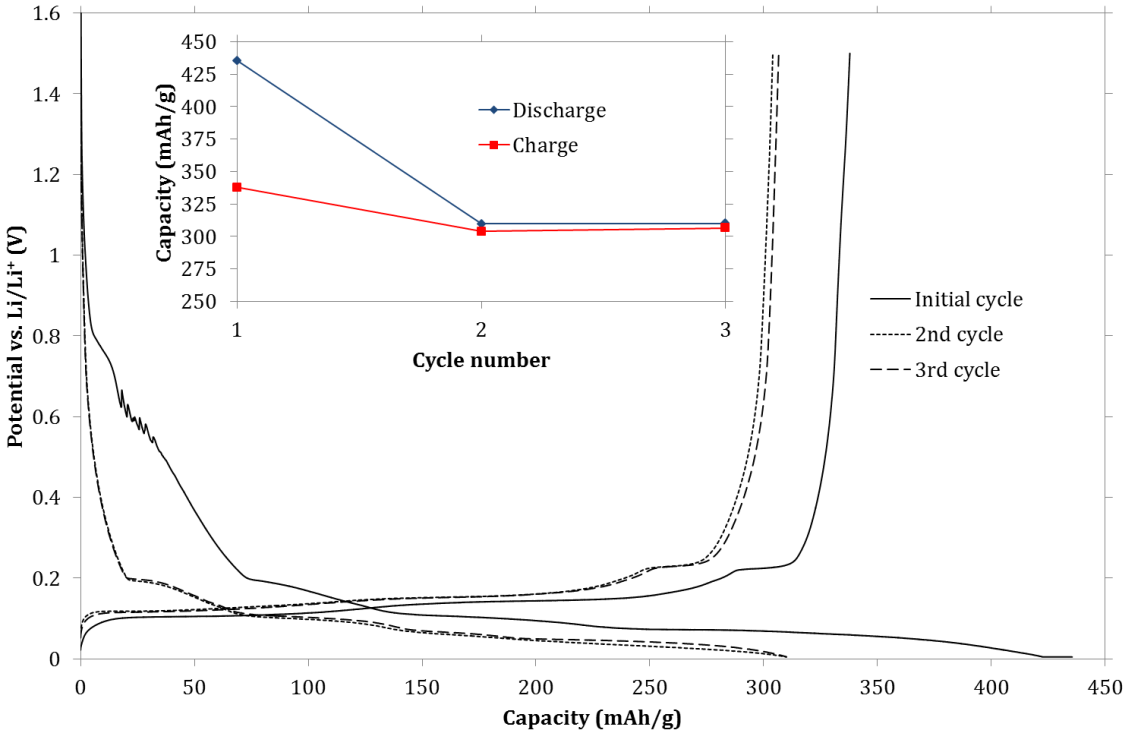

Figure 41: Cycling behaviour for the three first cycles at 20°C of one of the four cells composed of Timcal SLP30 and the 1:1:3 EC:PC:EMC (E2) electrolyte. The roughness of the initial discharge curve at about 0.6 V is likely noise caused by external effects.

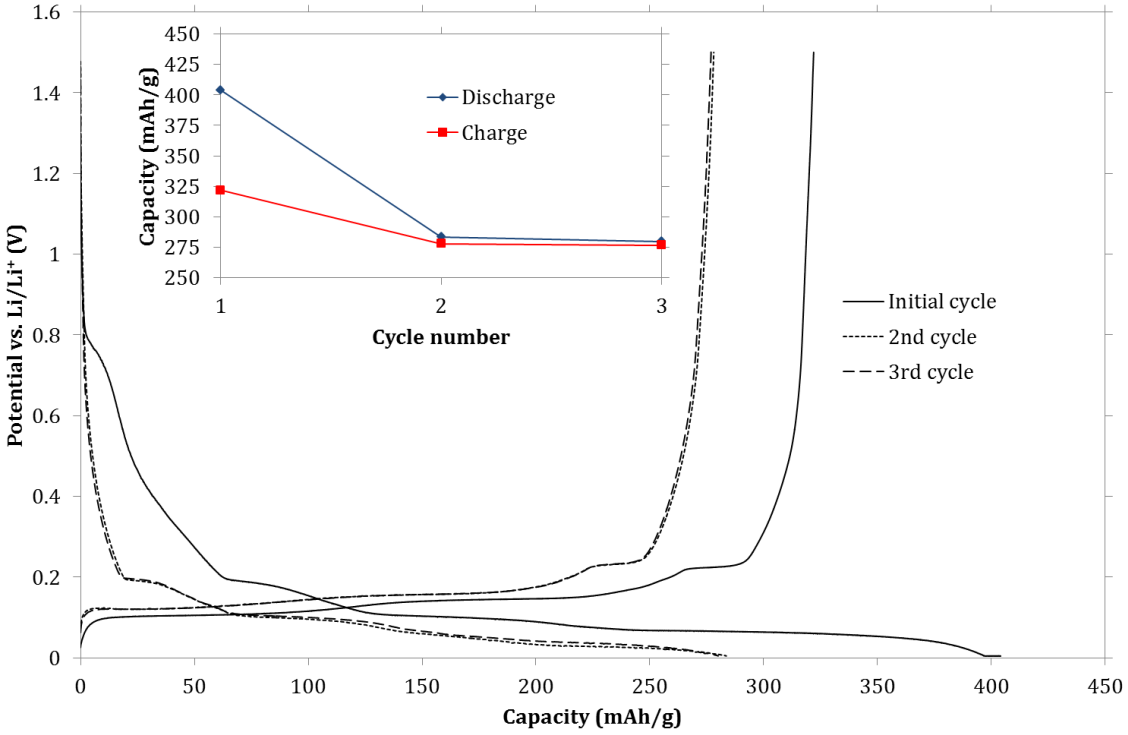

Figure 42: Cycling behaviour for the three first cycles at 20°C of one of the four cells composed of Timcal SLP30 and the 2:2:3:3 EC:PC:EMC:DMC (E3) electrolyte.

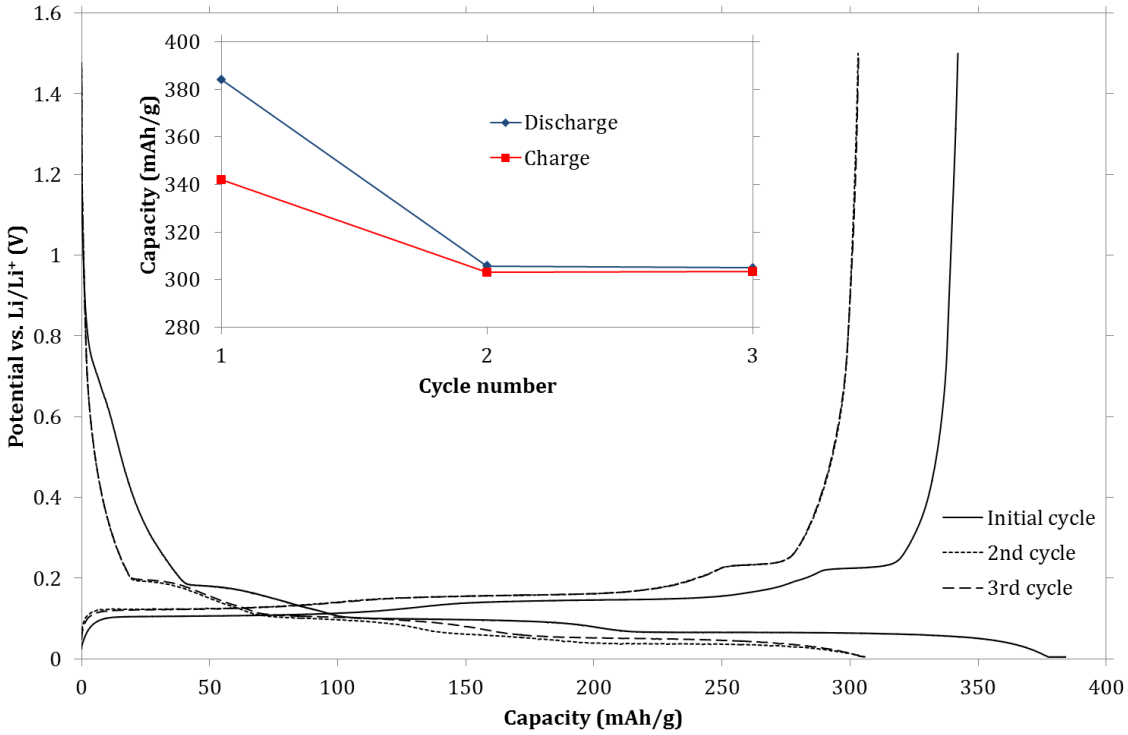

Figure 43: Cycling behaviour for the three first cycles at 20°C of one of the four cells composed of Timcal SLP30 and the 1:2:2 EC:EMC:DMC (E4) electrolyte.

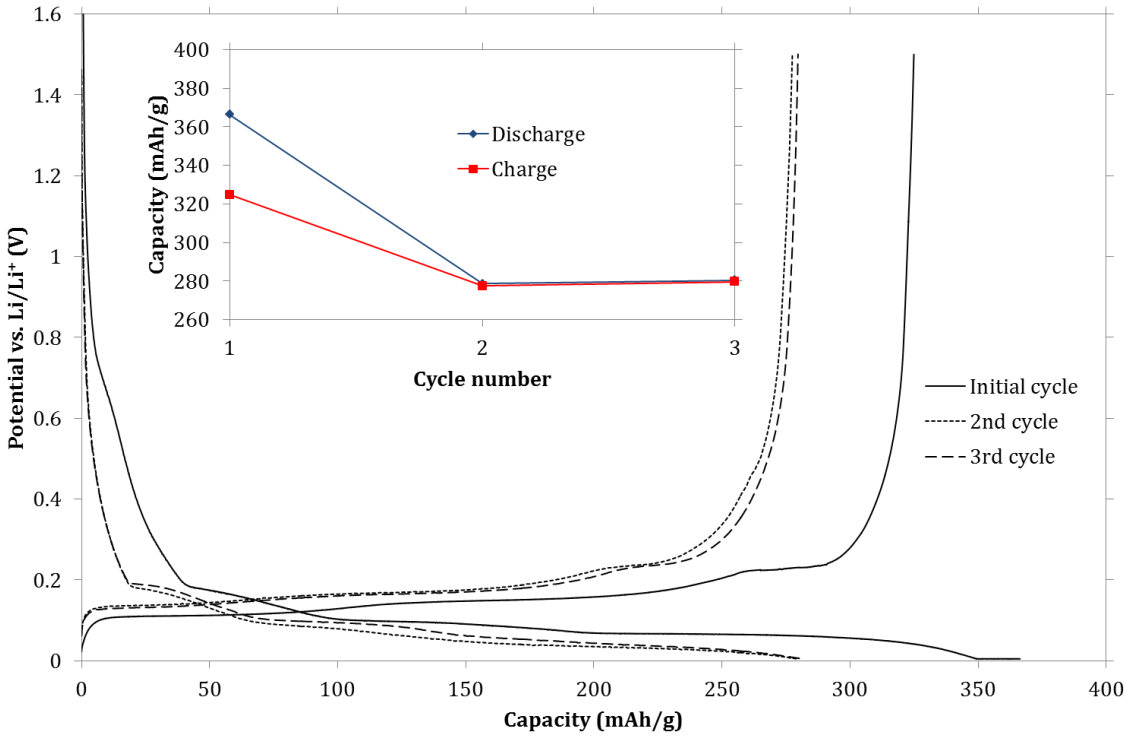

Figure 44: Cycling behaviour for the three first cycles at 20°C of one of the four cells composed of Timcal SLP30 and the 1:1:3 EC:EA:EMC (E5) electrolyte.

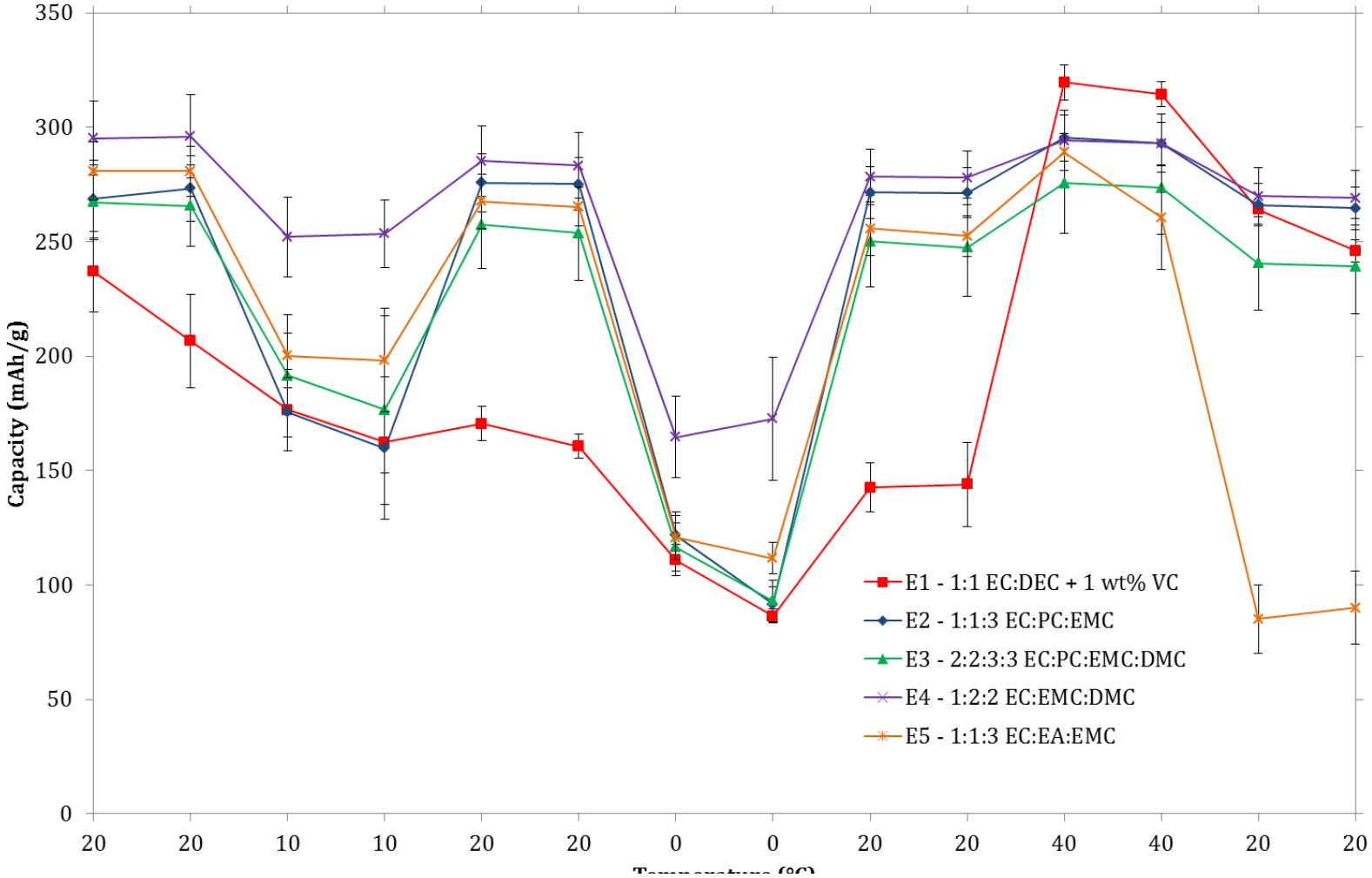

Figure 45: Average charge capacity for each cycle indicated with the chamber temperature for cells composed of Timcal SLP30 and each of the five electrolytes.

Largely speaking, all the above cells have the same cycling behaviour for the three first cycles at 20°C. In the first cycle there is an irreversible capacity loss caused by SEI formation, but the capacity stabilises for the next two cycles at C/8. The average ICL and initial and 3rd charge capacity values with standard deviations for all SLP30 cells for temperature cycling are presented in Table 9. The initial charge capacity represents the maximum reversible capacity (at C/37) of the cell, while the 3rd charge capacity (at C/8) relates of the rate capability of the cell.

Table 9: Performance characteristics of SLP30 cells for temperature cycling

Electrolyte	ICL (%)	Initial charge capacity (mAh/g)	3rd charge capacity (mAh/g)
E1	13.0 ± 0.2	341 ± 7	263 ± 11
E2	26.7 ± 2.8	335 ± 6	295 ± 14
E3	30.7 ± 1.8	326 ± 16	263 ± 14
E4	11.4 ± 0.6	334 ± 11	302 ± 1
E5	11.7 ± 0.8	333 ± 11	287 ± 11

There are some interesting trends to draw from the above data. Both of the PC-containing cells (E2 and E3) have significantly higher ICL values than the other electrolytes. Referring to Figure 3, the initial discharge curves in Figure 41 (E2) and Figure 42 (E3) also show signs of more electrolyte decomposition than the other cells. Accordingly, there seems to be more SEI formation in the cells containing E2 and E3. Nevertheless, the initial and final charge capacities at 20°C for these electrolytes do not significantly differ from the values obtained for the other electrolytes. Plausible explanations for this, as well as a thorough discussion of the cycling behaviour at 20°C, will be provided in chapter 5.3.2.

Figure 45 shows that the available capacity in Li-ion cells is highly dependent on the temperature. Even upon cycling at 10°C, the capacity of the cells is sliced by around 1/3, while at 0°C the cells retain about half of the room temperature capacity. Furthermore, it is clear that there is a significant difference in cell performance at lower temperatures for binary and multi-component electrolyte compositions. Notably, the capacity of the cells using the binary electrolyte E1 does not fully recover after being heated to 20°C, only when heated to 40°C. In contrast, all the multi-component electrolyte cells completely recover their capacity after being heated to 20°C, regardless of the previous cycling temperature. Interestingly, the cells containing the E5 electrolyte do not tolerate cycling at 40°C, as their capacities afterwards drop to less than 100 mAh/g. The cells composed of electrolyte E4

perform best, having generally the highest capacity, and retaining most of the capacity when cycled at 10 and 0°C. Except for the cells containing electrolyte E5, the capacity of the cells at the end of the temperature program is quite close to the capacity at the beginning. The processes occurring in the cells causing the capacity to decrease at lower temperatures are thus mostly reversible upon warming the cells again.

As mentioned in chapter 3.3, the cells prepared for thermal analysis were discharged to 5 mV at slow rate (C/37) before disassembly. These discharge capacity values (defined as retained capacity) are summarised in Table 10. These values represent how well the cell capacity is retained through the temperature cycling program, i.e. how well the different electrolytes tolerate cycling at different temperatures and their general cycling stability.

Table 10: Retained capacity of SLP30 cells after temperature cycling

Electrolyte composition	Retained capacity (mAh/g)
E1 - 1:1 EC:DEC + 1 wt% VC + 1M $LiPF_6$	315 ± 0.0
E2 - 1:1:3 EC:PC:EMC + 1M $LiPF_6$	280 ± 3.6
E3 - 2:2:3:3 EC:PC:EMC:DMC + 1M $LiPF_6$	285 ± 6.5
E4 - 1:2:2 EC:EMC:DMC + 1M $LiPF_6$	311 ± 3.0
E5 - 1:1:3 EC:EA:EMC + 1M $LiPF_6$	15.3 ± 1.2

Table 10 shows even more clearly that the cells composed of the E5 electrolyte have failed after cycling at 40°C, having capacities close to 0 mAh/g. Apart from that, the PC-containing cells have the lowest capacities, meaning that there has indeed been higher irreversible capacity loss in these cells. The cells using the binary electrolyte E1 display the highest capacities, further supporting that the processes causing lower capacity with this electrolyte at reduced temperatures are reversible upon sufficient heating. The above table confirms the high performance of electrolyte E4, as the corresponding cells have retained a large fraction of their capacity through the temperature cycling program. The processes and changes occurring in the cells on temperature reduction and the resulting performance differences will be more closely inspected and discussed in chapter 5.3.2.

4.4.2.2 Temperature cycling of CPreme P5 cells

Figure 46 and Figure 47 show the cycling behaviour of the three initial cycles for cells composed of CPreme P5 and electrolytes E2 and E4. Figure 48 displays the capacity of the same cells when cycled at different temperatures.

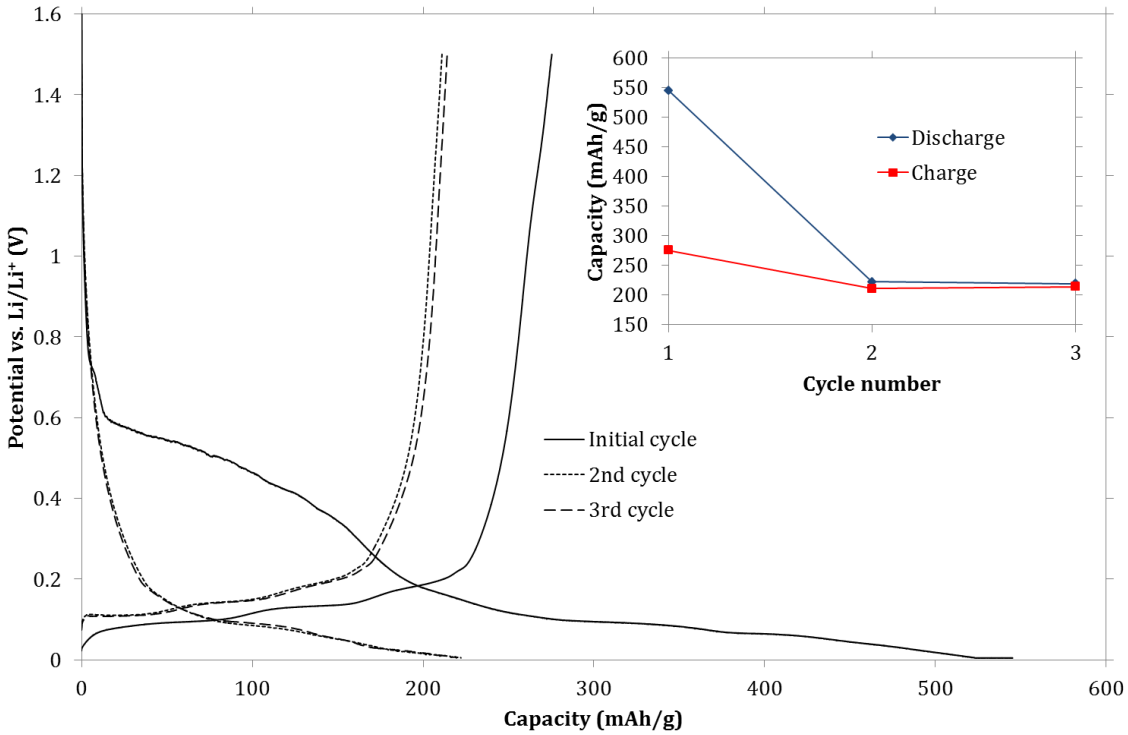

Figure 46: Cycling behaviour for the three first cycles at 20°C of one of the four cells composed of CPreme P5 and the 1:1:3 EC:PC:EMC (E2) electrolyte.

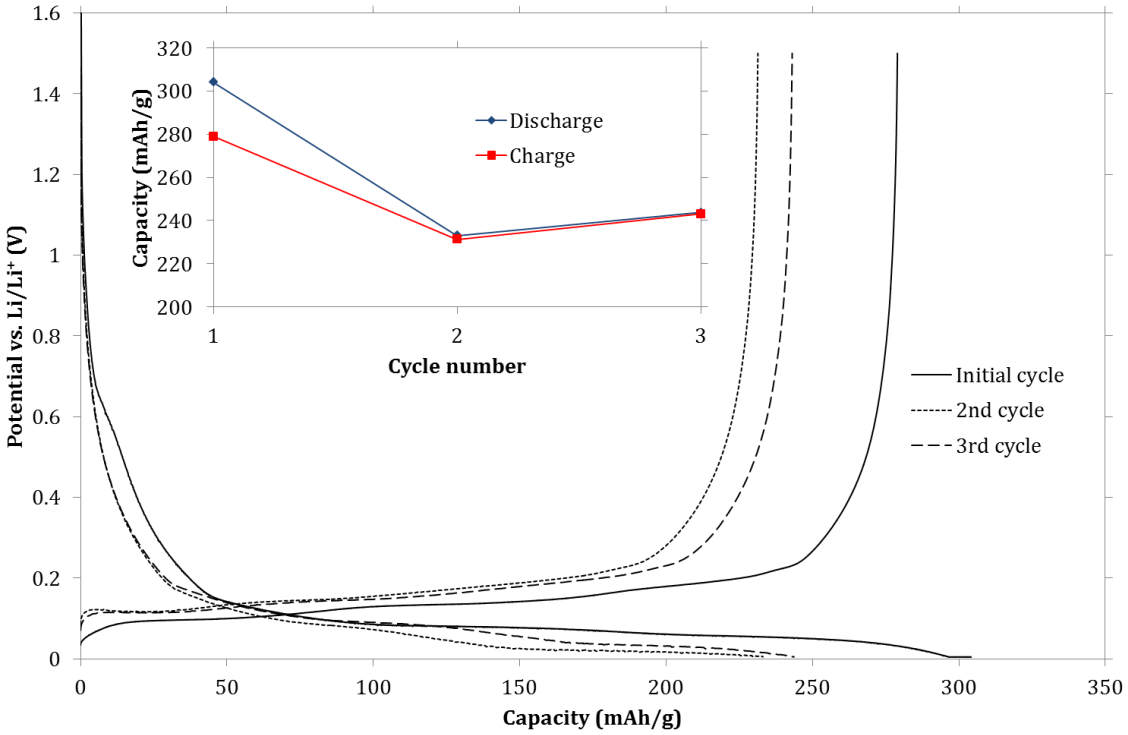

Figure 47: Cycling behaviour for the three first cycles at 20°C of one of the four cells composed of CPreme P5 and the 1:2:2 EC:EMC:DMC (E4) electrolyte.

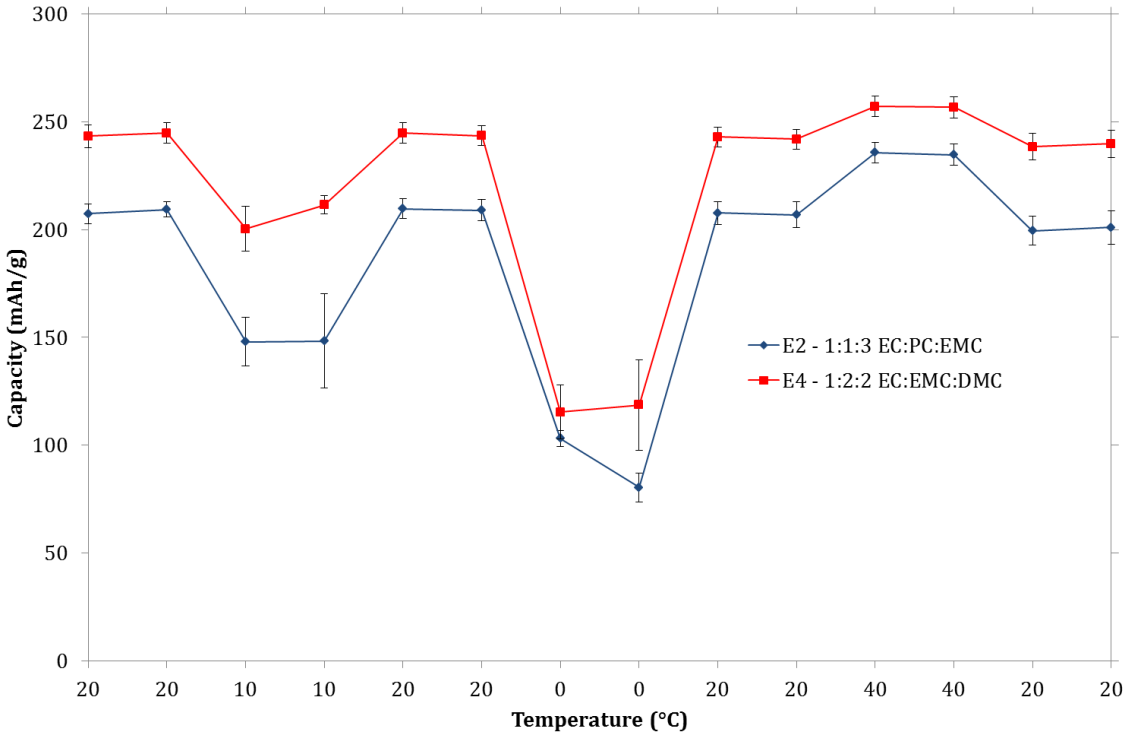

Figure 48: Average charge capacity for each cycle indicated with the chamber temperature for cells composed of CPreme P5 and the 1:1:3 EC:PC:EMC (E2) and 1:2:2 EC:EMC:DMC (E4) electrolytes.

Table 11: Performance characteristics of P5 cells for temperature cycling

Electrolyte	ICL (%)	Initial charge capacity (mAh/g)	3rd charge capacity (mAh/g)
E2	50.3 ± 0.9	269 ± 6	212 ± 4
E4	8.2 ± 0.1	277 ± 4	244 ± 5

There are significant differences in the cycling behaviour of the E2 and E4 electrolytes when CPreme P5 is used. For cells containing electrolyte E2, extensive electrolyte decomposition can be observed in the initial discharge curve (Figure 46), resulting in very high ICL values as shown in Table 11. The initial charge capacities, however, are fairly comparable for all the cells. Nonetheless, the cells using the E4 electrolyte have retained more of the capacity after the three first cycles with an average over 240 mAh/g. On the other hand, the cells containing electrolyte E2 had a capacity of about 210 mAh/g after the three cycles. The capacity increase between the 2nd and 3rd cycle in the E4 cells might be caused by SEI re-structuring as previously explained. Possible reasons for the higher degree of electrolyte decomposition observed for the P5 graphite compared to SLP30, along with other features and trends, will be further discussed in chapter 5.3.2.

The cell capacities during temperature cycling of the two electrolytes show a continuation of the trend in the pre-temperature cycling. Roughly, the capacity difference established during the initial three cycles stays constant in all the subsequent cycles, relatively independent of the temperature. Once again, cells using the E4 electrolyte proved to have the highest capacity, also at lower temperatures. For the temperatures investigated here, the CPreme P5 graphite generally displayed lower capacity than the Timcal SLP30 graphite. Table 12 shows the retained capacities obtained for cells containing the two electrolytes when discharged at a slow rate (C/37) after the end of temperature cycling.

Table 12: Retained capacity of P5 cells after temperature cycling

Electrolyte composition	Retained capacity (mAh/g)
E2 - 1:1:3 EC:PC:EMC + 1M $LiPF_6$	247 ± 1.7
E4 - 1:2:2 EC:EMC:DMC + 1M $LiPF_6$	269 ± 5.1

The above values confirm that there has indeed been a higher irreversible capacity loss in the cells containing E2 than for those with E4, further supporting the superiority of electrolyte E4. More thorough discussion regarding the cycling

behaviour, temperature dependency of the capacity, and performance difference between CPreme P5 and Timcal SLP30 will be undertaken in chapter 5.3.2.

5 Discussion

The discussion will deal with the results in similar order as they were presented in chapter 4. The results from low temperature thermal analysis of pure electrolytes will be utilised to support the findings from low temperature electrochemical cycling. Also, attempts will be made to correlate the results from electrochemical cycling with the high temperature DSC analyses. Furthermore, the results from the surface structure characterisation and nitrogen adsorption measurements will be used as a foundation for the discussion. Therefore, these results will be treated initially.

Before beginning the discussion, it should be remembered that the three graphites studied in this work are commercially available materials and hence are expected to display excellent cyclic and thermal stability. Consequently, no substantial performance differences were anticipated between the graphites in the experiments conducted. However, small differences were still discovered. In contrast, the performance of the electrolyte compositions studied, especially at lower temperatures, was expected to differ and the experiments confirmed this. The discussion will attempt to explain the observed performance variations.

5.1 Surface characterisation

The micrographs in Figure 27 show striking similarities in the surface structure and morphology of the graphite materials. The three graphites all consist of potato-shaped particles with a smooth particle surface to minimise the specific surface area. In fact, from the micrographs alone it is difficult to see any significant difference in the surface structure of the graphite materials. The nitrogen adsorption measurements, capable of probing surface characteristics with considerably higher precision than SEM, revealed some interesting differences. The table summarising the results from the nitrogen adsorption measurements is reproduced below for convenience.

Table 13: Graphite surface properties

Surface properties	Timcal SLP30	CPreme G8	CPreme P5
BET surface area (m^2/g)	6.16 ± 0.03	1.79 ± 0.03	3.48 ± 0.04
DFT surface area (m^2/g)	6.46	1.88	3.69
Edge plane surface area (m^2/g)	2.23	0.35	0.83
Basal plane surface area (m^2/g)	2.86	1.53	2.85
Defect surface area (m^2/g)	1.37	0	0
Ratio of basal:edge:defect areas (%)	44:34:21	81:19:0	77:23:0
Ratio of basal:"non-basal" areas (%)	44:56	81:19	77:23
Total area in pores (m^2/g)	2.41	0.6	1.2
% of surface area in pores (%)	37	33	33

The BET surface area values contradict the expected values after the SEM analysis. Because SLP30 is composed of the largest particles, it is expected to have the lowest specific surface area. It is obvious; however, that much of the surface structure of the graphites is not noticeable in the micrographs. For example, about 1/3 of the surface area is present in pores which are not visible in the micrographs. Even though the shape of the pore size distributions, seen in Figure 29, is relatively similar for all three materials, SLP30 has much more area contained inside pores. Additionally, the surface of SLP30 seems to be more heterogeneous and rougher than in the CPreme graphites. The defect surface area of SLP30 is 1.37 m^2/g, while the CPreme graphites do not contain any surface defects. These factors could explain the higher BET surface area value for SLP30.

The different extents of edge plane, basal plane and defects in Timcal SLP30 and the CPreme materials are noteworthy. Whereas the surface of SLP30 contains as much as 21% defects, there are no measureable defects in CPreme G8 or P5. By inspecting Figure 28, especially G8, on which only three different adsorptive potentials are measured, seems to have high uniformity within the edge- and basal plane surface areas. We have reasons to believe that this can be explained by the nature of the surface coating surrounding the graphite particles. According to Phillips 66 [63], the CPreme materials have "graphite-on-graphite coating", i.e. crystalline carbon coating. Such a coating should produce a homogeneous surface with minimum amount of defects. The Timcal SLP30 particles have also been subjected to surface treatment [62], likely yielding a coating surrounding the particles. The greater amount of surface defects in SLP30 indicates that the coating is less crystalline than that on the CPreme particles. Moreover, SLP30 has a greater extent of edge plane surface area than both of the CPreme materials. The ratio of basal to "non-basal" plane surface

areas is consequently much higher for the CPreme graphites. In line with Placke et al.'s [36] findings, this should result in lower ICL in Li-ion cells using CPreme G8 and P5 compared to cells using Timcal SLP30.

The presence of nano-scale surface defects, treated in chapter 2.4.2, was considered essential to obtain an effective surface passivation and avoid exfoliation, according to Novák et al. [28]. This result appears to be inconsistent with the results above, knowing that both CPreme materials performed well during electrochemical cycling. We believe that the type of surface defects found during the nitrogen adsorption measurements cannot be directly compared to the type of defects measured with oxygen chemisorption. In any case, the apparently defect-free surface of the CPreme materials did not deteriorate the surface passivation and consequent graphite performance in the cells cycled during this work.

It should be noted that the results from nitrogen adsorption measurements cannot be directly used to predict the electrochemical cell performance. Untreated powder samples, which were utilised for the measurements, are inherently different to the composite heterogeneous graphite electrodes utilised in the cells. Particularly, the quantitative ratios of different surface areas cannot be expected to remain entirely unchanged after the powders have been tape casted. This should be remembered when using the above results to interpret the data from thermal analysis and electrochemical cycling. Nevertheless, the broader lines of the results should be possible to employ in the further discussion.

5.2 Thermal analysis

5.2.1 Low temperature DSC analysis

The most useful information acquired from low temperature DSC analyses between -80 and +50°C is the liquidus transition temperatures of the electrolytes. The temperature translates to the lowest expected operating temperature of an electrolyte composition in a Li-ion cell, thus limiting possible applications. These results and their implications will be further examined in chapter 5.3.2.

Each endothermic response in the DSC heating curves corresponds to the melting of an electrolyte component. As previously mentioned, the response observed at the highest temperature is probably due to the melting of EC, which in its pure form has the highest melting point at 36°C. When mixed with other components with lower melting points to form a solution, its melting point is obviously reduced. It is more

difficult to unravel the causes for the more complex thermal features occurring at lower temperatures in the curves of e.g. electrolytes E1 and E5. Simultaneously, electrolytes E2 and E3 display only one peak upon heating, even though they are both composed of three components. This behaviour might be explained by compositional proximity to the eutectic composition, or similar melting points of the electrolyte components. Both of these situations would result in melting of several components over a narrow temperature interval, which could result in overlapping melting peaks. For example, PC and EMC melt at -49 and -53°C, respectively, meaning that these components will likely produce one single broad melting peak. Additionally, from the ternary phase diagram of EC-EMC-DMC produced by Ding [55], it can be rationalised that the endothermic response for electrolyte E4 at about -70°C is due to melting of both EMC and DMC. Without knowing all the relevant ternary phase diagrams, it is difficult to unravel the precise origins of all the other observed thermal responses.

The process causing the exothermic response present with different magnitudes in all the DSC curves between -40 and -70°C has not yet been unravelled. Since it appears, to some degree, in all the DSC curves it is suspected to be due to a salt transition. Low temperature DSC analyses of the same electrolyte compositions with different concentrations of $LiPF_6$, including no $LiPF_6$, could verify this hypothesis.

5.2.2 High temperature DSC analysis

Most importantly, the DSC curves from high temperature analysis of pure electrolytes, shown in Figure 31, illustrate that the electrolytes thermally decompose in approximately the same temperature interval, between 200 and 300°C. Apparently, the magnitude of the heat evolution from the decomposition varies somewhat for the different electrolytes. Particularly the electrolytes E1 and E3 appear to release more heat in the decomposition than the other electrolytes, which could be unfortunate in a thermal runaway situation. On the other hand, this heat evolution is highly dependent on the amount of electrolyte in the sample holder, which could vary with pipetting/sampling technique, among other things. As a consequence, the differences in heat production above 220°C, also in later figures, are not given much attention.

Figure 32 compares the thermal stability of the three graphites after 12 discharge-charge cycles at room temperature, using electrolyte E1. Overall, all three graphites exhibit high thermal stability and very low heat output below 200°C. As mentioned, this heat evolution is due to SEI transformation and direct reaction between lithiated

graphite and electrolyte through the SEI layer. The low heat evolution thus indicates that the SEI layers present on the graphites are stable, and that the SEI formation has been limited. This finding is consistent with the low BET surface areas and the low ICL values from electrochemical cycling at room temperature, ranging from only 8 to 13% for the different graphites. Notably, CPreme P5 is the only material which shows any sign of evident thermal response below 200°C. In addition to the minor exothermic peak at about 80°C, there seems to be slightly more heat output afterwards as well. This is indicative of a marginally less stable SEI layer. Interestingly, SLP30 does not display the similar behaviour, even when expected to have more SEI due to higher ICL value (12.9% for SLP30 vs. 11% for P5). Nonetheless, the deviating thermal behaviour is not considerable.

There seems to be a correlation between the heat output below 200°C and the onset temperature of exfoliation. It is known that the transformation of SEI results in the evolution of gaseous species [45]. The critical pressure to initiate exfoliation might thus be reached at a lower temperature in the case of increased SEI transformation. Indeed, this could be the case for CPreme P5, where the exfoliation clearly initiates at a lower temperature than for the other two graphites.

Generally, one can conclude that all the graphites demonstrate high thermal stability after 12 discharge-charge cycles conducted at room temperature when using the binary electrolyte E1.

First and foremost, the DSC curves in Figure 33 show that the magnitudes of the thermal responses occurring below 200°C have increased after the graphite has been cycled at different temperatures. The effect of the different cycling programs can be observed by comparing the SLP30 curve in Figure 32 with the E1 curve in Figure 33. The onset temperature of SEI transformation is about 70°C in the E1 curve while the SLP30 curve in Figure 32 hardly features any heat response below 200°C. This can probably be explained by increased SEI formation in the temperature cycled graphite. The reduced capacity of the temperature cycled SLP30 cells (Table 10) compared to those cycled at room temperature (Table 8) supports this explanation.

The electrolyte compositions seem to have influenced the stability of the SEI layer. With the exception of electrolyte E5, the SEI layer of the binary electrolyte E1 has the lowest transformation onset temperature, about 70°C. Electrolytes E2, E3 and E4 all produce SEI layers which start transforming above 100°C. This is surprising as the E1 composition is known to create a stable SEI layer [22, 39, 46, 47]. However, the

SEI transformation peak in the samples with electrolyte E2 and E3 is higher than for electrolyte E1. Again, this can likely be explained by more extensive SEI formation in the graphites cycled with E2 and E3, justified in Table 10. Nevertheless, the curves generally indicate that the use of novel multi-component electrolytes has not deteriorated the chemistry and stability of the SEI layer. Particularly the graphite cycled with electrolyte E4 exhibits low heat output over the entire temperature interval.

The thermal behaviour of the graphite sample cycled with the EA-containing electrolyte (E5) deviates significantly from the other samples. Notably, the sharp exothermic peak at about 75°C does not resemble the typical shape of the response caused by the transformation of SEI. Furthermore, there is very little heat evolution after this peak and until 200°C. The following thermal response resembles the electrolyte decomposition peak. From chapter 4.4.2.1, we know that the SLP30 cells containing electrolyte E5 failed after being cycled at 40°C (Table 10). Consequently, the graphite samples prepared for thermal analysis hardly contained any intercalated Li^+. Knowing that the reactions between 100 and 200°C require intercalated Li^+ to occur, it is evident why this sample shows no thermal response in this temperature interval. From the high temperature analysis of electrolytes in Figure 31, we can rule out that the peak at 75°C is related to electrolyte decomposition. Thus, it is most likely due to the transformation of SEI, which usually occurs around this temperature. With this conclusion, however, it is also clear that the composition of the SEI in this sample must be significantly different to the other samples. The sharpness of the peak implies that the SEI is more homogeneous than usual, possibly composed of fewer components. The nature of this SEI layer might contribute to the explanation of why the cells containing E5 failed after cycling at 40°C.

Once again, the thermal footprints of the samples are overall relatively small, further supporting that SLP30 is a good substrate for the formation of thermally stable SEI.

The DSC curves from analysis of temperature cycled CPreme P5 and electrolytes E2 (1:1:3 EC:PC:EMC) and E4 (1:2:2 EC:EMC:DMC) display the familiar features. The onset temperature is about 80°C in both curves. However, the heat output between 100 and 220°C is considerably larger for the sample with electrolyte E4. Moreover, the earlier onset temperature of exfoliation in this curve supports that there has been higher degree of SEI transformation in this sample. This is an unexpected result when comparing the cycling performance of these electrolytes with CPreme P5. The

ICL value, presented in Table 11, for electrolyte E2 was 50%, while it was only 8% for E4. An ICL value of 50% is very high, and usually an indication of exfoliation in the graphite structure. The exfoliation breaks up the graphite structure, exposes fresh lithiated graphite areas to the electrolyte which subsequently reacts to form SEI, consuming charge in the process [15]. This results in very high ICL values and extensive SEI formation. The DSC curves in Figure 34 do not support this hypothesis, as the heat generated from SEI transformation is not larger for electrolyte E2 compared to electrolyte E4. On the contrary, the heat output from the electrolyte E2 sample appears to be lower in the relevant temperature interval. Consequently, there must be some other process than exfoliation occurring in the graphite cycled with E2, which will be further examined in chapter 5.3.2.

Figure 35 compares the thermal stability of Timcal SLP30 and CPreme P5 after discharge-charge cycling at different temperatures with electrolytes E2 and E4. Similar trends can be observed for both electrolytes. Particularly the lower onset temperature of SEI transformation in CPreme P5 is notable, indicating that the SEI layer on P5 is less stable than that on SLP30. As described in chapter 2.4.2, the composition of the SEI layer on edge planes is considerably different to the composition on basal planes. The basal plane SEI contains mostly polymeric compounds from solvent decomposition, while the edge plane SEI is composed mainly of inorganic species, such as LiF, from salt decomposition [37]. Thus, it is not unlikely that the reactivity of the two SEI layers is different. The extent of basal planes on P5 and SLP30 was measured to be 77% and 44%, respectively. Accordingly, the lower onset temperature of P5 could be a result of basal plane prevalence, assuming that the basal plane SEI is less thermally stable. Unfortunately, no studies have been conducted on the thermal reactivity of the edge- and basal plane SEI layers to support this hypothesis.

For both electrolytes, the SEI reaction peak is highest for SLP30, indicating that there has been more SEI formation in these cells. This is consistent with the higher irreversible capacity loss and relatively lower retained capacity observed for the SLP30 cells after temperature cycling (Table 10) compared to the P5 cells (Table 12).

Both SLP30 and P5 generate approximately the same amount of heat before electrolyte decomposition at about 230°C, regardless of electrolyte composition. As a consequence, we cannot conclude that one of the graphite materials is more thermally stable than the other.

Figure 36 acts as a representation of the certainty and validity of the DSC curves shown and the conclusions drawn. The curves, from analysis of principally similar sample materials, evidently display that there are significant variations in the results, especially at higher temperatures. This is also the reason why the variations observed above 200°C have not been carefully examined. However, the curves from similar sample combinations do contain the same features at the same temperatures. Therefore, we think that the results and findings obtained are significant, even though the variations discussed may seem minor. Nonetheless, attempts should be made to improve upon the experimental method of analysing these materials, to further increase the accuracy of the results.

5.3 Electrochemical cycling

5.3.1 Room temperature cycling

Some selected graphite surface characteristics related to the irreversible capacity loss (ICL) in the initial cycle are reproduced in the table below.

Table 14: Graphite characteristics

Graphite material	ICL (%)	BET surface area (m^2/g)	Ratio of "non-basal":basal areas (%)
Timcal SLP30	12.9 ± 1.6	6.16 ± 0.03	56:44
CPreme G8	7.9 ± 0.1	1.79 ± 0.03	19:81
CPreme P5	11.0 ± 0.4	3.48 ± 0.04	23:77

Table 14 correlates the relevant properties of the graphite surface to the resulting ICL values observed for the initial cycle. Timcal SLP30, having the highest BET surface area, also displays the highest ICL. Also for the other graphites there is a positive relation between the BET surface area and ICL value. In addition, there is also a positive relation between the ratios of "non-basal" plane to basal plane surface areas and the ICL values, consistent with the results from Placke et al. [36]. These results thus support that there is more charge loss related to the SEI formation on edge planes and defect surfaces than on basal planes.

The different cycling behaviour of CPreme P5 and G8 shown in Figure 38 and Figure 39 is notable. However, it is most likely not related to the enhanced high rate capability of CPreme P5 compared to G8. In an optimised cell, the two graphites are expected to behave similarly when cycled at a rate of C/4, which is in fact quite slow. We believe that the thickness of the electrode sheet can have a large influence on the

rate capability of the resulting cell, even at relatively slow rates such as C/4. The thicker the electrode, the longer the diffusion distance for Li^+ within the electrode material before it can intercalate into the inner parts of the electrode, close to the current collector. For relatively porous electrodes with low density, the distance may become so large that it represents a kinetic limitation. From appendix C.1, the average thickness of the G8 and P5 electrodes are 78.9 and 58.5 μm, respectively. This difference could determine whether the resulting cell will experience kinetic limitations or not at a cycling rate of C/4. Furthermore, we think that minor variations during the cell assembly process, such as electrode alignment, could also influence the rate performance.

5.3.2 Cycling with temperature program

Before beginning the discussion of the temperature cycling results, the most important kinetic barriers in Li-ion cells at low temperatures, as presented in chapter 2.6.1, are listed:

- Diffusion of solvated Li^+ through electrolyte, limited by electrolyte conductivity
- Charge-transfer resistance at the electrolyte/SEI interface during removal of Li^+ solvation sheath
- Diffusion through the SEI layer
- Diffusion through the bulk of the graphite particles

From the above points it is evident that all the relevant components in the Li/graphite half cells manufactured in this work; electrolyte, graphite and SEI, deeply influence the low temperature performance.

Figure 45 compares the temperature performance of the different electrolytes when SLP30 is employed as graphite material. With the exception of the binary electrolyte E1, the electrolytes fully recover their capacity when heated to 20°C after cycling at a lower temperature. Apparently, the process causing reduced capacity with electrolyte E1 at 10 and 0°C is not reversible upon heating to 20°C, only upon heating to 40°C. The explanation could lie in the low temperature behaviour of electrolyte E1, shown in Figure 30. Electrolyte E1 was the only that displayed any thermal response above 0°C, due to melting of the EC component. Additionally, the liquidus transition temperature of electrolyte E1 was estimated to 5°C. It is thus expected that the E1 electrolyte partially solidifies when cooled to 0°C, which should significantly lower the cell performance. Ordering of the electrolyte, reducing the conductivity, might

even occur at a higher temperature, which might explain why the capacity is not fully recovered after cycling at 10 and 0°C.

We believe that the main reason for the lowered capacity observed for the other electrolytes at 10 and 0°C is reduced electrolyte conductivity due to increased viscosity. Recent electrochemical impedance spectroscopy studies by Svensson et al. [51, 71] support this belief. In addition to reduced electrolyte conductivity, increased charge-transfer resistance at the SEI/electrolyte interface was determined as the second most important factor causing lower capacity.

The superior performance of electrolyte E4 is likely related to the viscosity of the electrolyte composition. E4 is the only electrolyte composed of one cyclic carbonate (EC) and two linear carbonates (EMC and DMC). In fact, 80% of the solvents are linear carbonates. As written in chapter 2.3.1.2, linear carbonates generally display low viscosity. Thus, the presence of linear carbonates is therefore crucial to maintain the electrolyte conductivity, particularly at lower temperatures. The low temperature performance of electrolyte E4 confirms this. Notably, only 20% solvent concentration of EC is sufficient to obtain good surface passivation of the graphite. The cells composed with electrolyte E4 actually had the lowest ICL, the highest capacity after the 3rd cycle at 20°C, and retained a large fraction of the capacity after the temperature cycling. In conclusion, the 1:2:2 EC:EMC:DMC composition with 1M $LiPF_6$ balance well several important electrolyte properties, however, it may not be used for the most extreme purposes as it partially solidifies at about -30°C.

PC has been studied as an electrolyte component for many years due to its favourable low temperature performance compared to EC. Mostly, this is because of the much lower melting point of PC at -49°C, while pure EC freezes at 36°C. However, PC is also notorious for co-intercalating into the graphite structure, causing exfoliation due to its decomposition or simply the immense volume change of about 100% related to the co-intercalation [72]. In this work, two electrolyte compositions (E2 and E3) employing PC were studied. In the pre-temperature cycling at 20°C, increased electrolyte decomposition was observed in the initial cycles for these electrolytes (Figure 41 and Figure 42). Interestingly, the following charge capacity of the cells was not significantly lower, indicating no severe exfoliation. After the temperature cycling, however, the cells using electrolytes E2 and E3 had retained less capacity than the cells using electrolytes E1 and E4, which did not contain PC. Thus, there has been increased capacity loss in the PC-containing cells. Possible

reasons are exfoliation causing extensive SEI formation or simply formation of thicker SEI layer.

The performance of the PC-containing electrolytes at lower temperatures, 10 and 0°C, was not significantly improved compared to the binary electrolyte E1. This supports our hypothesis that the electrolyte conductivity is an important factor. Both PC and EC are cyclic carbonates and consequently display high viscosity, leading to inherently low conductivity. The effect of the lower melting point of PC compared to EC is expected to be more evident when cycling at even lower temperatures. From the low temperature DSC analysis, both of the PC-containing electrolytes will be liquid until at least -45°C. In fact, only these two electrolytes should be completely liquid at that temperature. With the current cycling program, exposing the cells to temperatures between 0 and 40°C, electrolyte conductivity plays the crucial role. In order to further investigate the influence of replacing EC with PC, cycling at even lower temperatures should be conducted.

The composition of electrolyte E5 stands out from the other electrolytes. As the only electrolyte, it contains an ester co-solvent, ethylene acetate (EA). Along the lines of the recent article by Smart et al. [7], we wanted to examine the effect of an ester co-solvent on the low temperature performance. Due to their low viscosity at low temperatures, esters have been increasingly studied as electrolyte co-solvents, particularly by the research group of Smart. In our studies, however, the performance of electrolyte E5 at 10 and 0°C was only marginally better than the binary electrolyte E1 and the PC-containing electrolytes E2 and E3. This indicates that the EA-addition has not significantly increased the electrolyte conductivity at these temperatures, which is surprising. There were some issues regarding the preparation of this particular electrolyte. Not all the lithium salt would dissolve in the solution, leaving the excess dispersed. The insoluble lithium salt might well deteriorate the viscosity and resulting conductivity of the electrolyte, explaining the unexpectedly poor performance of this composition.

Furthermore, it is evident that the cell containing electrolyte E5 did not tolerate cycling at 40°C, as the capacity dropped to almost 0 mAh/g in the following cycles (Table 10). Initially, we thought that this was directly related to the decomposition of the electrolyte at this temperature, as low molecular weight esters are known to display poor high temperature resilience [7]. However, the high temperature DSC analysis of the pure electrolytes showed that this was not the case, as electrolyte E5 did not decompose before being heated to 200°C. Instead, it is believed that the cause

of failure is related to the nature of the SEI layer. As most other electrolyte components, EA is expected to electrochemically reduce at low potentials vs. Li/Li^+, contributing to the SEI layer formation. The exact reduction potential of EA, however, is not known. If it is only slightly higher than the reduction potential of EC, the decomposition products of EA would be positioned near the graphite. If these components are not thermally stable at 40°C, they will further decompose and could deteriorate the SEI layer from the inside at this temperature. Extensive exfoliation causing destruction of the graphite structure would follow, reducing the cell capacity to nothing. Notably, the processes causing the cell capacity to diminish must be kinetically slow as many hours pass from when the cells are initially heated to 40°C to when the capacity is completely lost. The high temperature DSC analysis of temperature cycled SLP30 cells using electrolyte E5 supports the above explanation. Decomposition of the SEI layer might result in a more homogeneous SEI layer, consisting of fewer components. The transformation of this SEI layer would occur over a narrow temperature region, explaining the sharper transformation peak in Figure 33. Importantly, however, further investigations must be conducted to reinforce this hypothesis.

Largely speaking, the low temperature performance of electrolytes E2 (1:1:3 EC:PC:EMC) and E4 (1:2:2 EC:EMC:DMC) when using CPreme P5 as graphite material (Figure 48) follows the similar trend as for SLP30. During the entire temperature cycling program, the cells containing electrolyte E4 exhibit higher capacity than the cells using electrolyte E2. In fact, the relative capacity difference between the electrolytes at 20°C is larger when CPreme P5 is utilised compared to SLP30. Apparently, the capacity difference established during the initial three cycles performed at 20°C remains relatively constant during the temperature cycling program. Even after the temperature cycling program, the electrolyte E4 cells have retained a larger fraction of the capacity than the cells containing electrolyte E2.

The remarkable cycling behaviour of electrolyte E2 in the three initial cycles, displayed in Figure 46, can shed some light on why this electrolyte performs worse than electrolyte E4. Apparently, there is extensive electrolyte decomposition in the initial cycle of electrolyte E2. As previously mentioned, such behaviour is usually associated with exfoliation of the graphite structure. Knowing the character of the carbon coating surrounding the CPreme P5 particles, this explanation seems rational. The nitrogen adsorption measurements confirmed that the CPreme coating is highly crystalline, with minimum amount of defects. Thus, the CPreme coating might be more sensitive to co-intercalation of PC than the more amorphous coating on the

SLP30 particles. Indeed, there seemed to be a lesser extent of electrolyte decomposition in the corresponding SLP30 cell containing electrolyte E2, shown in Figure 41. Interestingly, the apparent co-intercalation of PC molecules into the graphite structure of P5 has not brought about extensive exfoliation, as the capacity stabilises well above 200 mAh/g before the temperature cycling. Furthermore, the E2 electrolyte cells function acceptably through the temperature cycling program, and the final retained capacity of these cells is not very far behind the capacity of the corresponding E4 cells. It appears that the P5 particles have resisted the exfoliation usually related to PC-intercalation. The smaller particles of P5 might have improved tolerance for the volume change related to PC-intercalation. Nevertheless, the trapped PC molecules represent a barrier for Li^+ intercalation which could explain the lower performance of electrolyte E2.

By comparing the general cycling behaviour of Timcal SLP30 (Figure 45) and CPreme P5 (Figure 48) during the temperature cycling program, one cannot conclude that either of the graphites perform better than the other. At the temperatures studied, it seems that the electrolyte and SEI properties have much higher influence on the performance than the graphite properties. Nonetheless, at even lower temperatures, for example -40°C, it is expected that CPreme P5 will perform better due to smaller particle size and shorter Li^+ diffusion distance.

In conclusion, there are strong indications that the electrolyte properties, particularly its conductivity, mainly influence the performance of Li-ion cells at temperatures down to 0°C. It has been confirmed that increased conductivity and performance can be achieved by employing multi-component electrolytes. The binary electrolyte E1 displayed the poorest performance; the capacity of the corresponding cells was not recovered before heating the cells to 40°C. All the multi-component electrolytes resulted in cells which performed generally better, fully recovering their capacity when heated to 20°C after being cycled at a lower temperature. Notably, electrolyte E4 composed of 80% linear carbonates and 20% EC exhibited high performance, both with respect to surface passivation, cycling at lower temperatures, and even thermal stability. Furthermore, there are clear indications that the rate properties of the graphite are not essential at the temperatures studied here.

6 Conclusion

Above all, this work has confirmed the importance of the solid electrolyte interphase (SEI) layer, influenced by both the properties of the electrolyte and graphite, between which the SEI is formed. Both the thermal stability and the temperature dependency of the performance of Li-ion cells were found to be highly dependent on the SEI properties.

Three commercially available graphite materials have been examined in this work; Timcal SLP30, CPreme G8 and CPreme P5. All three materials exhibited high thermal stability after being electrochemically cycled at room temperature. When SLP30 and P5 were subjected to cycling at temperatures between 0 and 40°C, the thermal stability was found to decrease, as the materials generated more heat during the thermal analysis. The reduced thermal stability was attributed to increased SEI formation. Furthermore, it was discovered that both the electrolyte composition and the graphite properties influenced the SEI properties, though in different ways. Specifically, the prevalent surface type present on the graphite might affect the SEI stability and the onset temperature of its transformation. Additionally, the composition of the electrolyte probably partially determined the extent of SEI formation. As an example, employing electrolytes containing propylene carbonate (PC) resulted in increased SEI formation and intensified heat evolution during the thermal analysis. Nevertheless, the magnitudes of the thermal reactions were still relatively limited, further demonstrating that the materials were good substrates for SEI formation.

The electrochemical cycling performance of five different electrolyte compositions was examined for temperatures between 0 and 40°C. Even for relatively mild temperature reductions, substantial capacity decrease was observed. Maintaining low viscosity and consequently high conductivity of the electrolyte was found essential to improve the cell performance at lower temperatures. In order to achieve this, the composition should consist of at least three components to create a disordering effect of the electrolyte. Also, linear carbonates or other low viscosity components should make up most of the composition. The electrolyte with the highest performance at lower temperatures was composed of 80% linear carbonates and 20% ethylene carbonate (EC); 1:2:2 EC:EMC:DMC. In addition, the results indicate that this electrolyte contributed to good surface passivation and high thermal stability. The use of PC to improve the low temperature electrolyte performance should be limited. The current results indicate that PC reduced the

capacity by exfoliation and/or extensive SEI formation, without significantly improving the low temperature performance. Finally, our results show that employing the ester co-solvent ethylene acetate (EA) has dire implications on the high temperature resilience of the Li-ion cell, as the relevant cells failed after being cycled at 40°C.

7 Further work

Through the course of this work, it has become clear that the results obtained here might produce more questions than answers. The main reason is that most of the processes and reactions causing the observed behaviour, both with respect to the results from thermal analysis and electrochemical cycling, are not clear and simple. Usually, several effects are at work, and often their interactions are perhaps more important than the effects alone. This was indicated in both the summaries from the literature study on thermal stability, in chapter 2.5.3, and from the literature study on low temperature performance, in chapter 2.6.4. Generally, the results and discussion presented in this thesis confirm this. The natural consequence of this is that even though several interesting observations have been made as part of this work, the actual reasons are unknown and requires further analysis to be unravelled. The most probable explanations have been elucidated and presented in chapter 4 and 5.

In order to verify that the results from thermal analysis, involving relatively minor differences regarding the heat output, are indeed significant, the analysis method should be improved. The most obvious way of doing this is to conduct the measurements on a modern and more accurate DSC instrument. Conducting the high temperature analyses proved challenging on the current instrument, mostly due to baseline variation.

The validity of several of the hypotheses presented in this work could be checked by further analysis. For instance, the process behind the failure of the cells containing electrolyte E5 when cycled at 40°C was reasoned to be transformation of the SEI layer from passivating to non-passivating. High temperature DSC analysis of graphite previously cycled with electrolyte E5 below 40°C might reveal whether there is a process occurring at about 40°C in the SEI layer. The sample should be very slowly heated, as the process itself appears to be kinetically slow. In addition, SEM analysis might reveal microstructural changes due to for example exfoliation in the failed graphite. Similarly, minor exfoliation in the graphite cycled with PC could possibly also be observed in high magnification micrographs. Lastly, the processes behind the interesting behaviour of CPreme P5 cycled with the PC-containing electrolyte might be revealed by in situ X-ray diffraction (XRD) studies. The current hypothesis suggests that the PC-molecules are co-intercalated but do not exfoliate the graphite structure. This is justified by the extensive electrolyte decomposition observed in the initial cycle without the usual accompanying capacity loss. The expected volume

increase of the CPreme P5 particles due to the co-intercalation could be observed by the in situ XRD studies, which would verify the present hypothesis.

To the best of our knowledge, no systematic study has yet been conducted to find the thermal stability of the edge plane- and basal plane SEI layers. As previously mentioned, the SEI on the basal plane is rich in organic compounds while the edge plane SEI is rich in inorganic compounds. Thus, it seems logical that the thermal stability of the two SEI layers might be different. In chapter 5.2.2, this was utilised to explain the earlier onset temperature of the SEI transformation observed for CPreme P5 compared to Timcal SLP30. In order to verify this, a systematic study combining both nitrogen adsorption measurements, to obtain the extents of edge and basal planes, and subsequent thermal analysis should be conducted.

Electrochemical impedance spectroscopy (EIS) could be utilised to reveal the significance of the various parameters behind the varying low temperature performance of Li-ion cell. In theory, the quantitative contribution of each of the kinetic barriers present in a Li/graphite cell can be calculated from such a study. Thus, EIS studies could verify the currently proposed explanation.

From the current work, it is clear that the performance of Li-ion cells is highly dependent on temperature. Even for quite mild temperature reductions to 10 and 0°C, significant performance decrease was observed. However, it is not uncommon for Li-ion batteries to experience temperatures far below these, at least not in Norway. Thus, it would be interesting to cycle cells at even lower temperatures, e.g. -20 and -40°C. At these temperatures it is furthermore expected that the graphite properties, such as particle size, start to influence the performance of the resulting cell. Accordingly, it would be interesting to compare the performance of CPreme P5 and Timcal SLP30 at temperatures below -20°C, in order to find the significance of the graphite properties.

Finally, this work has shed some light on the importance of the electrode thickness on the rate capability of Li/graphite half cells. In order to build cells of the highest possible quality with the current starting materials, optimisation of the graphite slurry preparation and tape casting process should be conducted. Ideally, the resulting electrode sheet should be as thin, compact and homogeneous as possible. Possibly, this can be achieved by tuning parameters such as the viscosity of the graphite slurry and the speed of the doctor blade during tape casting.

References

1. Tarascon, J.M. and M. Armand, *Issues and challenges facing rechargeable lithium batteries.* Nature, 2001. **414**(6861): p. 359-367.
2. Karden, E., et al., *Energy storage devices for future hybrid electric vehicles.* Journal of Power Sources, 2007. **168**(1): p. 2-11.
3. Brown, S., D. Pyke, and P. Steenhof, *Electric vehicles: The role and importance of standards in an emerging market.* Energy Policy, 2010. **38**(7): p. 3797-3806.
4. Solangi, K.H., et al., *A review on global solar energy policy.* Renewable & Sustainable Energy Reviews, 2011. **15**(4): p. 2149-2163.
5. Yoda, S. and K. Ishihara, *Global energy prospects in the 21st century: a battery-based society.* Journal of Power Sources, 1997. **68**(1): p. 3-7.
6. Kottegoda, I.R.M., et al., *High-rate-capable lithium-ion battery based on surface-modified natural graphite anode and substituted spinel cathode for hybrid electric vehicles.* Journal of the Electrochemical Society, 2005. **152**(8): p. A1595-A1599.
7. Smart, M.C., et al., *Lithium-Ion Electrolytes Containing Ester Cosolvents for Improved Low Temperature Performance.* Journal of the Electrochemical Society, 2010. **157**(12): p. A1361-A1374.
8. Armand, M. and J.M. Tarascon, *Building better batteries.* Nature, 2008. **451**(7179): p. 652-657.
9. Tobishima, S., *Secondary batteries - Lithium rechargeable systems - Lithium-Ion | Thermal Runaway*, in *Encyclopedia of Electrochemical Power Sources,* 2009, Elsevier: Amsterdam. p. 409-417.
10. McCurry, J. *Sony recalls nearly 500,000 PCs worldwide*. 2008 [cited 2012, 8th February]; Available from: http://www.guardian.co.uk/business/2008/sep/05/japan.sony.
11. Peled, E., *The Electrochemical-Behavior of Alkali and Alkaline-Earth Metals in Non-Aqueous Battery Systems - the Solid Electrolyte Interphase Model.* Journal of the Electrochemical Society, 1979. **126**(12): p. 2047-2051.
12. Verma, P., P. Maire, and P. Novak, *A review of the features and analyses of the solid electrolyte interphase in Li-ion batteries.* Electrochimica Acta, 2010. **55**(22): p. 6332-6341.
13. Linden, D. and T.B. Reddy, *Handbook of Batteries (3rd Edition)*, 2002, McGraw-Hill: New York. p. 1.3-1.4, 35.4-35.6, 35.18, 35.21-35.22, 35.28.
14. Kikkawa, J., et al., *Real-Space Observation of Li Extraction/Insertion in $Li_{1.2}Mn_{0.4}Fe_{0.4}O_2$ Positive Electrode Material for Li-Ion Batteries.* Electrochemical and Solid-State Letters, 2008. **11**(11): p. A183-A186.

15. Xu, K., *Secondary batteries - Lithium rechargeable systems | Electrolytes: Overview*, in *Encyclopedia of Electrochemical Power Sources,* 2009, Elsevier: Amsterdam. p. 51-70.
16. Inaba, M., *Secondary batteries - Lithium rechargeable systems - Lithium-Ion | Negative electrodes: Graphite*, in *Encyclopedia of Electrochemical Power Sources,* 2009, Elsevier: Amsterdam. p. 198-208.
17. Winter, M., P. Novak, and A. Monnier, *Graphites for lithium-ion cells: The correlation of the first-cycle charge loss with the Brunauer-Emmett-Teller surface area.* Journal of the Electrochemical Society, 1998. **145**(2): p. 428-436.
18. Koksbang, R., et al., *Cathode materials for lithium rocking chair batteries.* Solid State Ionics, 1996. **84**(1-2): p. 1-21.
19. Fergus, J.W., *Recent developments in cathode materials for lithium ion batteries.* Journal of Power Sources, 2010. **195**(4): p. 939-954.
20. Xu, K., et al., *Solvation sheath of Li^+ in nonaqueous electrolytes and its implication of graphite/electrolyte interface chemistry.* Journal of Physical Chemistry C, 2007. **111**(20): p. 7411-7421.
21. Smart, M.C., B.V. Ratnakumar, and S. Surampudi, *Electrolytes for low-temperature lithium batteries based on ternary mixtures of aliphatic carbonates.* Journal of the Electrochemical Society, 1999. **146**(2): p. 486-492.
22. Zhang, S.S., *A review on electrolyte additives for lithium-ion batteries.* Journal of Power Sources, 2006. **162**(2): p. 1379-1394.
23. Nishi, Y., *The development of lithium ion secondary batteries.* Chemical Record, 2001. **1**(5): p. 406-413.
24. Suryanarayanan, V. and M. Noel, *Role of carbon host lattices in Li-ion intercalation/de-intercalation processes.* Journal of Power Sources, 2002. **111**(2): p. 193-209.
25. Yoshio, M., et al., *Improvement of natural graphite as a lithium-ion battery anode material, from raw flake to carbon-coated sphere.* Journal of Materials Chemistry, 2004. **14**(11): p. 1754-1758.
26. Bruce, P.G., B. Scrosati, and J.M. Tarascon, *Nanomaterials for rechargeable lithium batteries.* Angewandte Chemie-International Edition, 2008. **47**(16): p. 2930-2946.
27. Arico, A.S., et al., *Nanostructured materials for advanced energy conversion and storage devices.* Nature Materials, 2005. **4**(5): p. 366-377.
28. Novak, P., et al., *The importance of the active surface area of graphite materials in the first lithium intercalation.* Journal of Power Sources, 2007. **174**(2): p. 1082-1085.

29. Bryngelsson, H., et al., *How dynamic is the SEI?* Journal of Power Sources, 2007. **174**(2): p. 970-975.
30. Balbuena, P.B. and Y. Wang, *Lithium-Ion Batteries: Solid-Electrolyte Interphase*, 2004, Imperial College Press: London. p. 7, back cover.
31. Aurbach, D., et al., *The Study of Electrolyte-Solutions Based on Ethylene and Diethyl Carbonates for Rechargeable Li Batteries II. Graphite-Electrodes.* Journal of the Electrochemical Society, 1995. **142**(9): p. 2882-2890.
32. Kang, S.H., et al., *Investigating the solid electrolyte interphase using binder-free graphite electrodes.* Journal of Power Sources, 2008. **175**(1): p. 526-532.
33. Andersson, A.M. and K. Edstrom, *Chemical composition and morphology of the elevated temperature SEI on graphite.* Journal of the Electrochemical Society, 2001. **148**(10): p. A1100-A1109.
34. Aurbach, D., et al., *On the use of vinylene carbonate (VC) as an additive to electrolyte solutions for Li-ion batteries.* Electrochimica Acta, 2002. **47**(9): p. 1423-1439.
35. Zheng, T., A.S. Gozdz, and G.G. Amatucci, *Reactivity of the solid electrolyte interface on carbon electrodes at elevated temperatures.* Journal of the Electrochemical Society, 1999. **146**(11): p. 4014-4018.
36. Placke, T., et al., *Influence of graphite surface modifications on the ratio of basal plane to "non-basal plane" surface area and on the anode performance in lithium ion batteries.* Journal of Power Sources, 2012. **200**: p. 83-91.
37. Peled, E., et al., *Composition, depth profiles and lateral distribution of materials in the SEI built on HOPG-TOF SIMS and XPS studies.* Journal of Power Sources, 2001. **97-8**: p. 52-57.
38. Yan, J., et al., *A novel perspective on the formation of the solid electrolyte interphase on the graphite electrode for lithium-ion batteries.* Electrochimica Acta, 2010. **55**(5): p. 1785-1794.
39. Gullbrekken, Ø., *Thermal characterisation of graphite materials for Li-ion batteries*, 2011: Department of Materials Science and Engineering, NTNU.
40. Smith, A.J., et al., *A High Precision Coulometry Study of the SEI Growth in Li/Graphite Cells.* Journal of the Electrochemical Society, 2011. **158**(5): p. A447-A452.
41. Xu, K., *Nonaqueous liquid electrolytes for lithium-based rechargeable batteries.* Chemical Reviews, 2004. **104**(10): p. 4303-4417.
42. Pesaran, A.A., *Battery Thermal Management in EV and HEVs: Issues and Solutions*, in *Advanced Automotive Battery Conference* 2001: Las Vegas, Nevada.

43. Yan, J.Y., et al., *Fuzzy Control for Battery Equalization Based on State of Charge.* 2010 IEEE 72nd Vehicular Technology Conference Fall, 2010.
44. Yamaki, J., et al., *Thermal stability of graphite anode with electrolyte in lithium-ion cells.* Solid State Ionics, 2002. **148**(3-4): p. 241-245.
45. Haik, O., et al., *On the Thermal Behavior of Lithium Intercalated Graphites.* Journal of the Electrochemical Society, 2011. **158**(8): p. A913-A923.
46. Roth, E.P., D.H. Doughty, and J. Franklin, *DSC investigation of exothermic reactions occurring at elevated temperatures in lithium-ion anodes containing PVDF-based binders.* Journal of Power Sources, 2004. **134**(2): p. 222-234.
47. Herstedt, M., et al., *Electrolyte additives for enhanced thermal stability of the graphite anode interface in a Li-ion battery.* Electrochimica Acta, 2004. **49**(14): p. 2351-2359.
48. Lee, S.M., et al., *Effect of carbon coating on thermal stability of natural graphite spheres used as anode materials in lithium-ion batteries.* Journal of Power Sources, 2009. **190**(2): p. 553-557.
49. Yang, H., et al., *Investigations of the exothermic reactions of natural graphite anode for Li-ion batteries during thermal runaway.* Journal of the Electrochemical Society, 2005. **152**(1): p. A73-A79.
50. Yaakov, D., et al., *On the Study of Electrolyte Solutions for Li-Ion Batteries That Can Work Over a Wide Temperature Range.* Journal of the Electrochemical Society, 2010. **157**(12): p. A1383-A1391.
51. Svensson, A.M., et al., *Investigation of Graphite Anodes for Li-ion Batteries Operating at Low Temperatures*, in *220th ECS Meeting* 2011: Boston.
52. Zhang, S.S., et al., *Effect of propylene carbonate on the low temperature performance of Li-ion cells.* Journal of Power Sources, 2002. **110**(1): p. 216-221.
53. Smart, M.C., et al. *Proceedings of 37th Power Sources Conference*. 1996. Cherry Hill, NJ.
54. *Sigma-Aldrich website*. [cited 2012, April]; Available from: http://www.sigmaaldrich.com/.
55. Ding, M.S., *Liquid-solid phase diagrams of ternary and quaternary organic carbonates.* Journal of the Electrochemical Society, 2004. **151**(5): p. A731-A738.
56. Ding, M.S., K. Xu, and T.R. Jow, *Liquid-solid phase diagrams of binary carbonates for lithium batteries.* Journal of the Electrochemical Society, 2000. **147**(5): p. 1688-1694.

57. Ding, M.S., et al., *Liquid/solid phase diagrams of binary carbonates for lithium batteries part II.* Journal of the Electrochemical Society, 2001. **148**(4): p. A299-A304.
58. Botte, G.G., R.E. White, and Z.M. Zhang, *Thermal stability of $LiPF_6$-EC:EMC electrolyte for lithium ion batteries.* Journal of Power Sources, 2001. **97-8**: p. 570-575.
59. Höhne, G.W.H., W.F. Hemminger, and H.-J. Flammersheim, *Differential Scanning Calorimetry*, 2003, Springer-Verlag: Berlin Heidelberg New York. p. 1-2, 10-12, 17-19, 26, 116-117.
60. *A Partial Cross Section of 2016 Coin*, Hohsen Corporation.
61. Mistler, R.E. and E.R. Twiname, *Tape Casting: Theory and Practice*, 2000, The American Ceramic Society: Westerville, Ohio. p. 67, 83, 93-94.
62. *Carbon powders for Lithium battery systems*. [cited 2012, May]; Available from: http://timcal.com/scopi/Group/Timcal/timcal.nsf/pagesref/SCMM-7EVDST?Opendocument&lang=en.
63. *CPreme Graphite*. [cited 2012, May]; Available from: http://www.cpreme.com/EN/Pages/index.aspx.
64. *Kynar® and Kynar Flex® PVDF*. [cited 2012, 12th May]; Available from: http://www.arkema-inc.com/kynar/page.cfm?pag=983.
65. *BF-Plainstainproof*. [cited 2012, 12th May]; Available from: http://www.circuitfoil.com/templates/rhuk_milkyway/products_details.php?id=22&KeepThis=true&TB_iframe=true.
66. *Obtained from Ethyl methyl carbonate bottle from Merck as product is discontinued and unavailable from website.*
67. Olivier, J.P. and S. Ross, *On Physical Adsorption. XVI. The Physical Interaction of H_2, D_2, CH_4, and CD_4 with Graphite.* Proceedings of the Royal Society of London. Series A, Mathematical and Physical Sciences, 1962. **265**(1323): p. 447-454.
68. Olivier, J.P. and M. Winter, *Determination of the absolute and relative extents of basal plane surface area and "non-basal plane surface" area of graphites and their impact on anode performance in lithium ion batteries.* Journal of Power Sources, 2001. **97-8**: p. 151-155.
69. Olivier, J.P., *Chapter Seven - The Surface Heterogeneity of Carbon and Its Assessment*, in *Adsorption by Carbons*, J.B. Eduardo and M.D.T. Juan, Editors. 2008, Elsevier: Amsterdam. p. 147-166.
70. Zhou, H., M.-A. Einarsrud, and F. Vullum-Bruer, *High capacity nanostructured $Li_2Fe_xSiO_4$/C with Fe hyperstoichiometry for Li-ion batteries.* Journal of Power Sources, submitted, 2012.
71. Svensson, A.M., *Personal Communication*, Ø. Gullbrekken, 2012.

72. Winter, M., et al., *Dilatometric investigations of graphite electrodes in nonaqueous lithium battery electrolytes.* Journal of the Electrochemical Society, 2000. **147**(7): p. 2427-2431.

Appendix A

A.1 Calculation of specific capacity of graphite

Moles of carbon atoms per gram graphite:

$$n_C = \frac{m_C}{M_C} = \frac{1\ \text{g}}{12.01 \frac{\text{g}}{\text{mol}}} = 0.0833\ \text{mol/g}$$

Moles of Li^+ per gram graphite:

$$n_{Li^+} = \frac{n_C}{6} = 0.0139\ \text{mol/g}$$

Specific capacity of graphite:

$$\text{Capacity} = n_{Li^+} \times N_{Av} \times e \times \frac{1}{3.6 \frac{\text{C}}{\text{mAh}}} = 372\ \text{mAh/g} \qquad \text{(A.1)}$$

N_{Av} is the Avogadro constant, $6.022 \times 10^{23}\ \text{mol}^{-1}$, e is the elementary charge and also the absolute value of the charge of an electron, 1.602×10^{-19} C. The last term is simply a conversion factor to obtain the value in mAh. This calculation assumes that each Li^+ intercalated in the graphite structure corresponds to one electron transferred via the external circuit.

Appendix B

This section contains supportive material for chapter 2.5.3.

B.1 DSC studies on the thermal stability of graphite electrodes

Many studies, some of them quantitative, have been conducted on the exothermic reactions in graphite electrodes. A selection of papers will be presented in the following. Yang et al. [49] examined a natural graphite electrode; Mag-10, in 2004. In the fully lithiated state and after cycling in a full cell against $Li_{0.36}Ni_{0.8}Co_{0.15}Al_{0.05}O_2$, the graphite anode without electrolyte generated 707 J/g of heat in a DSC analysis between 50 and 400°C. Furthermore, this study also found that the heat generation increased substantially for higher degrees of Li^+ intercalation in the graphite anode, especially from de-lithiated state to about 50% lithiated. Park et al. [48] performed DSC analyses on both unmodified and carbon-coated natural graphite electrodes with 1:1 EC:DEC and 1M $LiPF_6$ electrolyte. From 100 to 400°C, the overall heat generation was between ~4100 and ~4300 J/g. The substantially different heat generation found in these two studies can probably be explained by the extra electrolyte being removed from the DSC samples in the first study, and not in the second. In an already mentioned study by Roth et al. [46], DSC analyses were conducted on four graphite materials with electrolyte of 1:1 EC:DEC, 2 wt% VC and 1M $LiPF_6$. The reaction enthalpies of fully lithiated graphite anodes in DSC measurements up to 375°C varied between ~1800 and ~3000 J/g. Also here, the reaction enthalpies increased with the specific surface area of the graphite materials. Similarly to Aurbach et al. [34], the authors found that the addition of VC to the electrolyte resulted in a more stable SEI layer that decomposed more slowly at elevated temperatures. For example, most of the analyses did not exhibit the peak at 120°C caused by SEI decomposition [46]. Herstedt et al. [47] confirmed this observation after examining the effect of four additives, including VC, on the thermal stability of graphite electrodes. Of all the anodes examined, the onset temperature was highest for the anode cycled with VC-containing electrolyte, at 110°C. The additive reduced the overall heat generation from the graphite electrode which indicates that it did indeed improve the thermal stability.

High temperature DSC studies on pure electrolytes have also been carried out. In general, DSC curves from such studies exhibit only one peak caused by electrolyte decomposition, at a temperature above 250°C [58].

Appendix C

This section contains recipes and detailed procedures for the tape casting of graphite electrode sheets and the preparation of electrolytes used in this work.

C.1 Tape casting procedure of graphite electrode sheets

Table 15: Recipe for the Timcal SLP30 graphite casts

Material/chemical	Weight (g)
Graphite	37.05
Carbon black	0.95
PVDF	2
NMP	60

Procedure for preparing Timcal electrode sheet:

1. Graphite and carbon black were dried at 120°C overnight.
2. The dry components (graphite powder, carbon black and PVDF) were weighed.
3. PVDF was dissolved in NMP and stirred for 1.5 hours while covered.
4. Graphite, carbon black and the NMP-mixture were consecutively added to a ball mill container.
5. Five alumina balls of 30 mm diameter were added to the container, which was then sealed. The slurry was dispersed by rotary ball milling at 150 rpm for 1.5 hours.
6. The slurry was transferred to an Erlenmeyer flask and kept under vacuum while stirred to remove air bubbles.
7. The dispersed slurry was transferred onto a 10 µm thick copper foil cleaned with ethanol. Then, it was evenly distributed onto the foil by letting a doctor blade move over the slurry while keeping the foil still, the tape casting process.
8. The tape cast was dried at 60°C for two hours.
9. The graphite electrode cast was then dried in a Binder VD 23 vacuum oven overnight at a temperature of 120°C and a pressure of 10^{-5} bar.

The average graphite loading on the electrodes by using this tape casting process was 5.8 ± 0.2 mg graphite per cm^2. On average, the SLP30 electrodes were 92.3 ± 1.9 µm thick.

Table 16: Recipe for the CPreme casts

Material/chemical	Weight (g)
Graphite	4.31
Carbon black	0.14
PVDF	0.335
NMP	7.7

Procedure for preparing CPreme electrode sheet:

1. PVDF was dried overnight at 80°C.
2. The dry components (graphite powder, carbon black and PVDF) were weighed.
3. PVDF and NMP were consecutively added to a stainless steel crucible.
4. The PVDF and NMP mixture was shaken in a Retsch MM 2000 mixer mill for three minutes.
5. Graphite and carbon black were added to the mixture, which was then shaken for another three minutes. The resulting slurry was visually inspected to determine whether prolonged mixing and addition of more NMP was required to obtain a slurry with the desired viscosity and homogeneity.
6. The dispersed slurry was transferred onto a 10 μm thick copper foil cleaned with ethanol. Then, it was evenly distributed onto the foil by letting a doctor blade move over the slurry while keeping the foil still, the tape casting process.
7. The tape cast was dried at 60°C for two hours.
8. The graphite electrode cast was then dried in a Binder VD 23 vacuum oven overnight at a temperature of 120°C and a pressure of 10^{-5} bar.

The respective average graphite loadings on the CPreme P5 and G8 electrodes by using this tape casting process were 4.4 ± 0.3 and 6.6 ± 0.5 mg graphite per cm^2. On average, the P5 and G8 electrodes were 58.5 ± 2.1 and 78.9 ± 6.0 μm thick, respectively.

C.2 Electrolyte preparation procedure

General procedure:

1. The lithium salt was dried at 80°C before use in order to remove any trace moisture.
2. EC was heated to 50°C in order to melt the solvent.
3. The relevant organic solvents and $LiPF_6$ were successively added to a beaker.
4. In order to dissolve the lithium salt while simultaneously preventing EC from solidifying, the mixture was stirred and heated to a temperature of 50°C for 30 min while covered. The mixtures of EC and the other relevant organic solvents have lower freezing points than pure EC, resulting in a stable electrolyte solution at room temperature.
5. The ready electrolyte solution was transferred to a bottle with cork.

The electrolyte preparation was performed under argon atmosphere inside an MBraun glove box with water and oxygen contents below 1 ppm.